12-2020

Foundations of the Geometric Mechanics Udwadia-Kalaba Framework for Rigid Body Constrained Motion Analysis

Brennan McCann

Foundations of the Geometric Mechanics Udwadia-Kalaba Framework for Rigid Body Constrained Motion Analysis

By

Brennan McCann

A Thesis Submitted to the Faculty of Embry-Riddle Aeronautical University

In Partial Fulfillment of the Requirements for the Degree of

Master of Science in Aerospace Engineering

December 2020

Embry-Riddle Aeronautical University

Daytona Beach, Florida

Foundations of the Geometric Mechanics Udwadia-Kalaba Framework for Rigid Body Constrained Motion Analysis

By

Brennan McCann

This Thesis was prepared under the direction of the candidate's Thesis Committee Chair, Dr. Morad Nazari, Department of Aerospace Engineering, and has been approved by the members of the Thesis Committee. It was submitted to the Office of the Senior Vice President for Academic Affairs and Provost, and was accepted in the partial fulfillment of the requirements for the Degree of Master of Science in Aerospace Engineering.

THESIS COMMITTEE

Morad Nazari — Digitally signed by Morad Nazari Date: 2020.12.03 14:00:31 -05'00'

Chairman, Dr. Morad Nazari

Dr. Sergey V. Drakunov — Digitally signed by Dr. Sergey V. Drakunov Date: 2020.12.03 14:13:09 -05'00'

Member, Dr. Sergey Drakunov

Troy A. Henderson — Digitally signed by Troy A. Henderson Date: 2020.12.03 14:42:34 -05'00'

Member, Dr. Troy Henderson

Richard J. Prazenica — Digitally signed by Richard J. Prazenica Date: 2020.12.03 15:32:18 -05'00'

Member, Dr. Richard Prazenica

Marwan Al-Haik — Digitally signed by Marwan Al-Haik DN: cn=Marwan Al-Haik, o=Embry-Riddle Aeronautical University, ou=Aerospace Engineering, email=alhaikm@erau.edu, c=US Date: 2020.12.03 15:49:15 -05'00'

Graduate Program Coordinator, Dr. Marwan Al-Haik

12/3/2020

Date

Maj Mirmirani — Digitally signed by Maj Mirmirani Date: 2020.12.03 19:47:01 -05'00'

Dean of the College of Engineering, Dr. Maj Mirmirani

12/3/2020

Date

Christopher Grant — Digitally signed by Christopher Grant Date: 2020.12.04 08:36:49 -05'00'

Associate Provost of Academic Support, Dr. Christopher Grant

12/4/2020

Date

ACKNOWLEDGEMENTS

I would like to first thank my parents, sister, and the rest of my family, whose constant support and encouragement have made this possible. This work is as much your achievement as it is mine. I owe you an immeasurable debt and am consistently grateful of your dedication to ensuring I succeed.

In addition, I thank my advisor, Dr. Morad Nazari for his time and attention to my studies and work. Thank you for helping me to take my abstract research interests and hone them into a focused work. Your guidance and advice has been fundamental in being able to complete the work detailed here.

I also would like to thank my committee consisting of Dr. Troy Henderson, Dr. Richard Prazenica, and Dr. Sergey Drakunov. Your assistance, comments, and suggestions have improved the quality of this work and have been sincerely appreciated.

Support from the Department of Education Graduate Assistance in Areas of National Need (GAANN) and the Faculty Innovative Research in Science and Technology (FIRST) are gratefully acknowledged.

ABSTRACT

Presented herein are multiple tools for constrained motion analysis extended to different dynamical frameworks. The Udwadia-Kalaba (UK) formalism for the constrained motion analysis of a point mass is a well-documented and applied methodology. Here, UK formulation is generalized to the dynamics of rigid bodies on nonlinear manifolds in the geometric mechanics framework. This approach simultaneously treats rotational and translational motion in a unified method without encountering singularites or non-uniqueness, issues that would arise were attitude parameterization sets used. The viability of this geometric mechanics UK formalism is demonstrated for the cases of fully and underconstrained systems. The nominal UK formalism requires the complete knowledge of the system dynamics. In the presence of unmodeled dynamics or uncertainties in the system, the stability of the system cannot be assessed using the nominal UK formulation. Therefore, a controller is presented that stabilizes the system under unmodeled dynamics and external perturbations. In addition, the UK formulation has been historically applied to systems with equality constraints. However, it has not been formulated for usage with inequality constraints. Here, the implementation of slack and excess variables to treat this class of constraints is presented for usage within the UK formulation for the point mass constrained motion with inequality constraints. Also contained within is an extension of pre-existing work which models the gravitational force acting on a rigid body from a nonuniform gravitational field that holds for any degree and order of spherical harmonics.

TABLE OF CONTENTS

LIST OF FIGURES

Figure Page

Figure Page

Figure Page

LIST OF TABLES

ABBREVIATIONS

BI	Bounding Inequalities
FCCN	Fully Constrained, Circular, Noninclined
FCEI	Fully Constrained, Elliptical, Inclined
FCEIM	Fully Constrained, Elliptical, Inclined Case on Manifolds
GMUK	Geometric Mechanics Udwadia-Kalaba Formulation
GT	Greater Than
LCI	Lunar Centered Inertial
LCF	Lunar Centered Fixed
LT	Less Than
M-L	Morse-Lyapunov (as in a Morse-Lyapunov based controller)
SMD	Spring-Mass-Damper
UCEI	Under Constrained, Elliptical, Inclined
UCEIS	Under Constrained, Elliptical, Inclined Orbit with Sine Torque
UK	Udwadia-Kalaba Formulation

NOMENCLATURE

f	=	true anomaly
$\mathbf{f}$	=	external forces expressed in body frame $\mathcal{B}$
g	=	member of SE(3) that describes rigid body configuration
g_d	=	desired rigid body configuration
$\mathbf{L}$	=	external torques in body frame $\mathcal{B}$
R	=	rotation matrix from body frame $\mathcal{B}$ to inertial frame $\mathcal{N}$ ($R \in \mathrm{SO}(3)$)
$\mathbf{r}$	=	position vector of rigid body center of mass in the inertial frame $\mathcal{N}$
$\mathbf{v}$	=	velocity in the inertial frame expressed in the body frame
$\mathbf{V}$	=	augmented velocity vector
$\mathbf{u}$	=	augmented vector of control input torques and forces
$\mathbf{u}_f$	=	control input force in body frame $\mathcal{B}$
$\mathbf{u}_L$	=	control input torque in body frame $\mathcal{B}$
τ	=	augmented vector of external torques and forces
μ	=	gravitational parameter
Ω	=	right ascension of the ascending node
ω	=	argument of periapsis
$\boldsymbol{\omega}$	=	angular velocity expressed in the body frame $\mathcal{B}$

1. Introduction

Constrained motion analysis is a useful method to find control accelerations necessary to satisfy constraints on dynamical systems. A convenient approach for dealing with the dynamics of constrained point masses under equality constraints is Udwadia-Kalaba (UK) formulation. Some extensions have been undertaken to apply this formulation to rigid bodies. However, the usage of geometric mechanics as the configuration of rigid bodies evolves on the Special Euclidean group, SE(3), has not been strictly applied to constrained motion analysis or UK formalism. In addition, UK formulation has been well defined and has a strong heritage of applications for handling equality constraints; however, inequality constraints have yet to be satisfactorily modeled in that framework. Furthermore, treatment of initial conditions and disturbances that violate constraints within UK formulation can be analyzed using a form of feedback control.

1.1. Literature Review

A constrained motion analysis technique was proposed by Udwadia and Kalaba (1992) to calculate the generalized accelerations needed to satisfy a set of equality constraints acting on a system of particles using the Moorse-Penrose generalized inverse. Their method is capable of treating all types of equality constraints as long as they are differentiable, but it also requires the exact dynamics of the unconstrained system to be known.

UK formulation is defined for cases where the initial conditions satisfy the constraints. However, in the case of unsatisfied constraints derived from initial conditions, different types of stability analysis can be used to drive the system to constraint satisfaction. Among other methods, Baumgarte's stability analysis (Baumgarte, 1972) has frequently been used in the literature (Cho & Udwadia, 2010; Xu & Liu, 2017). While many constrained motion analysis problems have classically employed Lagrange multipliers for treatment of constraints, UK formulation does not require any computation of the Lagrange multipliers, though they can still be analytically and explicitly obtained as noted by Udwadia and Kalaba (2008). This simplifies calculation of the required constraint accelerations significantly.

The UK equations of constrained motion have been utilized in many applications both on Earth and in space. A modal UK formulation extension for use in modelling the dynamics of flexible systems under intermittent impacts was presented by Antunes et al. (2017). Treatment of multi-link robots (Yang et al., 2019), robotic tracking control (Sun et al., 2015), and other applications in robotics have often employed UK formulation. In Lam (2006), UK formulation was applied to a point-mass spacecraft orbiting an oblate body in order to maintain a circular orbit and a constant inclination. That framework was used in Cho and Udwadia (2010) and Memon et al. (2019) to find the explicit solution to satellite formation keeping. In Memon et al. (2019), the UK framework was applied along with Coulomb forces to control two charged spacecraft to maintain formation in an elliptic orbit. The results with and without the Coulomb effects were compared to those obtained by the use of near-optimal control schemes designed to achieve the same formation. The application of UK formulation to maintain a spacecraft stationed at an unstable Lagrange point under perturbations from solar radiation pressure (SRP) in the Sun-Earth-spacecraft circular restricted three body problem system was shown by Patel et al. (2019). UK formulation has also been applied to constrain a spacecraft to hover over an asteroid (Stackhouse et al., 2019, 2020). Space related applications have also considered elements of the planar pose within the Udwadia-Kalaba formulation for rendezvous (Pothen & Ulrich, 2019).

This approach is effective for equality constraints imposed on the system. However, inequality constraints present a different challenge. To the author's knowledge, no treatment of inequality constraints has been presented in Udwadia-Kalaba formulation except for in Yin et al. (2019), which suggested employing a diffeomorphism to transform the space bounded by a set of inequalities into an unbounded space; however, this method is undefined for singular inequalities. In short, it requires that pre-existing equality constraints be further bounded by other inequality constraints. As such, these equality constraints are mapped into a bounded space and assessed in that space. Such an approach will not work for constraints that are purely inequality constraints. Within static optimization, inequality constraints are

converted to equality constraints via addition or subtraction of slack and excess variables respectively, per Griva and Nash (2017). Furthermore, direct optimization methods can provide another means by which the validity and optimality of the solution derived from these methodologies may be analyzed. Many nonlinear-programming solvers are effective for parameter optimization problems; hence, they are used to solve these optimization problems (Liu et al., 2017; Kelly, 2016; Luenberger, 1969). However, this requires transforming the continuous time optimization problem into a discretized parameter optimization problem (Kelly, 2017; Hedengren et al., 2014; Fahroo & Ross, 2000).

Spacecraft and other dynamical systems often experience a coupling between their translational and rotational motions. For the case of spacecraft, orbital and attitude motions are often coupled due to the motion of flexible structures with many degrees of freedom, gravity gradient forces and torques, attitude-dependent forces and torques such as aerodynamic drag and solar-radiation pressure (SRP), and spacecraft rendezvous and proximity operations to name but a few.

In order to account for translational and rotational couplings, dual quaternions have been used for constrained motion analyses and optimization problems of multibody dynamical systems (Valverde & Tsiotras, 2018). Work has also been completed using dual-quaternions within UK formulation for spacecraft docking (Dong et al., 2018). In addition, robotic applications not strictly related to aerospace have applied Udwadia-Kalaba formulation to the pose of the system (Nielsen et al., 2020). A treatment of quaternions within UK formulation was developed for control torque determination by Udwadia and Schutte (2011). However, quaternions (and consequently dual quaternions) suffer from the unwinding issue that contributes to an inability to differentiate quaternion representations.

A key advantage of analyzing a rigid body system in the geometric mechanics framework is that it allows for this coupling to be accounted for while avoiding non-uniqueness and singularities due to the use of attitude parameterization sets. Furthermore, given the structure of elements in this framework, a single control law can be

designed to suit the needs of the coupled system. There have been some treatments of systems with constrained angular and translational components including vehicle trajectory tracking (Yin et al., 2019; Sun et al., 2016). Analysis of constraint satisfaction was conducted using Munthe-Kaas integration of members of SE(3). The analysis conducted determined that the integrator perfectly satisfied the constraints (Müller & Terze, 2014a, 2014b).

1.2. Research Goals

The research contained here aims to address some of the areas of development outlined above. First, derivation of a dynamic model that accounts for higher-order gravitational terms in the roto-translational coupling is presented. Then, the Udwadia-Kalaba formulation is generalized for use in the geometric mechanics framework for fully and underconstrained systems on $\mathbb{R}^6$ and for fully constrained systems on $T^2SE(3)$. In addition, the practicality of the methodology is extended by presenting a method for accounting for unmodeled dynamics and off-nominal initial conditions. Finally, a novel approach for treating inequality constraints within UK formulation is presented.

2. Preliminaries

Extending the existing UK formulation requires a through examination of both the UK formulation for a system of particles and a discussion of the geometric mechanics framework. First, the classical UK formulation is presented. Then, salient details about differential geometry are highlighted and summarized. Finally, these tools are used to provide mathematical context for the geometric mechanics framework.

2.1. Udwadia-Kalaba Formulation

Consider a system of n particles subject to s constraints and assume that the constraints are differentiable. Let $\mathbf{q}$ be a vector of generalized coordinates of n particles. Also, let $\boldsymbol{\Theta}(\mathbf{q}, t) \in \mathbb{R}^{s_1}$ represent the set of all holonomic constraints and $\boldsymbol{\Psi}(\mathbf{q}, \dot{\mathbf{q}}, t) \in \mathbb{R}^{s_2}$ represent the set of non-holonomic constraints ($s_1 + s_2 = s$). If $\boldsymbol{\Theta}$ is differentiated twice and $\boldsymbol{\Psi}$ once, the constraint equation of the form presented by Udwadia and Kalaba (1992, 2008) is obtained.

$$A(\mathbf{q}, \dot{\mathbf{q}}, t)\ddot{\mathbf{q}} = \mathbf{b}(\mathbf{q}, \dot{\mathbf{q}}, t). \tag{1}$$

Hence, in three-dimensional Euclidean space, $\mathbf{q} \in \mathbb{R}^{3n\times 1}$, $A \in \mathbb{R}^{s\times 3n}$ and $\mathbf{b} \in \mathbb{R}^{s\times 1}$. If the matrix M is defined as a $3n \times 3n$ matrix with the values of the masses of the particles along the diagonal, the constraint acceleration can be determined.

$$\mathbf{a}_c = M^{-1}A^T(AM^{-1}A^T)^+(\mathbf{b} - A\mathbf{a}), \tag{2}$$

Here, $\mathbf{a} \in \mathbb{R}^{3n\times 1}$ is the acceleration of the unconstrained system and $(\cdot)^+$ denotes the pseudoinverse or the Moore-Penrose generalized inverse. UK formulation is especially useful becase it does not require explicit determination of the Lagrange multipliers to find a solution. However, the Lagrange multipliers can be determined within this framework and were given by Udwadia and Kalaba (2008).

$$\boldsymbol{\lambda} = \left(AM^{-1}A^T\right)^{-1}(\mathbf{b} - A\mathbf{a})\,. \tag{3}$$

This approach to constraint motion analysis requires that the constraint is satisfied by the initial condition. In the event that this is not the case, Baumgarte's stability analysis (Baumgarte, 1972) can be employed for the transient response of the system as implemented by Cho and Udwadia (2010). Then, the general set of all constraints can be given as $\mathbf{\Phi} \in \mathbb{R}^s$. When $\mathbf{\Phi} \neq \mathbf{0}$, i.e. when the desired motion is not satisfied at the initial time, the constraints can be rewritten as,

$$\ddot{\mathbf{\Phi}} + \alpha\dot{\mathbf{\Phi}} + \beta\mathbf{\Phi} = \mathbf{0}, \tag{4}$$

where $\alpha = \text{diag}(\alpha_1, \alpha_2 \ldots \alpha_s)$ and $\beta = \text{diag}(\beta_1, \beta_2 \ldots \beta_s)$. Depending on selection of α and β, the system will be under, critically, or over damped. In the case of critically or over damped values of α and β, the system will approach zero asymptotically, thereby satisfying the constraint given by Φ. The methodology described here applies to a system of point masses. This same approach is generalized to a system of rigid bodies in Chapter 4. This extension is then used to analyze the stability of a rigid body system under disturbances and unmodeled dynamics in Chapter 5.

2.2. Differential Geometry and Lie Groups

A manifold $\mathcal{M}$ is a space with a locally Euclidean, or flat, structure. However, this may not be the case globally. At a general point $x \in \mathcal{M}$, there exists a tangent space denoted $\text{T}_x\mathcal{M}$. The disjoint union of all tangent spaces over the manifold is the tangent bundle $\text{T}\mathcal{M}$ with elements $\dot{x} \in \text{T}\mathcal{M}$ (Michor, 2008). Note that, by definition, the tangent bundle $\text{T}\mathcal{M}$ is also a manifold. Hence, for every $\dot{x} \in \text{T}\mathcal{M}$, there is also another tangent space denoted $\text{T}_{\dot{x}}\mathcal{M}$. This intuition lends itself to exploration of the second-order tangent bundle denoted as $\text{T}^2\mathcal{M}$. This bundle contains elements $\ddot{x} \in \text{T}^2\mathcal{M}$ that are on the tangent bundle to $\text{T}\mathcal{M}$ (Suri, 2013, 2016; Dodson & Galanis, 2004).

There are several relationships between $\mathcal{M}$, $\text{T}\mathcal{M}$, and $\text{T}^2\mathcal{M}$ that are relevant to understanding the geometry of these manifolds. First, a push-forward is a mapping from the tangent space of one manifold to the tangent space of another. For example, for a mapping ϕ

from manifold $\mathcal{M}$ to $\mathcal{P}$ ($\phi : \mathcal{M} \to \mathcal{P}$), the push-forward $d\phi$ (also called the differential of ϕ) at x is defined as follows:

$$d\phi : \mathrm{T}_x\mathcal{M} \to \mathrm{T}_{\phi(x)}\mathcal{P}$$

Since $\mathcal{M}$ and $\mathrm{T}\mathcal{M}$ are both manifolds, the canonical projections $\pi_{\mathrm{T}\mathcal{M}}$ and $\pi_{\mathrm{T}^2\mathcal{M}}$ are defined as $\pi_{\mathrm{T}\mathcal{M}} : \mathrm{T}\mathcal{M} \to \mathcal{M}$ and $\pi_{\mathrm{T}^2\mathcal{M}} : \mathrm{T}^2\mathcal{M} \to \mathrm{T}\mathcal{M}$, respectively. Furthermore, using the concept of the push-forward of the canonical projection $\pi_{\mathrm{T}\mathcal{M}}$ to define $d\pi_{\mathrm{T}\mathcal{M}}$, a mapping from the tangent bundle of $\mathrm{T}\mathcal{M}$ (i.e. $\mathrm{T}^2\mathcal{M}$) onto the tangent bundle of $\mathcal{M}$ (i.e. $\mathrm{T}\mathcal{M}$) is obtained. In a sense, this push-forward is performing a mapping from the second-order tangent bundle to the tangent bundle. With this intuition, it can be concluded that the push forward of the canonical projection, $d\pi_{\mathrm{T}\mathcal{M}}$, and the canonical projection of the second-order tangent bundle $\pi_{\mathrm{T}^2\mathcal{M}}$ are isomorphic. These quantities are related by the isomorphism called the canonical flip, which, while relevant, is not strictly required for the formulation presented here. The reader is referred to Suri (2016) and Dodson and Galanis (2005) for further details about the canonical flip isomorphism.

Next, the concept of fibers and fiber bundles is briefly introduced. Consider some space E, a base space B, and a fiber F. The space E is called a fiber bundle if E is a bundle that locally behaves like the product space of $B \times F$, but may not behave so globally. Hence, E behaves locally as the product space. This implies that there locally exists a surjective mapping $\phi : E \to B$ that maps from the total space E to the base space B. Tangent bundles are an example of fiber bundles. That is, the tangent bundle $\mathrm{T}\mathcal{M}$ can be locally written as $\mathrm{T}\mathcal{M} = \mathcal{M} \times F_1$, where F_1 is the fiber associated with $\mathcal{M}$. If the tangent bundle locally behaves as $T\mathcal{M} = \mathcal{M} \times F$, then the tangent bundle is called a trivial fiber bundle since it equates $E = B \times F$ locally. In this study, for the case of the manifolds, their tangent- and second-order tangent bundles, the product space is the tangent bundle and the base space is the base manifold. Considering second-order tangent bundles in the context of fiber bundles,

the second-order tangent bundle can be defined locally as,

$$\mathrm{T}^2\mathcal{M} = (\mathcal{M} \times F_1) \times F_2 = \mathrm{T}\mathcal{M} \times F_2, \tag{5}$$

where F_2 is the fiber associated with $\mathrm{T}\mathcal{M}$. An important distinction to make is between a direct product and a semidirect product. Consider a group $\mathcal{G}$ with subgroups $\mathcal{H}$ and $\mathcal{K}$. The group $\mathcal{G}$ is isomorphic to the direct product between $\mathcal{H}$ and $\mathcal{K}$ (i.e. $\mathcal{G} = \mathcal{H} \times \mathcal{K}$) if:

1) $\mathcal{H} \triangleleft \mathcal{G}$ and $\mathcal{K} \triangleleft \mathcal{G}$,
2) $\mathcal{H} \cap \mathcal{K} = I$.

The $\cap$ operator indicates the intersection between two groups. In addition, the $\triangleleft$ operator denotes a normal subgroup, which has the property that, for $\mathcal{H}$ which is a subgroup of $\mathcal{G}$, the subgroup $\mathcal{H}$ is a normal subgroup of $\mathcal{G}$, (i.e. $\mathcal{H} \triangleleft \mathcal{G}$) if and only if for $g \in \mathcal{G}$ and $h \in \mathcal{H}$, $ghg^{-1} \in \mathcal{H}$. By contrast, a group $\mathcal{G}$ is isomorphic to the semidirect product between subgroups $\mathcal{H}$ and $\mathcal{K}$ (i.e. $\mathcal{G} = \mathcal{H} \ltimes \mathcal{K}$) if:

1) $\mathcal{H} \triangleleft \mathcal{G}$,
2) $\mathcal{H} \cap \mathcal{K} = I$.

Manifolds can also be specified by the properties of the norm and inner products on these spaces. First, a Banach manifold is a manifold endowed with a norm of its elements. A subset of Banach manifolds are Riemannian manifolds, which are a set of smooth manifolds with tangent spaces endowed with a smoothly varying inner product or Riemannian metric (Absil et al., 2008). The following section illustrates how these concepts relate to rigid body configuration and dynamics on the Special Euclidean group SE(3).

It is also necessary to present a few qualities of Lie groups and group theory that are also relevant to the dynamics on this manifold. A set of elements under an operation is considered a group $\mathcal{G}$ if and only if:

1) The group is closed under the group operation,
2) The group operation is associative,
3) There exists an identity element,

4) There exists an inverse element.

Lie groups $\mathcal{G}$ are subsets of $\mathbb{R}^N$ such that:

1) $\mathcal{G}$ is a group,

2) $\mathcal{G}$ is a manifold,

3) The group operation and its inverse are smooth.

Lie groups are endowed with a Lie algebra. This quantity forms a basis for the tangent space of the Lie group manifold. It also is coincident with the tangent space at the identity of the manifold (Casado & Martínez-Rubio, 2019). These properties of Lie groups and differential geometry form the foundation for geometric mechanics. This framework is described in the following section and is necessary for development of the geometric mechanics UK formulation in Chapter 4.

2.3. Rigid Body Motion in the Geometric Mechanics Framework

Rigid body configurations can be described as elements of the Special Euclidean group SE(3), which describes both rotational and translational motion of rigid bodies in three-dimensional space. This group is a Lie group, meaning that SE(3) is also a manifold. Let the configuration of a rigid body g be described by (Sastry, 1999),

$$g = \begin{bmatrix} R & \mathbf{r} \\ 0_{1\times 3} & 1 \end{bmatrix} \in \mathrm{SE}(3), \tag{6}$$

where $R \in \mathrm{SO}(3)$ is a rotation matrix from the rigid body's body frame $\mathcal{B}$ to the inertial frame $\mathcal{N}$ and $\mathbf{r} \in \mathbb{R}^3$ is a position vector that points from the origin of the $\mathcal{N}$ frame to the center of mass of the rigid body. If the Frobenius inner product is taken as the Riemannian metric, it follows that SE(3) is a Riemannian manifold. This also implies that a norm, specifically the Frobenius norm, exists on this space.

$$\langle A, B \rangle_F = \sum_{i=1}^{m} \sum_{j=1}^{n} A_{ij} B_{ij} = \mathrm{tr}\left(A^T B\right) \tag{7}$$

$$\|A\|_F = \sqrt{\langle A, A \rangle_F} \tag{8}$$

Therefore, SE(3) is a Banach manifold, which also follows from the fact that inner product spaces, such as Riemannian manifolds, are subsets of normed, or Banach spaces (Biggs & Holderbaum, 2005; Dodson & Galanis, 2004). The augmented velocity vector is given by,

$$\mathbf{V} = \begin{bmatrix} \boldsymbol{\omega} \\ \mathbf{v} \end{bmatrix} \in \mathbb{R}^6, \tag{9}$$

where $\omega \in \mathbb{R}^3$ is the angular velocity and $\mathbf{v} \in \mathbb{R}^3$ is the translational velocity of the rigid body, both with respect to the $\mathcal{N}$ frame expressed in the $\mathcal{B}$ frame. The states of the rigid body motion in three-dimensional space can therefore be fully described by $(g, V) \in \mathrm{SE}(3) \ltimes \mathbb{R}^6$. The tangent space to SE(3), denoted TSE(3), is the semidirect product between SE(3) and $\mathbb{R}^6$ (i.e. $\mathrm{TSE}(3) = \mathrm{SE}(3) \ltimes \mathbb{R}^6$) and the elements of that space are given by $\dot{g}$. Likewise, the double tangent bundle is denoted $\mathrm{T}^2\mathrm{SE}(3)$ and the elements of the double tangent bundle are denoted $\ddot{g}$. Furthermore, applying and simplifying the definition of the fiber bundle, it can be said that the double tangent bundle is the semidirect product between SE(3) and $\mathbb{R}^{12}$ (i.e. $\mathrm{T}^2\mathrm{SE}(3) = \mathrm{SE}(3) \ltimes \mathbb{R}^{12}$). Note that, this quantity obeys the normal subgroup condition. Furthermore, for both the tangent and double tangent bundle, the disjoint union, or the intersection, between the component subgroups is I_4. The rationale for these definitions becomes clearer as the dynamics on SE(3)and the structure of their components are investigated.

The kinematics and kinetics of the rigid body's motion are given by,

$$\dot{g} = g\mathbf{V}^{\vee}, \tag{10a}$$

$$\dot{\mathbf{V}} = \mathbb{I}^{-1}\mathrm{ad}^{*}_{\mathbf{V}}\mathbb{I}\mathbf{V} + \mathbb{I}^{-1}(\boldsymbol{\tau} + \mathbf{u}), \tag{10b}$$

respectively, where $\tau = [\mathbf{L}^T, \mathbf{f}^T]^T \in \mathbb{R}^6$ is the augmented vector of external torques $\mathbf{L} \in \mathbb{R}^3$ and forces $\mathbf{f} \in \mathbb{R}^3$, and $\mathbf{u} = [\mathbf{u}_L^T, \mathbf{u}_f^T]^T \in \mathbb{R}^6$ is the augmented vector of control input torques $\mathbf{u}_L \in \mathbb{R}^3$ and forces $\mathbf{u}_f \in \mathbb{R}^3$, all expressed in the $\mathcal{B}$ frame. In Equation (10b), $\mathbb{I}$ is the tensor

of mass and inertia properties.

$$\mathbb{I} = \begin{bmatrix} J & 0_{3\times3} \\ 0_{3\times3} & mI_3 \end{bmatrix}, \tag{11}$$

In this matrix, J and m are the moment of inertia matrix and mass of the rigid body, respectively, and I_3 is the 3×3 identity matrix. Also, the mapping $(\cdot)^\vee : \mathbb{R}^6 \to \mathfrak{se}(3)$ is applied to the augmented velocity vector $\mathbf{V}$.

$$V^\vee = \begin{bmatrix} \omega^\times & \mathbf{v} \\ 0_{1\times3} & 0 \end{bmatrix}, \tag{12}$$

Note that the $(\cdot)^\times : \mathbb{R}^3 \to \mathfrak{so}(3)$ operator is defined for a three-dimensional vector ω.

$$\omega^\times = \begin{bmatrix} 0 & -\omega_3 & \omega_2 \\ \omega_3 & 0 & -\omega_1 \\ -\omega_2 & \omega_1 & 0 \end{bmatrix} \tag{13}$$

Furthermore, the co-adjoint operator $\mathrm{ad}^*_{\mathbf{V}}$ in Equation (10b) is obtained by taking the transpose of the adjoint operator:

$$\mathrm{ad}_{\mathbf{V}} = \begin{bmatrix} \omega^\times & 0_{3\times3} \\ v^\times & \omega^\times \end{bmatrix} \tag{14}$$

That is,

$$\mathrm{ad}^*_{\mathbf{V}} = \begin{bmatrix} -\omega^\times & -v^\times \\ 0_{3\times3} & -\omega^\times \end{bmatrix} \tag{15}$$

A final operator that is particular importance to relative configuration and velocity determination is the linear adjoint operator given by,

$$\mathrm{Ad}_g = \begin{bmatrix} R & 0_{3\times3} \\ r^\times R & R \end{bmatrix} \tag{16}$$

The translational and rotational motions of the rigid body are obtained through simultaneous integration of Eqs. (10a) and (10b) over time. By differentiating the kinematics in Equation (10a) with respect to time and using the expression for kinetics in Equation (10b), the second rate of change of g with respect to time can be obtained as,

$$\ddot{g} = \ddot{g}_a + \ddot{g}_c \in \mathrm{T}^2\mathrm{SE}(3), \tag{17}$$

where

$$\ddot{g}_a = g\left(V^{\vee^2} + \left(\mathbb{I}^{-1}\left(\mathrm{ad}_V^*\mathbb{I}V + \tau\right)\right)^{\vee}\right), \tag{18}$$

and

$$\ddot{g}_c = g\left(\mathbb{I}^{-1}u\right)^{\vee} \tag{19}$$

Applying the exponential mapping $\xi = \exp(g)^{|}$, where $(\cdot)^{|}$ denotes the unwedge mapping and is the inverse of the wedge mapping given in Equation (12), the dynamic problem on the Lie group SE(3) as given by Equation (10) becomes a problem on the Lie algebra $\mathfrak{se}(3)$ associated with SE(3), i.e.,

$$\dot{\xi} = (I_6 + \frac{1}{2}\mathrm{ad}_\xi + F_1(\theta)\mathrm{ad}_\xi^2 + F_2(\theta)\mathrm{ad}_\xi^4)\mathbf{V}, \tag{20}$$

where $\xi = [\mathbf{\Theta}^T, \mathbf{p}^T]^T \in \mathbb{R}^6$ denotes the exponential coordinates, where $\mathbf{\Theta} \in \mathbb{R}^3$ is the product of eigenaxis (principal axis) and eigenangle (principal angle) of rotation, i.e. $\mathbf{\Theta} = \theta\mathbf{e}$ and $||\mathbf{\Theta}|| = \theta$, and $\mathbf{p} \in \mathbb{R}^3$ represent the translational vector components. Also, in Equation (20),

$$F_1(\theta) = \frac{2}{\theta^2} - \frac{3}{4\theta}\cot\frac{\theta}{2} - \frac{1}{8}\csc^2\frac{\theta}{2}, \tag{21}$$

and,

$$F_2(\theta) = \frac{1}{\theta^4} - \frac{1}{4\theta^3}\cot\frac{\theta}{2} - \frac{1}{8\theta^2}\csc^2\frac{\theta}{2}. \tag{22}$$

3. Rigid Body Dynamics and Higher-Order Gravitational Models

The dynamics of the rigid-body spacecraft in an orbit around a central body are given by Equation (10), with the properties of the spacecraft defined in the same fashion as the properties of the rigid body. In the two-body problem, the external effect τ is the augmented vector of the gravity gradient moment and force applied to spacecraft expressed in the spacecraft body frame, i.e. $\tau = [\mathbf{L}_G^T, \mathbf{f}_G^T]^T$, where from Schaub and Junkins (2018),

$$\mathbf{L}_G = \frac{3\mu}{||\mathbf{r}_\mathcal{B}||^5}\mathbf{r}_\mathcal{B}^\times J\mathbf{r}_\mathcal{B}, \tag{23a}$$

is the gravity gradient moment, and,

$$\mathbf{f}_G = -\frac{\mu m}{||\mathbf{r}_\mathcal{B}||^3}\left(1 + \frac{3}{m||\mathbf{r}_\mathcal{B}||^2}\left[J + \frac{1}{2}(\mathrm{tr}(J) - 5\hat{r}_\mathcal{B}^T J\hat{r}_\mathcal{B})I_3\right]\right)\mathbf{r}_\mathcal{B}, \tag{23b}$$

is the gravity gradient force, where $\mathbf{r}_\mathcal{B} = R^T\mathbf{r}$, the quantity $\hat{r}_\mathcal{B} = \mathbf{r}_\mathcal{B}/||\mathbf{r}_\mathcal{B}||$, and μ denotes the gravitational parameter of the central body. In Equation (23), the central body is assumed to have a uniform gravitational field. However, to ensure that the required accuracy is achieved, higher degree gravitational terms can be included in the model. Depending on the application, the chosen gravitational terms have a profound impact both on results and computation time.

The gravitational potential of a large body is given by Lemoine et al. (2013) and Vallado (2013) in the body's inertial frame by,

$$U = \frac{\mu}{(\mathbf{r}\cdot\mathbf{r})^{\frac{1}{2}}} + \frac{\mu}{(\mathbf{r}\cdot\mathbf{r})^{\frac{1}{2}}}\sum_{n=1}^{\infty}\sum_{p=0}^{n}\left(\frac{R_M}{(\mathbf{r}\cdot\mathbf{r})^{\frac{1}{2}}}\right)^n \bar{P}_{np}(\sin\theta)[\bar{C}_{np}\cos p\phi + \bar{S}_{np}\sin p\phi], \tag{24}$$

where θ is the spacecraft's latitude and ϕ is its longitude. The value of R_M denotes the mean radius of the body being orbited, $\bar{P}_{np}$ denotes the normalized associated Legendre functions, and $\bar{C}_{np}$ and $\bar{S}_{np}$ are the normalized gravity coefficients. To find the acceleration caused by the gravity in the central body's inertial frame, differentiate U with respect to $\mathbf{r}$.

$$\mathbf{a} = -\frac{\mu\mathbf{r}}{(\mathbf{r}\cdot\mathbf{r})^{\frac{3}{2}}}\left[1 - \sum_{n=1}^{\infty}\sum_{p=0}^{n}(n+1)\left(\frac{R_M}{(\mathbf{r}\cdot\mathbf{r})^{\frac{1}{2}}}\right)^n \bar{P}_{np}(\sin\theta)[\bar{C}_{np}\cos p\phi + \bar{S}_{np}\sin p\phi]\right] \tag{25}$$

It is important to note that the longitude and latitude are derived from the position vector in the LCF frame, but these expressions are written in the LCI frame. To find the longitude and latitude, it is necessary to find the position vector in the LCF frame. This will be discussed presently.

The Legendre polynomial P_n, associated Legendre functions P_{nm}, and the normalized associated Legendre functions are given by the the following expressions respectively (Abramowitz & Stegun, 2014):

$$P_n(t) = \frac{1}{2^n n!}\frac{d^n}{dt^n}\left(t^2-1\right)^n \tag{26a}$$

$$P_{np}(t) = \left(1-t^2\right)^{\frac{p}{2}}\frac{d^p}{dt^p}P_n(t) \tag{26b}$$

$$\bar{P}_{np}(t) = \sqrt{n+\frac{1}{2}\frac{(n-p)!}{(n+p)!}}P_{np}(t) \tag{26c}$$

It is necessary to define $\mathbf{r}_{dm} = \mathbf{r} + \delta\mathbf{r}$ where $\mathbf{r}$ is the vector from the central body with radius R_M to the rigid body center of mass and $\delta\mathbf{r}$ is the position vector from the center of mass to some differential mass element. Recalling the gravitational potential of a body and substituting for $\mathbf{r}_{dm}$, the gravitational force per differential mass can be found.

$$\begin{aligned} d\mathbf{F}_g = -\frac{\mu\mathbf{r}_{dm}}{(\mathbf{r}_{dm}\cdot\mathbf{r}_{dm})^{\frac{3}{2}}}\Bigg(1-\sum_{n=1}^{\infty}\sum_{p=0}^{n}(n+1)\left(\frac{R_M}{(\mathbf{r}_{dm}\cdot\mathbf{r}_{dm})^{\frac{1}{2}}}\right)^n\bar{P}_{np}(\sin\theta)*\ldots \\ \cdots*\left[\bar{C}_{np}\cos p\phi+\bar{S}_{np}\sin p\phi\right]\Bigg)dm \end{aligned} \tag{27}$$

For the ease of notation, define a quantity Q.

$$Q = (n+1)\,R_M^n\bar{P}_{np}(\sin\theta)\left[\bar{C}_{np}\cos p\phi+\bar{S}_{np}\sin p\phi\right] \tag{28}$$

The coupling between rotational and translational motion as a point mass's gravitational attraction acts on a rigid body spacecraft is given by Schaub and Junkins (2018). Extensions for higher order terms up to second degree and order have been presented (Scheeres et al., 1998; Scheeres, 2012; Misra et al., 2016). However, those developments only go up to

second degree and order. The following formulation can be utilized for any degree and order. In addition, the previously computed dynamics assumed that the gravitational potential, and more specifically the gravitational coefficients, were measured about a point coincident with the center of the rigid body. This causes many of the first degree and order gravitational coefficients to be zero; while this is a convenient, and justified, assumption, the following formulation can be applied when such is not the case.

3.1. Gravitational Force

For a rigid body, the total gravitational force acting on the body is given by,

$$\mathbf{F}_g = \int_{\mathcal{B}} d\mathbf{F}_g,$$

where the differential gravitational force is given in Equation (27). As such, the above expression becomes:

$$\begin{aligned}\mathbf{F}_g = \int_{\mathcal{B}} \Bigg(& -\frac{\mu \mathbf{r}_{dm}}{(\mathbf{r}_{dm}\cdot\mathbf{r}_{dm})^{\frac{3}{2}}} - \dots \\ & \cdots - \frac{\mu \mathbf{r}_{dm}}{(\mathbf{r}_{dm}\cdot\mathbf{r}_{dm})^{\frac{3}{2}}} \sum_{n=1}^{\infty}\sum_{p=0}^{n} -(n+1)\left(\frac{R_M}{(\mathbf{r}_{dm}\cdot\mathbf{r}_{dm})^{\frac{1}{2}}}\right)^n \bar{P}_{np}(\sin\theta)[\bar{C}_{np}\cos p\phi + \dots \\ & \cdots + \bar{S}_{np}\sin p\phi]\Bigg) dm\end{aligned}$$

To simplify computation, the integral is split into two terms:

$$\textbf{Term 1: } \mathbf{F}_{g1} = \int_{\mathcal{B}} -\frac{\mu \mathbf{r}_{dm}}{(\mathbf{r}_{dm}\cdot\mathbf{r}_{dm})^{\frac{3}{2}}} dm \tag{29}$$

$$\begin{aligned}\textbf{Term 2: } \mathbf{F}_{g2} = \int_{\mathcal{B}} & \frac{\mu \mathbf{r}_{dm}}{(\mathbf{r}_{dm}\cdot\mathbf{r}_{dm})^{\frac{3}{2}}} \sum_{n=1}^{\infty}\sum_{p=0}^{n}(n+1)\left(\frac{R_M}{(\mathbf{r}_{dm}\cdot\mathbf{r}_{dm})^{\frac{1}{2}}}\right)^n \bar{P}_{np}(\sin\theta) * \dots \\ & \cdots * [\bar{C}_{np}\cos p\phi \bar{S}_{np}\sin p\phi] dm\end{aligned} \tag{30}$$

Note the total gravitational force is given by the summation of the two terms.

$$\mathbf{F}_g = \mathbf{F}_{g1} + \mathbf{F}_{g2} \tag{31}$$

Consider the first term to start. The quantity $(\mathbf{r}_{dm} \cdot \mathbf{r}_{dm})^{-\frac{3}{2}}$ can be approximated using a binomial expansion for the power $-3/2$. Substituting $\mathbf{r}_{dm}$ with $\mathbf{r} + \delta\mathbf{r}$, expanding the term's dot product with itself, and then factoring out an $(\mathbf{r} \cdot \mathbf{r})^{-\frac{3}{2}}$ gives,

$$(\mathbf{r}_{dm} \cdot \mathbf{r}_{dm})^{-\frac{3}{2}} \approx \frac{1}{(\mathbf{r} \cdot \mathbf{r})^{\frac{3}{2}}} \left[1 - 3\frac{\mathbf{r} \cdot \delta\mathbf{r}}{\mathbf{r} \cdot \mathbf{r}} - \frac{3}{2}\frac{\delta\mathbf{r} \cdot \delta\mathbf{r}}{\mathbf{r} \cdot \mathbf{r}} + \frac{15}{2}\left(\frac{\mathbf{r} \cdot \delta\mathbf{r}}{\mathbf{r} \cdot \mathbf{r}}\right)^2 + \dots \right], \tag{32}$$

where only terms of up to second order terms in $\delta\mathbf{r}$ from the binomial expansion are retained. Substituting Equation (32) into Equation (29) gives the following:

$$\mathbf{F}_{g1} = -\frac{\mu}{(\mathbf{r} \cdot \mathbf{r})^{\frac{3}{2}}} \int_{\mathcal{B}} (\mathbf{r} + \delta\mathbf{r}) \left[1 - 3\frac{\mathbf{r} \cdot \delta\mathbf{r}}{\mathbf{r} \cdot \mathbf{r}} - \frac{3}{2}\frac{\delta\mathbf{r} \cdot \delta\mathbf{r}}{\mathbf{r} \cdot \mathbf{r}} + \frac{15}{2}\left(\frac{\mathbf{r} \cdot \delta\mathbf{r}}{\mathbf{r} \cdot \mathbf{r}}\right)^2 \right] dm$$

The terms are distributed and simplified, giving the final gravitational force for the first term (Schaub & Junkins, 2018).

$$\mathbf{F}_{g1} = -\frac{\mu m}{(\mathbf{r} \cdot \mathbf{r})^{\frac{3}{2}}} \left(1 + \frac{3}{m\,(\mathbf{r} \cdot \mathbf{r})} \left[J + \frac{1}{2}\left(\mathrm{tr}(J) - \frac{5\mathbf{r}^T J \mathbf{r}}{\mathbf{r} \cdot \mathbf{r}} \right) I_3 \right] \right) \mathbf{r} \tag{33}$$

Note that Term 1 is identical to the expression given in Equation (23b), which describes the coupled gravitational effects of a a uniform gravitational field. Now consider Term 2. By substituting Q from Equation (28) into Equation (30), the latter term can be rewritten.

$$\textbf{Term 2:} \qquad \mathbf{F}_{g2} = \mu \sum_{n=1}^{\infty} \sum_{p=0}^{n} \int_{\mathcal{B}} \frac{Q\mathbf{r}_{dm}}{(\mathbf{r}_{dm} \cdot \mathbf{r}_{dm})^{\frac{n+3}{2}}} dm \tag{34}$$

Also note the change in the order of the summation and integral notation. Given that the series summations will be finite in practical applications and the integral is finite, this change is justified. Approximating $(\mathbf{r}_{dm} \cdot \mathbf{r}_{dm})^{-\frac{n+3}{2}}$ using a binomial expansion of the power $-\frac{n+3}{2}$ and retaining second order terms simplifies the integral.

$$\begin{aligned} (\mathbf{r}_{dm} \cdot \mathbf{r}_{dm})^{-\frac{n+3}{2}} \approx & \frac{1}{(\mathbf{r} \cdot \mathbf{r})^{\frac{n+3}{2}}} \left[1 - \frac{(n+3)\,\mathbf{r} \cdot \delta\mathbf{r}}{\mathbf{r} \cdot \mathbf{r}} - \frac{(n+3)\,\delta\mathbf{r} \cdot \delta\mathbf{r}}{2\mathbf{r} \cdot \mathbf{r}} + \dots \right. \\ & \left. \dots + \frac{(n+3)\,(n+5)\,(\mathbf{r} \cdot \delta\mathbf{r})^2}{2\,(\mathbf{r} \cdot \mathbf{r})^2} \right] \end{aligned} \tag{35}$$

Substituting this expression into the gravitational force gives an integral in terms of $\mathbf{r}$ and $\delta\mathbf{r}$.

$$\begin{aligned}\mathbf{F}_{g2} =&\mu \sum_{n=1}^{\infty}\sum_{n=0}^{p} \frac{Q}{(\mathbf{r}\cdot\mathbf{r})^{\frac{n+3}{2}}} \int_{\mathcal{B}} (\mathbf{r}+\delta\mathbf{r}) \left[1 - \frac{(n+3)\,\mathbf{r}\cdot\delta\mathbf{r}}{\mathbf{r}\cdot\mathbf{r}} - \frac{(n+3)\,\delta\mathbf{r}\cdot\delta\mathbf{r}}{2\mathbf{r}\cdot\mathbf{r}} + \dots \right.\\ &\left. \cdots + \frac{(n+3)\,(n+5)\,(\mathbf{r}\cdot\delta\mathbf{r})^2}{2\,(\mathbf{r}\cdot\mathbf{r})^2}\right] dm\end{aligned} \tag{36}$$

Distributing and retaining up to second order terms in $\delta\mathbf{r}$ gives the following:

$$\begin{aligned}\mathbf{F}_{g2} =&\mu \sum_{n=1}^{\infty}\sum_{p=0}^{n} \frac{Q}{(\mathbf{r}\cdot\mathbf{r})^{\frac{n+3}{2}}} \left\{ \mathbf{r}\int_{\mathcal{B}} dm - \int_{\mathcal{B}} \frac{(n+3)\,(\mathbf{r}\cdot\delta\mathbf{r})\,\mathbf{r}}{\mathbf{r}\cdot\mathbf{r}} dm - \dots \right.\\ &\cdots - \int_{\mathcal{B}} \frac{(n+3)\,\mathbf{r}\,(\delta\mathbf{r}\cdot\delta\mathbf{r})}{2\mathbf{r}\cdot\mathbf{r}} dm + \int_{\mathcal{B}} \frac{(n+3)\,(n+5)\,(\mathbf{r}\cdot\delta\mathbf{r})^2\,\mathbf{r}}{2\,(\mathbf{r}\cdot\mathbf{r})^2} dm + \dots\\ &\left.\cdots + \int_{\mathcal{B}} \delta\mathbf{r} dm - \int_{\mathcal{B}} \frac{(n+3)\,(\mathbf{r}\cdot\delta\mathbf{r})\,\delta\mathbf{r}}{\mathbf{r}\cdot\mathbf{r}} dm \right\}\end{aligned} \tag{37}$$

The second and fifth terms are zero by the definition of the center of mass $\int_{\mathcal{B}} \delta\mathbf{r} dm = 0$.

$$\begin{aligned}\mathbf{F}_{g2} =&\mu \sum_{n=1}^{\infty}\sum_{p=0}^{n} \frac{Q}{(\mathbf{r}\cdot\mathbf{r})^{\frac{n+3}{2}}} \left\{ \mathbf{r}m - \frac{(n+3)}{2\mathbf{r}\cdot\mathbf{r}} \int_{\mathcal{B}} \mathbf{r}\,(\delta\mathbf{r}\cdot\delta\mathbf{r})\,dm + \dots \right.\\ &\left.\cdots + \frac{(n+3)\,(n+5)}{2\,(\mathbf{r}\cdot\mathbf{r})^2} \int_{\mathcal{B}} (\mathbf{r}\cdot\delta\mathbf{r})^2\,\mathbf{r} dm - \frac{(n+3)}{\mathbf{r}\cdot\mathbf{r}} \int_{\mathcal{B}} (\delta\mathbf{r}\cdot\mathbf{r})\,\delta\mathbf{r} dm \right\}\end{aligned} \tag{38}$$

Note the vector relationship $\delta\mathbf{r}\,(\delta\mathbf{r}\cdot\mathbf{r}) = \delta\mathbf{r}\times(\delta\mathbf{r}\times\mathbf{r}) - (\delta\mathbf{r}\cdot\delta\mathbf{r})\,\mathbf{r}$; this can be used to simplify the integral.

$$\begin{aligned}\mathbf{F}_{g2} =&\mu \sum_{n=1}^{\infty}\sum_{p=0}^{n} \frac{Q}{(\mathbf{r}\cdot\mathbf{r})^{\frac{n+3}{2}}} \left\{ \mathbf{r}m - \frac{(n+3)}{2\mathbf{r}\cdot\mathbf{r}} \int_{\mathcal{B}} \mathbf{r}\,(\delta\mathbf{r}\cdot\delta\mathbf{r})\,dm + \dots \right.\\ &\cdots + \frac{(n+3)\,(n+5)}{2\,(\mathbf{r}\cdot\mathbf{r})^2} \int_{\mathcal{B}} \mathbf{r}\cdot[\mathbf{r}\times(\delta\mathbf{r}\times\mathbf{r}) + (\delta\mathbf{r}\cdot\delta\mathbf{r})\mathbf{r}]\,\mathbf{r} dm - \dots\\ &\left.\cdots - \frac{(n+3)}{\mathbf{r}\cdot\mathbf{r}} \int_{\mathcal{B}} [\delta\mathbf{r}\times(\delta\mathbf{r}\times\mathbf{r}) + (\delta\mathbf{r}\cdot\delta\mathbf{r})\mathbf{r}]\,dm \right\}\end{aligned} \tag{39}$$

Solving the integrals yields,

$$\begin{aligned}\mathbf{F}_{g2} =&\mu \sum_{n=1}^{\infty}\sum_{p=0}^{n} \frac{Q}{(\mathbf{r}\cdot\mathbf{r})^{\frac{n+3}{2}}} \left\{ \mathbf{r}m - \frac{(n+3)}{4\mathbf{r}\cdot\mathbf{r}} \mathrm{tr}(J)\mathbf{r} + \dots \right.\\ &\left.\cdots + \frac{(n+3)\,(n+5)}{2\,(\mathbf{r}\cdot\mathbf{r})^2} \left(-\mathbf{r}^T J\mathbf{r} + \mathbf{r}^T \frac{1}{2}\mathrm{tr}(J)\mathbf{r}\right)\mathbf{r} - \frac{(n+3)}{\mathbf{r}\cdot\mathbf{r}} \left(-J + \frac{1}{2}\mathrm{tr}(J)\right)\mathbf{r} \right\}\end{aligned} \tag{40}$$

To obtain the force from higher order terms, the terms can be combined.

$$\mathbf{F}_{g2} = \mu \sum_{n=1}^{\infty} \sum_{p=0}^{n} \frac{Qm}{(\mathbf{r}\cdot\mathbf{r})^{\frac{n+3}{2}}} \left\{ 1 + \frac{(n+3)}{m\mathbf{r}\cdot\mathbf{r}} \left(J + \frac{n+2}{4} \left[\mathrm{tr}(J) - (n+5)\, \frac{\mathbf{r}^T J \mathbf{r}}{\mathbf{r}\cdot\mathbf{r}} \right] I_{3\times 3} \right) \right\} \mathbf{r} \tag{41}$$

If $\mathbf{F}_{g1}$ from Equation (33) and $\mathbf{F}_{g2}$ from Equation (41) are substituted into Equation (31), then the total gravitational force on the rigid body from a nonuniform gravitational field is found.

$$\begin{aligned} \mathbf{F}_g = & -\frac{\mu m}{(\mathbf{r}\cdot\mathbf{r})^{\frac{3}{2}}} \left(1 + \frac{3}{m\,(\mathbf{r}\cdot\mathbf{r})} \left[J + \frac{1}{2} \left(\mathrm{tr}(J) - \frac{5\mathbf{r}^T J \mathbf{r}}{\mathbf{r}\cdot\mathbf{r}} \right) I_3 \right] \right) \mathbf{r} + \dots \\ & \cdots + \mu \sum_{n=1}^{\infty} \sum_{p=0}^{n} \frac{m\,(n+1)\, R_M^n \bar{P}_{np}(\sin\theta)[\bar{C}_{np}\cos p\phi + \bar{S}_{np}\sin p\phi]}{(\mathbf{r}\cdot\mathbf{r})^{\frac{n+3}{2}}} \left\{ 1 + \dots \right. \\ & \left. \cdots + \frac{(n+3)}{m\mathbf{r}\cdot\mathbf{r}} \left(J + \frac{n+2}{4} \left[\mathrm{tr}(J) - (n+5)\, \frac{\mathbf{r}^T J \mathbf{r}}{\mathbf{r}\cdot\mathbf{r}} \right] I_{3\times 3} \right) \right\} \mathbf{r} \end{aligned} \tag{42}$$

3.2. Gravity Gradient Torque

The gravitational gradient torque is given by (Schaub & Junkins, 2018).

$$\mathbf{L}_g = \int_{\mathcal{B}} \delta\mathbf{r} \times d\mathbf{F}_g \tag{43}$$

The definition for $d\mathbf{F}_g$ from Equation (27) can be substituted into Equation (43).

$$\begin{aligned} \mathbf{L}_g = \int_{\mathcal{B}} \delta\mathbf{r} \times \Bigg(& -\frac{\mu \mathbf{r}_{dm}}{(\mathbf{r}_{dm}\cdot\mathbf{r}_{dm})^{\frac{3}{2}}} - \dots \\ & \dots + \frac{\mu \mathbf{r}_{dm}}{(\mathbf{r}_{dm}\cdot\mathbf{r}_{dm})^{\frac{3}{2}}} \sum_{n=1}^{\infty} \sum_{p=0}^{n} (n+1) \left(\frac{R_M}{(\mathbf{r}_{dm}\cdot\mathbf{r}_{dm})^{\frac{1}{2}}} \right)^n \bar{P}_{np}(\sin\theta)[\bar{C}_{np}\cos p\phi + \dots \\ & \cdots + \bar{S}_{np}\sin p\phi] \Bigg) dm \end{aligned} \tag{44}$$

The integrand is simplified and the order of the cross product is reversed.

$$\begin{aligned} \mathbf{L}_g = \int_{\mathcal{B}} \Bigg(& \frac{\mu\,(\mathbf{r}+\delta\mathbf{r})}{(\mathbf{r}_{dm}\cdot\mathbf{r}_{dm})^{\frac{3}{2}}} - \dots \\ & \dots - \frac{\mu\,(\mathbf{r}+\delta\mathbf{r})}{(\mathbf{r}_{dm}\cdot\mathbf{r}_{dm})^{\frac{3}{2}}} \sum_{n=1}^{\infty} \sum_{p=0}^{n} (n+1) \left(\frac{R_M}{(\mathbf{r}_{dm}\cdot\mathbf{r}_{dm})^{\frac{1}{2}}} \right)^n \bar{P}_{np}(\sin\theta)[\bar{C}_{mp}\cos p\phi + \dots \\ & \cdots + \bar{S}_{np}\sin p\phi] \Bigg) \times \delta\mathbf{r} dm \end{aligned} \tag{45}$$

The cross product can be distributed and the integral separated, leaving two terms.

$$\textbf{Term 1:} \qquad \mathbf{L}_{g1} = \int_{\mathcal{B}} \left(\frac{\mu \left(\mathbf{r} + \delta\mathbf{r} \right)}{\left(\mathbf{r}_{dm} \cdot \mathbf{r}_{dm} \right)^{\frac{3}{2}}} \right) \times \delta\mathbf{r} dm \tag{46}$$

$$\begin{aligned} \textbf{Term 2:} \, \mathbf{L}_{g2} = \int_{\mathcal{B}} \Bigg(& -\frac{\mu \left(\mathbf{r} + \delta\mathbf{r} \right)}{\left(\mathbf{r}_{dm} \cdot \mathbf{r}_{dm} \right)^{\frac{3}{2}}} \sum_{l=1}^{\infty} \sum_{m=0}^{l} (l+1) \left(\frac{R_M}{\left(\mathbf{r}_{dm} \cdot \mathbf{r}_{dm} \right)^{\frac{1}{2}}} \right)^{l} \bar{P}_{lm}(\sin\theta) * \ldots \\ & \cdots * \left[\bar{C}_{lm} \cos m\phi + \bar{S}_{lm} \sin m\phi \right] \Bigg) \times \delta\mathbf{r} dm \end{aligned} \tag{47}$$

Consider Term 1. Distribute the cross product and rearrange the corresponding terms, noting that $\delta\mathbf{r} \times \delta\mathbf{r}$ is zero, to obtain the following:

$$\textbf{Term 1:} \qquad \mathbf{L}_{g1} = \mu\mathbf{r} \times \int_{\mathcal{B}} \frac{\delta\mathbf{r}}{\left(\mathbf{r}_{dm} \cdot \mathbf{r}_{dm} \right)^{\frac{3}{2}}} dm \tag{48}$$

As seen above, the quantity $\left(\mathbf{r}_{dm} \cdot \mathbf{r}_{dm} \right)^{-\frac{3}{2}}$ can be approximated using a binomial expansion for the power $-3/2$. Substituting this expansion from Equation (32) where only first order terms in $\delta\mathbf{r}$ are retained, the torque is given in terms of $\mathbf{r}$ and $\delta\mathbf{r}$.

$$\mathbf{L}_{g1} = \frac{\mu\mathbf{r}}{\left(\mathbf{r} \cdot \mathbf{r} \right)^{\frac{3}{2}}} \times \int_{\mathcal{B}} \delta\mathbf{r} \left[1 - 3\frac{\mathbf{r} \cdot \delta\mathbf{r}}{\mathbf{r} \cdot \mathbf{r}} \right] dm \tag{49}$$

Note that $\int_{\mathcal{B}} \delta\mathbf{r} dm = 0$. Employing the same vector relationship from the gravitational force case, $-\delta\mathbf{r} \left(\delta\mathbf{r} \cdot \mathbf{r} \right) = -\delta\mathbf{r} \times \left(\delta\mathbf{r} \times \mathbf{r} \right) + \left(\delta\mathbf{r} \cdot \delta\mathbf{r} \right) \mathbf{r}$, the torque is simplified.

$$\mathbf{L}_{g1} = \frac{3\mu\mathbf{r}}{\left(\mathbf{r} \cdot \mathbf{r} \right)^{\frac{5}{2}}} \times \int_{\mathcal{B}} - \left(\delta\mathbf{r} \times \left(\delta\mathbf{r} \times \mathbf{r} \right) + \left(\delta\mathbf{r} \cdot \delta\mathbf{r} \right) \mathbf{r} \right) dm \tag{50}$$

The second term in the integral is zero, such that only the first term remains. This term is expanded using the $(\cdot)^{\times}$ mapping.

$$\mathbf{L}_{g1} = \frac{3\mu\mathbf{r}}{\left(\mathbf{r} \cdot \mathbf{r} \right)^{\frac{5}{2}}} \times \int_{\mathcal{B}} -\delta\mathbf{r}^{\times} \delta\mathbf{r}^{\times} dm\mathbf{r} \tag{51}$$

Observing that the integral is defined as the moment of inertia matrix, the first term of the gravity gradient torque is given as follows:

$$\textbf{Term 1:} \qquad \mathbf{L}_{g1} = \frac{3\mu\mathbf{r}}{(\mathbf{r}\cdot\mathbf{r})^{\frac{5}{2}}} \times J\mathbf{r} \tag{52}$$

Note that Term 1 is equivalent to Equation (23a) for a uniform gravitational field. Now consider Term 2. This can be rewritten using the definition of Q.

$$\textbf{Term 2:} \qquad \mathbf{L}_{g2} = \int_{\mathcal{B}} \left(-\mu \left(\mathbf{r} + \delta\mathbf{r}\right) \sum_{n=1}^{\infty} \sum_{p=0}^{n} \frac{Q}{\left(\mathbf{r}_{dm}\cdot\mathbf{r}_{dm}\right)^{\frac{n+3}{2}}} \right) \times \delta\mathbf{r} dm \tag{53}$$

If the cross product is distributed and the appropriate cancellations and rearrangements are taken, the torque can be rewritten.

$$\mathbf{L}_{g2} = -\mu\mathbf{r} \sum_{n=1}^{\infty} \sum_{p=0}^{n} Q \times \int_{\mathcal{B}} \frac{\delta\mathbf{r}}{\left(\mathbf{r}_{dm}\cdot\mathbf{r}_{dm}\right)^{\frac{n+3}{2}}} dm \tag{54}$$

Employing the same binomial expansion as given above and substituting gives a simpler integral.

$$\mathbf{L}_{g2} = -\mu\mathbf{r} \sum_{n=1}^{\infty} \sum_{p=0}^{n} \frac{Q}{\left(\mathbf{r}\cdot\mathbf{r}\right)^{\frac{n+3}{2}}} \times \int_{\mathcal{B}} \left[1 - \frac{(n+3)\,\mathbf{r}\cdot\delta\mathbf{r}}{\mathbf{r}\cdot\mathbf{r}} \right] \delta\mathbf{r} dm \tag{55}$$

Simplifying and applying the vector relationship from before gives the following.

$$\mathbf{L}_{g2} = -\mu\mathbf{r} \sum_{n=1}^{\infty} \sum_{p=0}^{n} \frac{Q\,(n+3)}{\left(\mathbf{r}\cdot\mathbf{r}\right)^{\frac{n+5}{2}}} \times \int_{\mathcal{B}} -\delta\mathbf{r} \times (\delta\mathbf{r} \times \mathbf{r}) + (\delta\mathbf{r}\cdot\delta\mathbf{r})\,\mathbf{r} dm \tag{56}$$

The second term in the integrand is cancelled the remaining terms are expanded.

$$\mathbf{L}_{g2} = -\mu\mathbf{r} \sum_{n=1}^{\infty} \sum_{p=0}^{n} \frac{Q\,(n+3)}{\left(\mathbf{r}\cdot\mathbf{r}\right)^{\frac{n+5}{2}}} \times \int_{\mathcal{B}} -\delta\mathbf{r}^{\times}\delta\mathbf{r}^{\times} dm\mathbf{r} \tag{57}$$

As before, the moment of inertia tensor integral appears. With this relationship, the final form of Term 2 is obtained.

$$\begin{aligned} \mathbf{L}_{g2} = &- \frac{\mu\mathbf{r}}{\left(\mathbf{r}\cdot\mathbf{r}\right)^{\frac{5}{2}}} \sum_{n=1}^{\infty} \sum_{p=0}^{n} (n+1)\,(n+3) \left(\frac{R_M}{\left(\mathbf{r}\cdot\mathbf{r}\right)^{\frac{1}{2}}} \right)^{n} \bar{P}_{np}(\sin\theta) [\bar{C}_{np}\cos p\phi + \dots \\ &\cdots + \bar{S}_{np}\sin p\phi] \times J\mathbf{r} \end{aligned} \tag{58}$$

Thus, after applying the $(\cdot)^{\times}$ mapping, the total torque is given as follows:

$$\mathbf{L}_g = \frac{\mu r^{\times}}{(\mathbf{r}\cdot\mathbf{r})^{\frac{5}{2}}}\left[3 - \sum_{n=1}^{\infty}\sum_{p=0}^{n}(n+1)\,(n+3)\left(\frac{R_M}{(\mathbf{r}\cdot\mathbf{r})^{\frac{1}{2}}}\right)^{n}\bar{P}_{np}(\sin\theta)[\bar{C}_{np}\cos p\phi + \ldots \right.$$
$$\left. \cdots + \bar{S}_{np}\sin p\phi]\right] J\mathbf{r} \tag{59}$$

3.3. Longitude and Latitude Determination

The position of a spacecraft expressed in the central body's fixed frame $\mathcal{F}$ is given in terms of the magnitude of the position vector r, the latitude of the spacecraft θ, and its longitude ϕ.

$$\mathbf{r}_{\mathcal{F}} = \begin{bmatrix} r\cos\theta\cos\phi \\ r\cos\theta\sin\phi \\ r\sin\theta \end{bmatrix} \tag{60}$$

This position vector $\mathbf{r}_{\mathcal{F}}$ is related to the inertial position $\mathbf{r}$ by the rotation matrix from $\mathcal{N}$ to $\mathcal{F}$ denoted $R_{\mathcal{F}\mathcal{N}}$.

$$\mathbf{r} = R_{\mathcal{F}\mathcal{N}}^{-1}\mathbf{r}_{\mathcal{F}} \tag{61}$$

Expressing this matrix in this form is useful because it is directly inherited from the properties of the celestial body. For example, in the following analyses, the central body is taken to be the Moon. Furthermore, it is assumed it rotates simply about its third axis with the rotational rate of the Moon about the $\mathcal{N}$ and $\mathcal{F}$ coincident third axis by the rotation angle η given by $R_{\mathcal{F}\mathcal{N}}(\eta)$. Pre-multiplying the position vector by the rotation matrix from the $\mathcal{N}$ to the $\mathcal{F}$ frame will give the necessary vector to find the longitude and latitude. With the vector expressed in this frame, the longitude and latitude can be determined.

$$\theta = \arcsin\left(\frac{r_{\mathcal{F}_3}}{||\mathbf{r}_{\mathcal{F}}||}\right), \tag{62a}$$

$$\phi = \arctan_2\left(\frac{r_{\mathcal{F}_2}}{r_{\mathcal{F}_1}}\right), \tag{62b}$$

Here, $r_{\mathcal{F}_i}$ for $i = 1, 2, 3$ indicates the i^{th} component of $\mathbf{r}_{\mathcal{F}}$ and $\arctan_2$ denotes the four quadrant inverse tangent. Recall that longitude is bounded between -180° and 180° and that latitude is bounded between -90° and 90°.

3.4. Numerical Simulations and Discussion

To look at the effects of this formulation over the course of a lunar orbit, consider the case of a spacecraft in lunar orbit. The violent formation of the Moon and lack of atmosphere led to dense concentrations of mass spattered across its surface. The presence of these mass concentrations on the Moon leads to large gravitational perturbations except at a handful of frozen orbits (Elipe & Lara, 2003). Gravitational potential models of degree 900 and higher have been developed by Konopliv et al. (2013) and Lemoine et al. (2014, 2013) as part of the Gravity Recovery and Interior Laboratory (GRAIL) mission. Spacecraft in lunar orbits are primarily governed by lunar gravity, and the effects of the Earth and Sun can be neglected while maintaining sufficient accuracy for early mission planning (Knežević & Milani, 1998). Therefore, it is assumed in numerical simulations here that the only force acting on the rigid body is the lunar gravitational force. Apollo 16 released a small subsatellite into a roughly circular orbit inclined at approximately 11°. After several weeks, the spacecraft crashed into the surface due to the perturbations. Furthermore, the spacecraft had a periselene altitude of 90km and an aposelene altitude of 130km (Bell, 2020). Assuming all other orbital elements were zero, the spacecraft motion in lunar orbit can be simulated. For all of the simulations presented in this thesis involving spacecraft in lunar orbits, unless otherwise specified, the mass properties for the spacecraft are assumed to be those of the Apollo Lunar Module from Low (1969) and Zupp (January 2013).

$$m = 7063\ kg \qquad J = \begin{bmatrix} 17058.9014 & 246.758867 & 752.478961 \\ 246.758867 & 18801.1275 & 100.330528 \\ 752.478961 & 100.330528 & 21969.674 \end{bmatrix} kg\ m^2$$

The spacecraft initial conditions are taken to start at periselene. Correspondingly, the initial configuration and velocity of the spacecraft are given as follows:

$$\mathbf{V} = \begin{bmatrix} 0 \\ 0 \\ 9.03813 \times 10^{-4} \\ 0 \\ -1.64863 \times 10^{3} \\ 0 \end{bmatrix} \qquad g = \begin{bmatrix} -1 & 0 & 0 & 1.824 \times 10^{6} \\ 0 & -0.98163 & -0.19081 & 0 \\ 0 & -0.19081 & 0.98163 & 0 \\ 0 & 0 & 0 & 1 \end{bmatrix}$$

Figure 3.1 shows the difference in position between different orders of spherical harmonics in the nonuniform gravitational model and the uniform gravitational model. The main observation is that the position changes by almost four kilometers during one orbital period. It exhibits a periodic behavior, but examining the position alone, it is clear the effects of such a gravitational field must be accounted for. Failure to do so is what caused the degradation of the Apollo 16 subsatellite, prompting exploration into and discovery of lunar mass concentrations. Figure 3.2 illustrates that the deviations in velocity are small for the

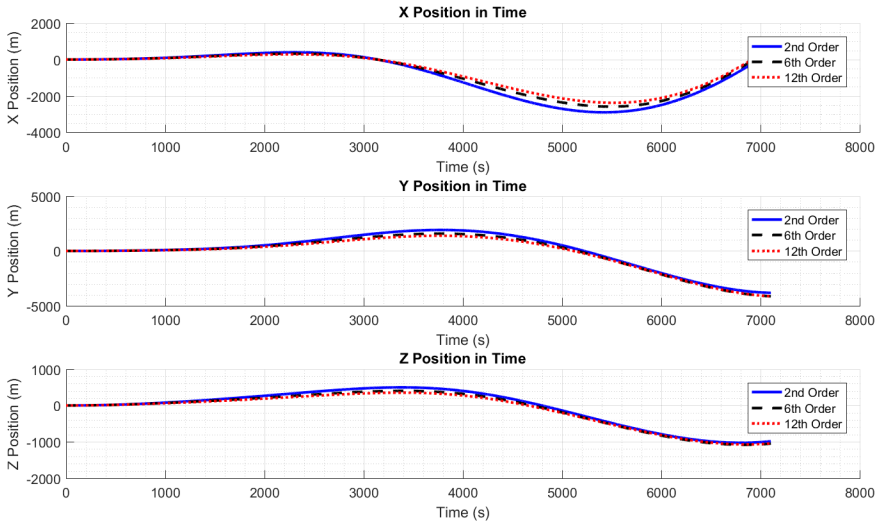

Figure 3.1 Position Comparison with Uniform Gravitational Field

scale of orbital velocities, but not negligible.

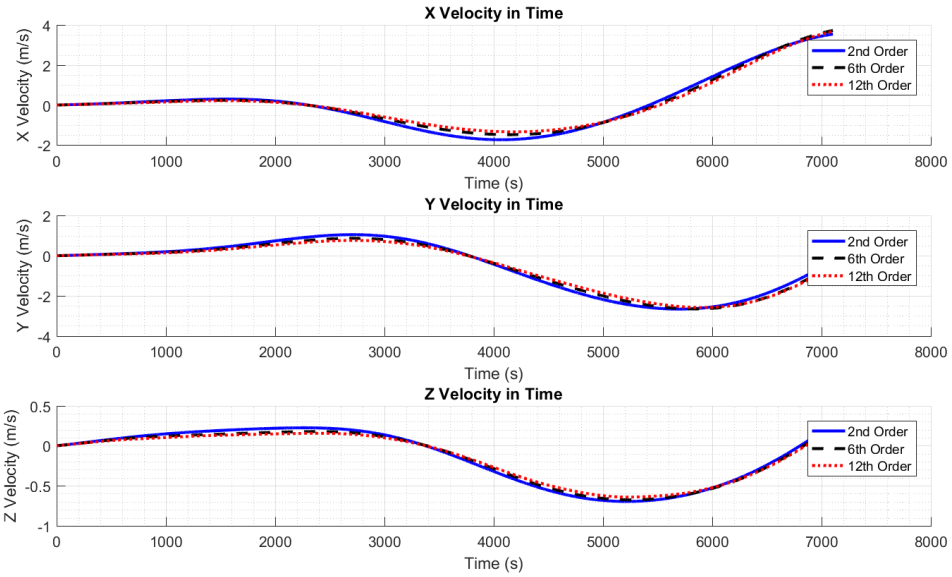

Figure 3.2 Velocity Comparison with Uniform Gravitational Field

Figure 3.3 shows the difference in Euler angles between the different harmonic degrees that were chosen and the uniform field. The angular changes from the nominal case are in the neighborhood of one-twentieth of a degree, three arcmin, or 180 arcsec. These errors are within common pointing accuracies for different spacecraft. For example, the Lunar Reconnaissance Orbiter had several instruments, one of which was the Lunar Orbiter Laser Altimeter (LOLA) that gathered topography data accurate to within meters (Barker et al., 2016). Such precise measurements necessitated a pointing accuracy of 15 arcsec or slightly over four-thousandths of a degree (Shah et al., 2010). In the case of that spacecraft, failure to capture higher order gravitational terms could have led to science objective failures, per Figure 3.3.

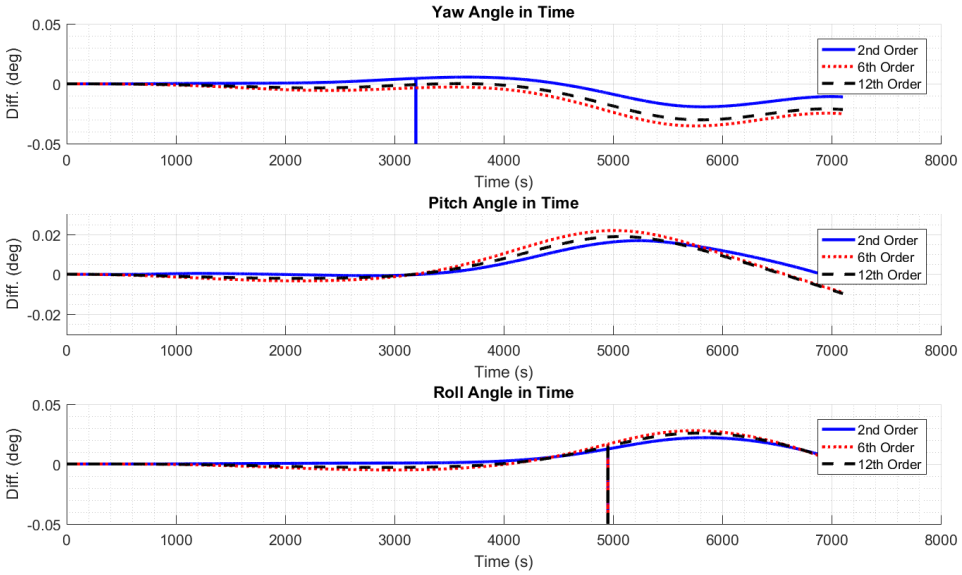

Figure 3.3 Attitude Comparison with Uniform Gravitational Field

Similar to the Euler angles, the differences in angular velocities are seen by plotting the comparison between the orders, as seen in Figure 3.4.

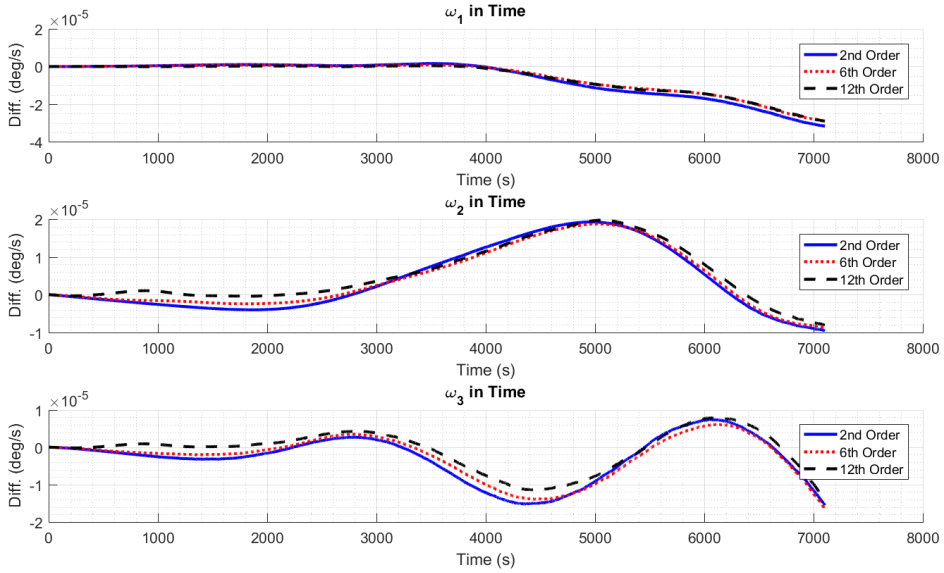

Figure 3.4 Angular Velocity Comparison with Uniform Gravitational Field

In general, using these higher order terms provides small changes in accuracy for the system dynamics; however, considering the disturbances seen over only one orbit period, planning for these disturbances in coupled roto-translational motion is vital for mission planning and spacecraft longevity.

4. Constrained Motion Analysis in the Geometric Mechanics Framework

While the original Udwadia-Kalaba (UK) formulation was initially developed for point masses, since it utilizes generalized accelerations, it can be extended to other systems where accelerations occur. Here, UK formulation is generalized to constrain rigid body motion. Within the geometric mechanics framework, there are two different spaces where accelerations occur; these include the six-dimensional Euclidean space $\mathbb{R}^6$ and the double tangent bundle of SE(3), $T^2SE(3)$. In this section, the generalization of the UK formulation to geometric mechanics (GMUK) is presented for both of these spaces.

4.1. Constrained Motion on Six Dimensional Euclidean Space

In this section, the constraints of motion dynamics of the rigid body spacecraft are defined and formulated in the geometric mechanics framework on $\mathbb{R}^6$. In the fully constrained case, all six degrees of freedom of the spacecraft are specified by the constraints. Therefore, the number of constraints in the system is $s < 6$ for underconstrained case, $s = 6$ for fully constrained case, and $s > 6$ for overconstrained cases.

4.1.1. Determination of the Constraint Equation

In general, for n rigid body spacecraft, it can be shown that the constraint equation can be written in the form of Equation (1).

$$A\dot{\tilde{\mathbf{V}}} = \mathbf{b}, \tag{63}$$

where $\dot{\tilde{\mathbf{V}}} = [\dot{\mathbf{V}}_1^T, \ldots, \dot{\mathbf{V}}_n^T]^T \in \mathbb{R}^{6n}$, $A \in \mathbb{R}^{s\times 6n}$ and $\mathbf{b} \in \mathbb{R}^s$ depend on the system constraints. Taking the constraint equation, substituting for $\dot{\tilde{\mathbf{V}}} = \dot{\tilde{\mathbf{V}}}_a + \dot{\tilde{\mathbf{V}}}_c$ and rearranging, the constraint equation is altered.

$$A\dot{\tilde{\mathbf{V}}}_c = \mathbf{b} - A\dot{\tilde{\mathbf{V}}}_a$$

This can be re-expressed as follows:

$$A\bar{\mathbb{I}}^{-\frac{1}{2}}\bar{\mathbb{I}}^{\frac{1}{2}}\dot{\tilde{\mathbf{V}}}_c = \mathbf{b} - A\dot{\tilde{\mathbf{V}}}_a,$$

where $\bar{\mathbb{I}} = \text{blkdiag}(\mathbb{I}_1 \ldots \mathbb{I}_n)$. After employing the substitution $y = \bar{\mathbb{I}}^{\frac{1}{2}} \dot{\dot{\mathbf{V}}}_c$, it can be seen:

$$A\bar{\mathbb{I}}^{-\frac{1}{2}} y = \mathbf{b} - A\dot{\dot{\mathbf{V}}}_a$$

To apply the properties of the Moore-Penrose generalized inverse as in Udwadia and Kalaba (2008), it is required that:

$$A\bar{\mathbb{I}}^{-\frac{1}{2}} \left(A\bar{\mathbb{I}}^{-\frac{1}{2}}\right)^{+} \left(\mathbf{b} - A\dot{\dot{\mathbf{V}}}_a\right) = \mathbf{b} - A\dot{\dot{\mathbf{V}}}_a$$

It can be seen that the expression for y above is equivalent to,

$$y = \left(A\bar{\mathbb{I}}^{-\frac{1}{2}}\right)^{+} \left(\mathbf{b} - A\dot{\dot{\mathbf{V}}}_a\right)$$

Relating expressions for y, the control acceleration can be found.

$$\dot{\dot{\mathbf{V}}}_c = \bar{\mathbb{I}}^{-\frac{1}{2}} \left(A\bar{\mathbb{I}}^{-\frac{1}{2}}\right)^{+} \left(\mathbf{b} - A\dot{\dot{\mathbf{V}}}_a\right)$$

A symmetric form of the equation is derived by Udwadia and Kalaba (2008). Therefore, the constraint acceleration can also be obtained similar to that in Equation (2).

$$\dot{\dot{\mathbf{V}}}_c = \bar{\mathbb{I}}^{-1} A^T \left(A\bar{\mathbb{I}}^{-1} A^T\right)^{+} \left(\mathbf{b} - A\dot{\dot{\mathbf{V}}}_a\right) \quad \in \mathbb{R}^6, \tag{64}$$

Here, $\dot{\dot{\mathbf{V}}}_a = [(\mathbb{I}_1^{-1} \text{ad}^*_{\mathbf{V}_1} \mathbb{I}_1 \mathbf{V}_1 + \mathbb{I}^{-1} \boldsymbol{\tau}_1)^T, \ldots, (\mathbb{I}_n^{-1} \text{ad}^*_{\mathbf{V}_n} \mathbb{I}_n \mathbf{V}_n + \mathbb{I}^{-1} \boldsymbol{\tau}_n)^T]^T$.

4.1.2. Fully-Constrained Case

For many missions, keeping a spacecraft pointed toward the central body is important. Many mapping and observation satellites are required to keep tremendous pointing accuracy for efficient measurements. For example, the Lunar Reconnaissance Orbiter (LRO) was designed to operate within a pointing accuracy of 15 arcsec or slightly over four-thousandths of a degree (Shah et al., 2010). LRO had several instruments, one of which was the Lunar Orbiter Laser Altimeter (LOLA) that gathered topology data accurate to within meters (Barker et al., 2016). To accomplish this, the spacecraft had to have sufficient pointing accuracy.

There are three reference frames used in this analysis: the Lunar Centered Inertial (LCI) frame $\mathcal{N}$, the perifocal frame $\mathcal{P}$ of the desired orbit, and the spacecraft body frame $\mathcal{B}$. A graphical representation of these three frames is provided in Fig. 4.1, where the subscripts 1, 2, and 3 denote the basis vectors of each reference frame. Note that the inertial frame need not be only around the Moon. This formulation holds for any orbit around any central body; however, the simulations presented are for the case of a spacecraft in lunar orbit, so the LCI frame is introduced here first.

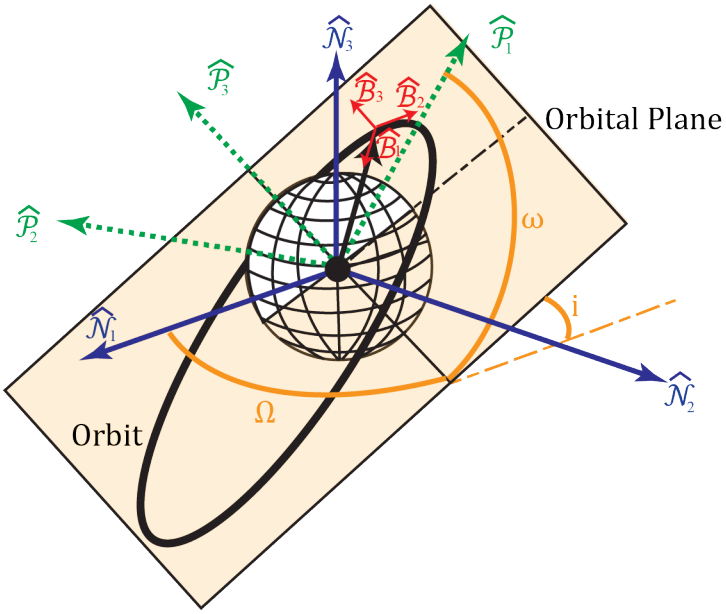

Figure 4.1 Inertial $\mathcal{N}$, Perifocal $\mathcal{P}$, and Body $\mathcal{B}$ Reference Frames

To keep a spacecraft constrained to point toward its orbiting body, it is required for the spacecraft body's first axis $\hat{\mathcal{B}}_1$ to point opposite the position vector $\mathbf{r}$, the second axis $\hat{\mathcal{B}}_2$ to be normal to the first axis and in the orbital plane, and the third axis $\hat{\mathcal{B}}_3$ to be aligned with the angular momentum vector, as shown in Fig. 4.1. This amounts to describing the LVLH frame with a rotation of 180° about the angular momentum vector in this frame. Formulating this problem within the perifocal frame lends itself to accommodating eccentric and inclined orbits.

Consider a single, fully constrained rigid body spacecraft shown in Figure 4.1 confined to move in the orbit with its $\mathcal{B}$ frame coordinates always constrained to be aligned in the

directions shown. Note that in this case, $n = 1$ in Equation (64). In order to formulate the constrained motion in the GMUK framework, the desired states of a rigid body spacecraft are fully specified by (g_d, V_d), where g_d denotes the desired configuration given in the form of Equation (6) and V_d is the desired augmented velocity given in the form of Equation (9). Both quantities are obtained by following Kepler's laws of orbital motion. For the motion to be completely defined, only holonomic constraints are necessary to utilize this GMUK formulation.

Differentiating the holonomic constraint of $g = g_d$ twice and using Equation (10a) yields the following:

$$g\mathbf{V}^{\vee^2} + g\dot{\mathbf{V}}^{\vee} = g_d\mathbf{V}_d^{\vee^2} + g_d\dot{\mathbf{V}}_d^{\vee} \tag{65}$$

Solving Equation (65) for $\dot{\mathbf{V}}$, the holonomic constraint above can be written in the vector form.

$$\dot{\mathbf{V}} = \left(g^{-1}g_d(\mathbf{V}_d^{\vee^2} + \dot{\mathbf{V}}_d^{\vee}) - \mathbf{V}^{\vee^2}\right)^{|} \tag{66}$$

Hence, in this case, A and $\mathbf{b}$ in Equation (63) can be obtained.

$$A = I_6, \quad \mathbf{b} = \left(g^{-1}g_d(\mathbf{V}_d^{\vee^2} + \dot{\mathbf{V}}_d^{\vee}) - \mathbf{V}^{\vee^2}\right)^{|} \in \mathbb{R}^6 \tag{67}$$

The desired configuration relative to the perifocal frame $\mathcal{P}$ is given in the form of Equation (6), i.e.,

$$g_{d/\mathcal{P}} = \begin{bmatrix} R_{d/\mathcal{P}} & \mathbf{r}_{d/\mathcal{P}} \\ 0_{1\times 3} & 1 \end{bmatrix}, \tag{68}$$

where, from Vallado (2013),

$$R_{d/\mathcal{P}} = \begin{bmatrix} -\cos f & -\sin f & 0 \\ \sin f & -\cos f & 0 \\ 0 & 0 & 1 \end{bmatrix}, \qquad \mathbf{r}_{d/\mathcal{P}} = \frac{h^2}{\mu(1 + e\cos f)}[\cos f,\ \sin f,\ 0]^T \tag{69}$$

Examining the rotation matrix in Equation (69), it takes the form of a negative third axis rotation as a function of true anomaly. This is the negative rotation matrix needed to transform from the perifocal frame to the modified LVLH frame previously described. This points the body's first axis opposite the position vector, as desired and seen in Figure 4.1. Then, the desired configuration is obtained.

$$g_d = g_{\mathcal{P}} g_{d/\mathcal{P}}, \tag{70}$$

Here, $g_{\mathcal{P}}$ is comprised of the 3-1-3 Euler angle rotation matrix from the perifocal frame to the inertial frame $R_{\mathcal{N}\mathcal{P}}$ and the relative position. Note that since both frames' origins are at the center of mass of the orbited body, the relative position vector is $\mathbf{0}$ and therefore $\mathbf{r}_d = R_{\mathcal{N}\mathcal{P}}\mathbf{r}_{d/\mathcal{P}}$. Examining Equation (69), it can be seen that an eccentricity of zero will reduce the desired position in the perifocal frame to being on a circle. Furthermore, examining the definition of $g_{\mathcal{P}}$, if the inclination is zero, and maintaining the circularity condition, $g_{\mathcal{P}}$ is equivalent to the inertial frame with a third axis rotation. Once again considering the constraint $g = g_d = g_{\mathcal{P}} g_{d/\mathcal{P}}$, finding the values of $\mathbf{V}_d$ and $\dot{\mathbf{V}}_d$ requires determination of $\mathbf{V}_{d/\mathcal{P}}$ and $\dot{\mathbf{V}}_{d/\mathcal{P}}$. Relative to the $\mathcal{P}$ frame, the spacecraft is spinning about its third axis at a rate equal to $\dot{f}$, and there is no other angular velocity. In addition, the translational velocity in the perifocal frame is given by $\mathbf{v}_{d/\mathcal{P}}$. In order to express this value as a member of $\mathbf{V}_{d/\mathcal{P}}$, this velocity relative to the perifocal frame must be expressed in the spacecraft body frame $\mathcal{B}$. Therefore, the desired velocity relative to the $\mathcal{P}$ frame can be determined.

$$\mathbf{V}_{d/\mathcal{P}} = \begin{bmatrix} \omega_{d/\mathcal{P}} \\ R_{d/\mathcal{P}}^T \mathbf{v}_{d/\mathcal{P}}, \end{bmatrix}, \tag{71}$$

Note that $\omega_{d/\mathcal{P}} = [0,\ 0,\ \dot{f}]^T$ and the rate of change of true anomaly f is given as follows:

$$\dot{f} = \frac{\mu^2}{h^3}(1 + e\cos f)^2$$

Then, Equation (71) is differentiated with respect to time.

$$\dot{\mathbf{V}}_{d/\mathcal{P}} = \begin{bmatrix} \dot{\omega}_{d/\mathcal{P}} \\ R^T_{d/\mathcal{P}}\dot{\mathbf{v}}_{\mathcal{P}} + R^T_{d/\mathcal{P}}\omega^{\times}_{d/\mathcal{P}}\mathbf{v}_{d/\mathcal{P}} \end{bmatrix}, \tag{72}$$

Here $\dot{\omega}_{d/\mathcal{P}} = [0,\ 0,\ \ddot{f}]^T$,

$$\ddot{f} = -\frac{2\mu^4}{h^6}(1 + e\cos f)^3 e \sin f,$$

and,

$$\dot{\mathbf{v}}_{d/\mathcal{P}} = -\frac{\mu^3}{h^4}(1 + e\cos f)^2[\cos f,\ \sin f,\ 0]^T$$

It is necessary to find the value of $\dot{\mathbf{V}}_d$ from the above relations, which is given by the derivative of the relative velocity expression.

$$\mathbf{V}_d = \mathbf{V}_{d/\mathcal{P}} + \mathrm{Ad}_{g^{-1}_{d/\mathcal{P}}}\mathbf{V}_{\mathcal{P}}, \tag{73}$$

$$\dot{\mathbf{V}}_d = \dot{\mathbf{V}}_{d/\mathcal{P}} - \mathrm{Ad}_{g^{-1}_{d/\mathcal{P}}}\dot{\mathbf{V}}_{\mathcal{P}} + \mathrm{ad}_{\mathbf{V}_{d/\mathcal{P}}}\mathrm{Ad}_{g^{-1}_{d/\mathcal{P}}}\mathbf{V}_{\mathcal{P}} \tag{74}$$

Then, the constraint translational and rotational control accelerations $\mathbf{a}_c$ required to maintain the desired motion for this fully-constrained scenario are obtained using Equations (64), (67), (70), (73), and (74).

It is important to highlight that this formulation requires determination of the true anomaly as a function of time. Given the semimajor axis for the elliptical orbit, the mean motion can be determined.

$$n_{mm} = \sqrt{\frac{\mu}{a^3}} \tag{75}$$

From the expression for mean motion, the mean anomaly M is obtained

$$M = n_{mm}t \tag{76}$$

The mean anomaly is related to the eccentric anomaly E by Kepler's equation.

$$M = E - e\sin E \tag{77}$$

This requires a numerical method to solve for E, such as the Newton-Raphson method. Finally, the eccentric anomaly is related to the true anomaly, thereby relating time to true anomaly.

$$f = 2\arctan\left(\tan\left(\frac{E}{2}\right)\sqrt{\frac{1+e}{1-e}}\right) \tag{78}$$

4.1.3. Underconstrained Case

For the underconstrained, elliptical, inclined orbit case (UCEI), choosing the constraints becomes somewhat more difficult than the fully constrained system. It is convenient when all the motion is fixed in one orientation with respect to one reference frame. However, if motion is constrained in more than one reference frame, there may be a components of the motion that are constrained in two different reference frames. For example, consider a spacecraft free to rotate around its first body axis $\mathcal{B}_1$; it is still required to rotate around the perifocal frame's third axis $\hat{P}_3$ at an angular speed equal to the rate of change of the true anomaly. The third axis constraint cannot be imposed on the body's angular velocity as the rotation about the $\mathcal{B}_1$ axis will change how the spacecraft is oriented with respect to the perifocal frame. In the fully constrained case, such issues could be neglected as the perifocal frame was stationary, thus Equation (73) and (74) could be simplified to the relative velocities. Consider the case of two rigid bodies with configurations g_1 and g_2 and velocities $\mathbf{V}_1$ and $\mathbf{V}_2$. Employing Equation (73), expanding in terms of the velocity vector, and combining yields the following:

$$\begin{bmatrix}\omega_1\\ \mathbf{v}_1\end{bmatrix} = \begin{bmatrix}\omega_{1/2} + R_1^T R_2 \omega_2\\ \mathbf{v}_{1/2} - (\mathbf{r}_1 - \mathbf{r}_2)^\times R_1^T R_2 \omega_2 + R_1^T R_2 \mathbf{v}_2\end{bmatrix}$$

The important factor to consider is that the coupling that makes the usage of geometric mechanics beneficial has the consequence that underconstraining the system becomes more difficult. Therefore, the constraints must be posed in a reference frame such that the degrees of freedom do not exhibit constraint coupling.

Let the modified LVLH frame, which was the desired body frame in the fully constrained case, be denoted by the $\mathcal{L}$ frame. Assume there is a fully constrained virtual spacecraft given by the configuration $g_{\mathcal{L}}$ with velocity $\mathbf{V}_{\mathcal{L}}$ in this frame.

$$\mathbf{V}_{\mathcal{L}} = \mathbf{V}_{\mathcal{L}/\mathcal{P}} + \mathrm{Ad}_{g_{\mathcal{L}/\mathcal{P}}^{-1}} \mathbf{V}_{\mathcal{P}}$$

Also assume the virtual spacecraft and the actual spacecraft have identical mass properties and initial conditions. Hence, the velocity of the real spacecraft in $\mathcal{B}$ with respect to the virtual spacecraft described in the $\mathcal{L}$ frame is desired to be $\mathbf{V}_{\mathcal{B}/\mathcal{L}} = [\omega_f, 0, 0, 0, 0, 0]^T$, where the subscript f denotes the free motion. Since the motion of the real spacecraft is constrained relative to the virtual spacecraft and the virtual spacecraft is constrained relative to the perifocal-and by extension the inertial frames-the UK formulation must be applied to two rigid bodies. These two rigid bodies are the virtual fully constrained and actual underconstrained spacecraft. This is an effective approach to mitigating the problems caused by dynamical constraint coupling.

Consider forming the constraints on these two rigid bodies. It is desired for the virtual spacecraft to travel in a prescribed orbit described in the $\mathcal{P}$ frame. In addition, it is desired for the relative motion of the actual spacecraft about its $\mathcal{B}_1$ axis with respect to the $\mathcal{L}_1$ frame to be left free; all other relative accelerations are zero. Choosing this constraint definition is convenient as the relative position is zero and the relative attitude will always be a first axis rotation. As such, the relative acceleration $\dot{\mathbf{V}}_{\mathcal{B}/\mathcal{L}}$ is defined using Equation (74).

$$\dot{\mathbf{V}}_{\mathcal{B}/\mathcal{L}} = \dot{\mathbf{V}}_{\mathcal{B}} + \mathrm{ad}_{\mathbf{V}_{\mathcal{B}/\mathcal{L}}} \mathrm{Ad}_{g_{\mathcal{B}/\mathcal{L}}^{-1}} \mathbf{V}_{\mathcal{L}} - \mathrm{Ad}_{g_{\mathcal{B}/\mathcal{L}}^{-1}} \dot{\mathbf{V}}_{\mathcal{L}}$$

Note that this approach works because the motion of the spacecraft in the $\mathcal{B}$ frame is free to rotate about the first axis of the $\mathcal{L}$ frame and has zero motion about the other $\mathcal{L}$ frame axes. Removing this condition may cause additional coupling which may require a different formulation. However, for most pointing purposes, releasing one degree of freedom is the most likely the case. Multiple unconstrained degrees of freedom would often signal larger

translational and rotational motions that are beyond the purview of this discussion. To simplify notation, the quantity S is defined as $S = [0_{5\times1} \quad I_5]$, and the two constraints are expressed in the form of Equations (63) and (64).

$$A = \begin{bmatrix} I_6 & 0_6 \\ -S\mathrm{Ad}_{g_{\mathcal{B}/\mathcal{L}}^{-1}} & S \end{bmatrix} \quad \mathbf{b} = \begin{bmatrix} \left(g_{\mathcal{L}}^{-1} g_d(\mathbf{V}_d^{\vee^2} + \dot{\mathbf{V}}_d^{\vee}) - \mathbf{V}_{\mathcal{L}}^{\vee^2}\right)^{\mid} \\ S\left(\dot{\mathbf{V}}_{\mathcal{B}/\mathcal{L}} - \mathrm{ad}_{\mathbf{V}_{\mathcal{B}/\mathcal{L}}} \mathrm{Ad}_{g_{\mathcal{B}/\mathcal{L}}^{-1}} \mathbf{V}_{\mathcal{L}}\right) \end{bmatrix}$$

$$\dot{\bar{V}} = \begin{bmatrix} \dot{\mathbf{V}}_{\mathcal{L}} \\ \dot{\mathbf{V}}_{\mathcal{B}} \end{bmatrix} \quad \bar{\mathbb{I}} = \begin{bmatrix} \mathbb{I}_{\mathcal{L}} & 0_{6\times6} \\ 0_{6\times6} & \mathbb{I}_{\mathcal{B}} \end{bmatrix}$$

4.2. Constrained Motion on Double Tangent Bundles

The preceding development illustrates how the GMUK can be applied to fully and underconstrained systems as the system parameters evolve as elements of $\mathbb{R}^6$. The geometric mechanics framework permits definition of accelerations both on $\mathbb{R}^6$ and on the double tangent bundle $\mathrm{T}^2\mathrm{SE}(3)$. By the definition of a manifold, the double tangent bundle of the base manifold is also a manifold. Taking the base manifold to be $\mathrm{SE}(3)$, elements of the double tangent bundle $\mathrm{T}^2\mathrm{SE}(3)$ are the set of all accelerations $\ddot{g}$. Constraints on the double tangent bundle adopt the form,

$$A\ddot{\tilde{g}}B = C, \tag{79}$$

where $\ddot{\tilde{g}} = \mathrm{blkdiag}\,(\ddot{g}_1, \ldots \ddot{g}_n)$ representing n rigid bodies. Furthermore, $A \in \mathbb{R}^{m\times4n}$, $B \in \mathbb{R}^{4n\times p}$, and $C \in \mathbb{R}^{m\times p}$. A matrix $\tilde{\mathbb{I}}$ can be defined.

$$\tilde{\mathbb{I}} = \mathrm{blkdiag}\,(J_1, m_1 \ldots J_n, m_n) \in \mathbb{R}^{4n\times4n},$$

and recalling $\ddot{g} = \ddot{g}_c + \ddot{g}_a$, the constraint equation can be rewritten following the process of (Udwadia & Kalaba, 2008).

$$A\tilde{\mathbb{I}}^{-\frac{1}{4}}\tilde{\mathbb{I}}^{\frac{1}{4}}\ddot{g}_c\tilde{\mathbb{I}}^{\frac{1}{4}}\tilde{\mathbb{I}}^{-\frac{1}{4}}B = C - A\ddot{\tilde{g}}_aB$$

The term $y = \tilde{\mathbb{I}}^{\frac{1}{4}} \ddot{g}_c \tilde{\mathbb{I}}^{\frac{1}{4}}$ can be defined such that $A\tilde{\mathbb{I}}^{-\frac{1}{4}} y \tilde{\mathbb{I}}^{-\frac{1}{4}} B = C - A\ddot{\tilde{g}}_a B$. Applying the property of the Moore-Penrose inverse yields,

$$A\tilde{\mathbb{I}}^{-\frac{1}{4}} \left(A\tilde{\mathbb{I}}^{-\frac{1}{4}}\right)^{+} \left(C - A\ddot{\tilde{g}}_a B\right) \left(\tilde{\mathbb{I}}^{-\frac{1}{4}} B\right)^{+} \tilde{\mathbb{I}}^{-\frac{1}{4}} B = C - A\ddot{\tilde{g}}_a B$$

By examination, it can also be seen that $y = \left(A\tilde{\mathbb{I}}^{-\frac{1}{4}}\right)^{+} \left(C - A\ddot{\tilde{g}}_a B\right) \left(\tilde{\mathbb{I}}^{-\frac{1}{4}} B\right)^{+}$. If the expressions for y are equated, $\ddot{g}_c$ can be obtained.

$$\ddot{g}_c = \tilde{\mathbb{I}}^{-\frac{1}{4}} \left(A\tilde{\mathbb{I}}^{-\frac{1}{4}}\right)^{+} \left(C - A\ddot{\tilde{g}}_a B\right) \left(\tilde{\mathbb{I}}^{-\frac{1}{4}} B\right)^{+} \tilde{\mathbb{I}}^{-\frac{1}{4}} \tag{80}$$

4.3. Numerical Simulations and Discussion

For the numerical simulations included here, the dynamic model for the forces and torque are given by Equations (23b) and (23a) respectively, assuming the gravitational field is uniform. In addition, the mass properties of the spacecraft in question are the same as those defined in Section 3.4. The initial conditions for the spacecraft for all fully and underconstrained cases are given as follows:

$$\mathbf{V} = \begin{bmatrix} 0 \\ 0 \\ 4.23818 \times 10^{-4} \\ 0 \\ -1.35622 \times 10^{3} \\ 0 \end{bmatrix} \qquad g = \begin{bmatrix} -1 & 0 & 0 & 3.20 \times 10^{6} \\ 0 & -0.81915 & -0.57358 & 0 \\ 0 & -0.57358 & 0.81915 & 0 \\ 0 & 0 & 0 & 1 \end{bmatrix}$$

4.3.1. Fully Constrained Results on Six-Dimensional Euclidean Space

First, consider a spacecraft that is fully constrained. The chosen desired orbits fall into two classes, each of which is discussed separately. The orbit can either be circular and non-inclined, or eccentric and inclined. Parabolic and hyperbolic orbits are not considered here; however, few-if any-changes are needed to apply this formulation to those cases.

4.3.1.1. Circular Non-Inclined Orbit

For the case where the reference orbit is fully constrained, circular, and non-inclined (FCCN), assuming the initial conditions satisfy the constraint, and taking the central body to have a uniform gravitational potential, intuition would suggest that there would be little to no control inputs necessary to satisfy the UK formulation. For the following results, a semi-major axis of 4000km and an eccentricity of zero were selected with all remaining orbital element equal to 0°. In addition, the results show the motion of the spacecraft over one orbital period. Applying Equations (69) and (71), initial conditions that satisfy the constraints can be specified. Once again, under no external perturbations for this type of orbit, the spacecraft is expected to have a bounded orbit and should require little to no control to maintain this motion.

Figure 4.2 illustrates the position of the spacecraft in the LCI frame. In the non-inclined, circular case, is is expected that the spacecraft should behave in a perfectly sinusoidal fashion in the $\mathcal{N}_1$ and $\mathcal{N}_2$ axes whereas there should be no motion in the $\mathcal{N}_3$ axes. Examination of Figure 4.2 confirms this behavior. As with the case of the position

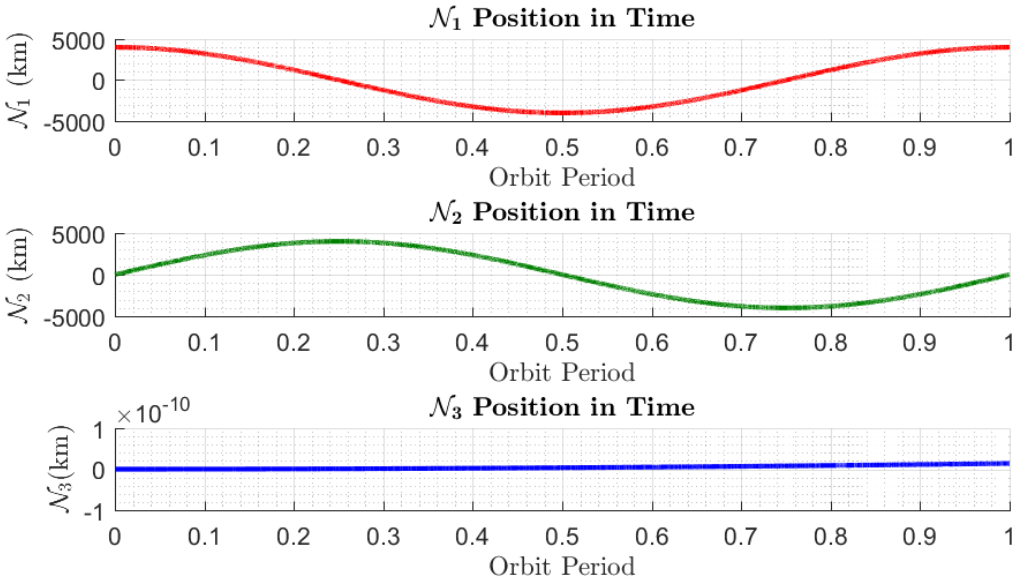

Figure 4.2 FCCN Position

components, the spacecraft velocities in the $\mathcal{N}_1$ and $\mathcal{N}_2$ axes are expected to oscillate in a sinusoidal fashion over one period of the orbit and there should be no velocity in the $\mathcal{N}_1$ axis. Such behavior is seen in Figure 4.3.

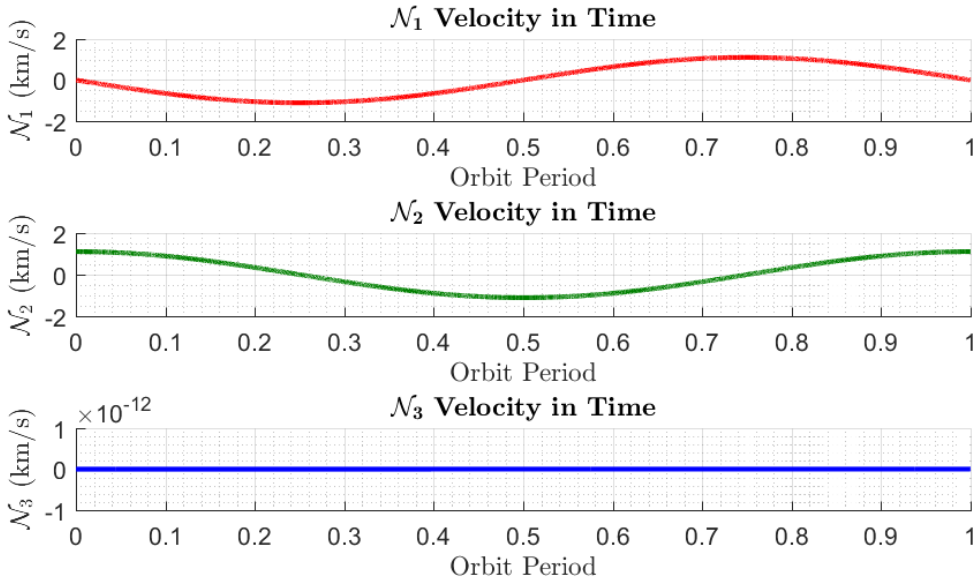

Figure 4.3 FCCN Velocity

If the spacecraft is constrained to point toward the body in a circular orbit, then the spacecraft should rotate about its $\mathcal{B}_3$ axis at the same rate as the mean motion of the spacecraft motion about the central body; this rate is identical to the rate of change of true anomaly for a circular orbit. This would suggest that only the yaw angle among the yaw-pitch-roll Euler angle set will change, and it will change linearly. Figure 4.4 displays the expected behavior. Recalling that the spacecraft should rotate about only its third axis with a constant angular velocity equal to the mean motion of the orbit, it is expected that the angular velocities about the remaining axes are zero. Figure 4.5 illustrates that the only nonzero angular velocity is that about $\mathcal{B}_3$ and is equal to the mean motion of the chosen orbit.

In the case of a uniform gravitational field acting on a point mass spacecraft, the required control inputs are expected to be exactly zero. However, treating the spacecraft as a rigid body, the dynamical model applied in these simulations given by Equation 25 accounts

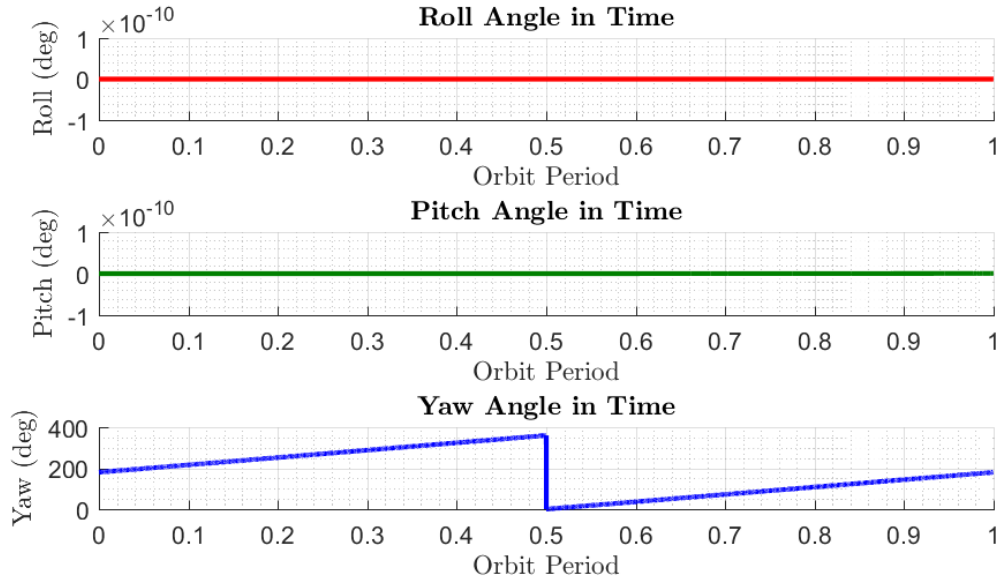

Figure 4.4 FCCN Euler Angles

for coupling between translational and rotational motion. As a result, the translational control inputs will be very small, but nonzero. This behavior is seen in Figure 4.6. In addition, these forces are functionally constant since the magnitude of this coupled force

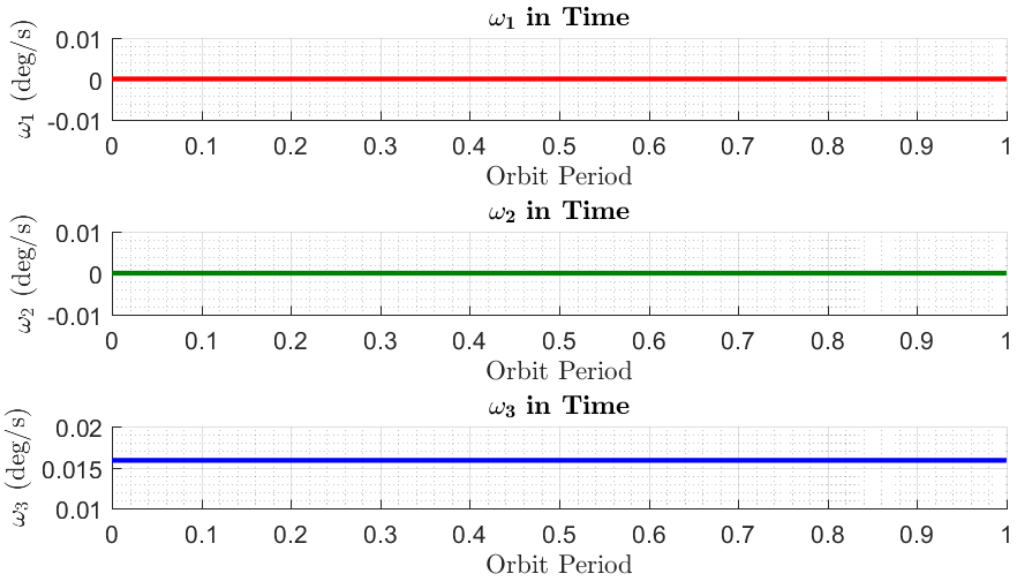

Figure 4.5 FCCN Body Rotation Rate

does not change in the case of the circular orbit and the spacecraft is rotating such that it is pointed toward the central body with the same orientation for the entire orbit.

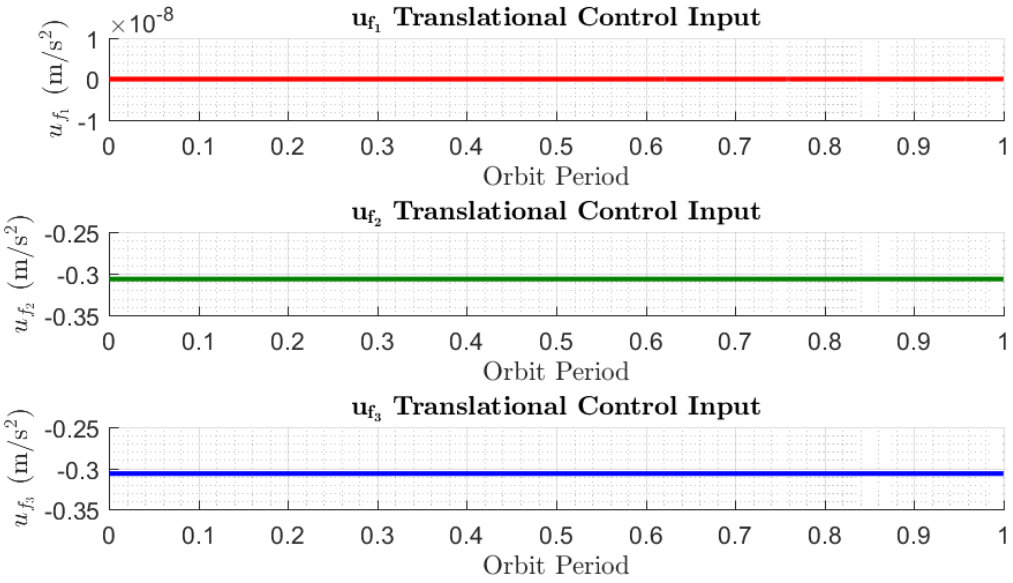

Figure 4.6 FCCN Translation Control

Similar to the translational control inputs, it is assumed that gravity gradient torque is also acting on the rigid body spacecraft. Hence, as seen in Figure 4.7, the rotational control inputs are small and nonzero. Furthermore, these control inputs are functionally constant because the circular orbit will not alter the magnitude of the gravity gradient torque.

4.3.1.2. Eccentric and Inclined Orbit

In the following numerical simulations, the rigid body spacecraft is considered in a lunar orbit with the following orbital elements:

$$a = 4000 \text{ km}, \quad e = 0.2, \quad i = 35^\circ, \quad \omega = 0^\circ, \quad \Omega = 0^\circ$$

It is noted that this fully constrained elliptical inclined (FCEI) case can be applied for any elliptical orbit. The desired position of the mass center of the spacecraft $\mathbf{r}_d$ and its desired attitude R_d are obtained through Equation (70) and the conversion of the rotation matrix R_d to the 3-2-1 Euler angle set is used to present the attitude results. The Euler angles are

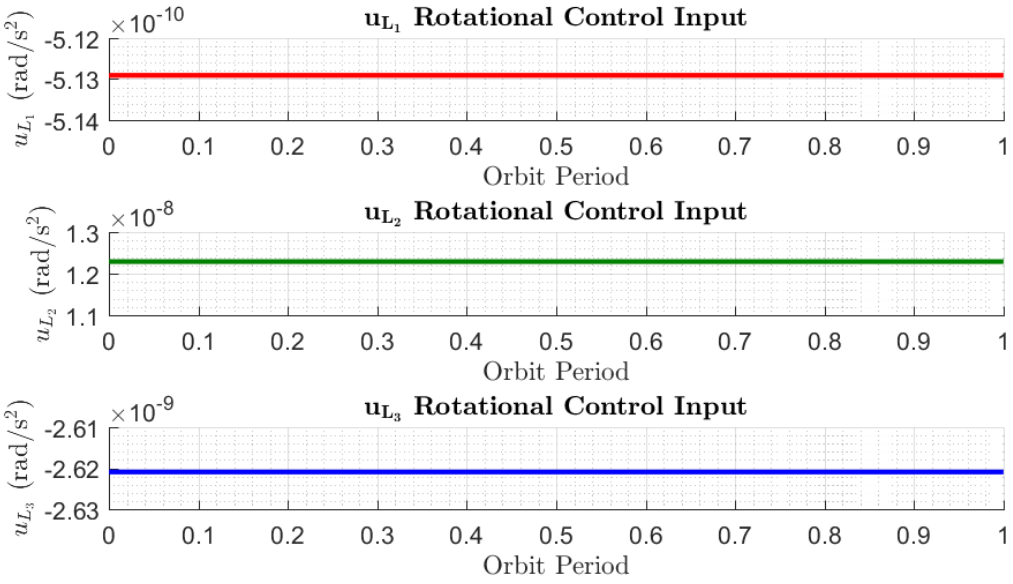

Figure 4.7 FCCN Rotational Control

determined from the direction cosine matrix R_d contained within g_d at each time step. Also, the angular $\boldsymbol{\omega}_d$ and translational $\mathbf{v}_d$ velocities are partitions of the augmented velocity $\mathbf{V}_d$ in Equation (73).

Figure 4.8 shows the selenocentric position of the spacecraft and its components in the inertial frame. With the inclined, eccentric orbit, it is expected for the system to still display periodicity with sinusoidal time histories. This agrees with the results shown in Figure 4.8. Figure 4.9 shows the velocity in the LCI frame. Like the position, the velocity displays the sinusoidal, periodic behavior expected from a bounded orbit of this type.

Figure 4.10 shows the Euler angle representation of the attitude of spacecraft relative to the LCI frame. The discontinuities, namely in the roll and yaw angles, are due to the bounding of these angles between 0° and 360°. Note that those angles do not vary linearly with time, indicating the fact that the desired orbit is inclined and eccentric.

The angular velocity of the spacecraft about the spacecraft $\mathcal{B}$ axes is shown in Figure 4.11. Recalling the nonlinear variation in the Euler angles, this behavior is once more verified by the fact that the angular velocity about the $\mathcal{B}_3$ axis (given by ω_3) is not constant

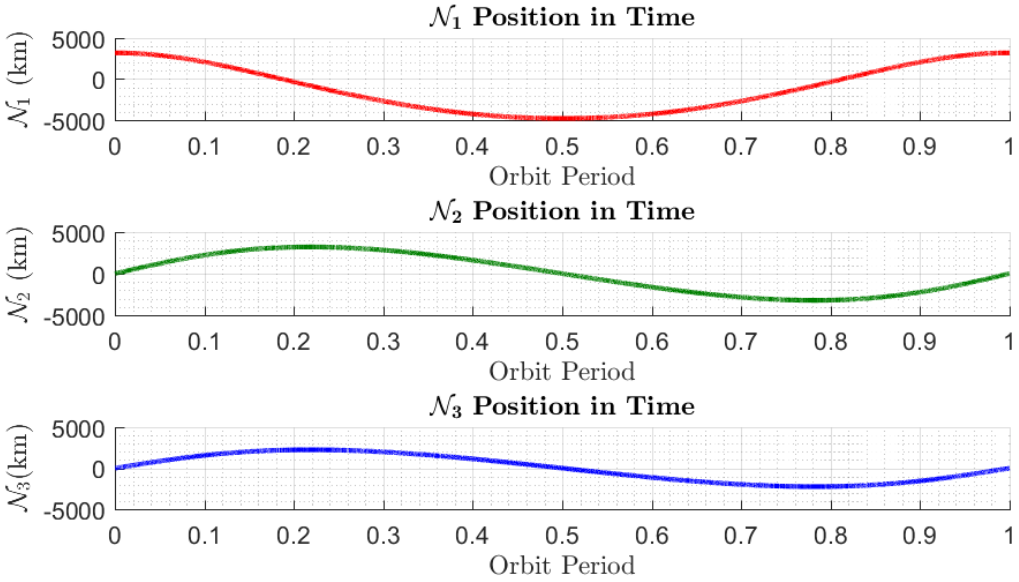

Figure 4.8 FCEI Position

and varies over the orbit, indicating the varying speed of the spacecraft over the eccentric orbit in accordance with Kepler's second law. Note that the angular velocities about the $\mathcal{B}_1$ and $\mathcal{B}_2$ are zero to within working numerical precision (nonzero angular velocities on the

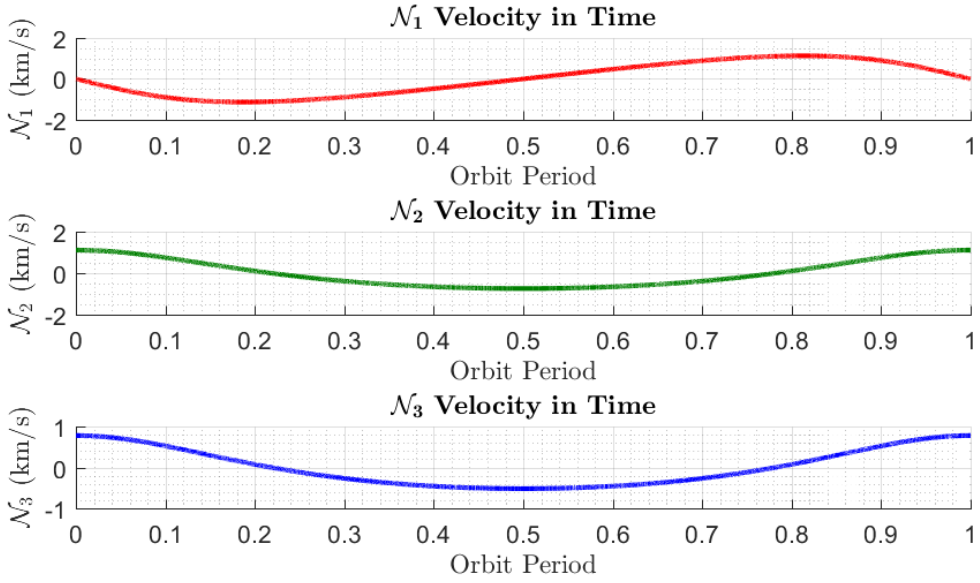

Figure 4.9 FCEI Velocity

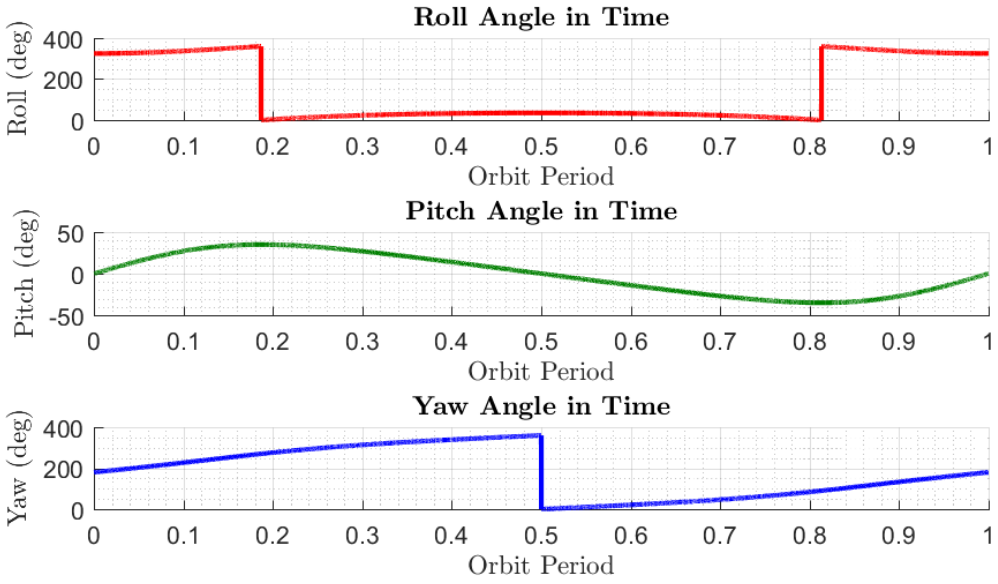

Figure 4.10 FCEI Euler Angles

order of 10^{-16} rad/s were observed). This is expected given that the initial conditions satisfy the constraint, meaning the only rotation needed to satisfy the attitude constraints are rotations about the $\mathcal{B}_3$ axis. The Euler angles illustrate the fact that there is some initial attitude that ensures the spacecraft is aligned with the selected modified LVLH frame. As the motion occurs in a plane, and the attitude is parallel to the plane, the rotation about the $\mathcal{B}_3$ axis will affect all three angles with respect to the LCI frame, but will only change one angle relative to the $\mathcal{P}$ perifocal frame, which is what is observed in the angular velocities.

The translational inputs for the spacecraft obtained from Equation (64) are seen in Figure 4.12 . The translational control inputs exhibit periodicity. These inputs will cancel out the coupled forces that act on the spacecraft. Note that the minimum control input magnitude occurs at half the orbital period. Alternatively, given that the initial conditions place the spacecraft at periselene, the minimum control acceleration magnitude occurs at aposelene. This makes sense because the perturbing term from the coupled dynamics varies as $||\mathbf{r}||^{-5}$.

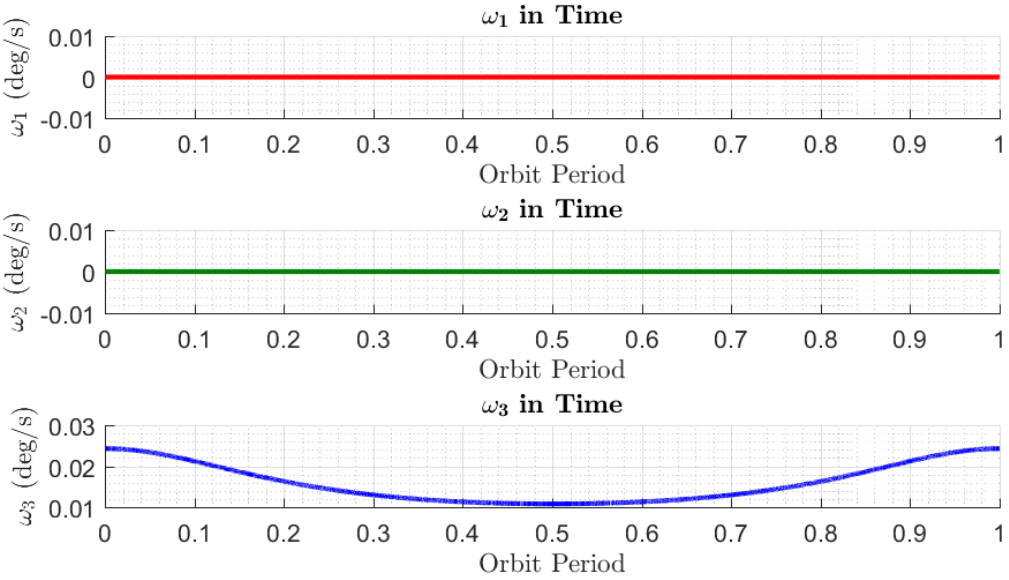

Figure 4.11 FCEI Angular Velocities

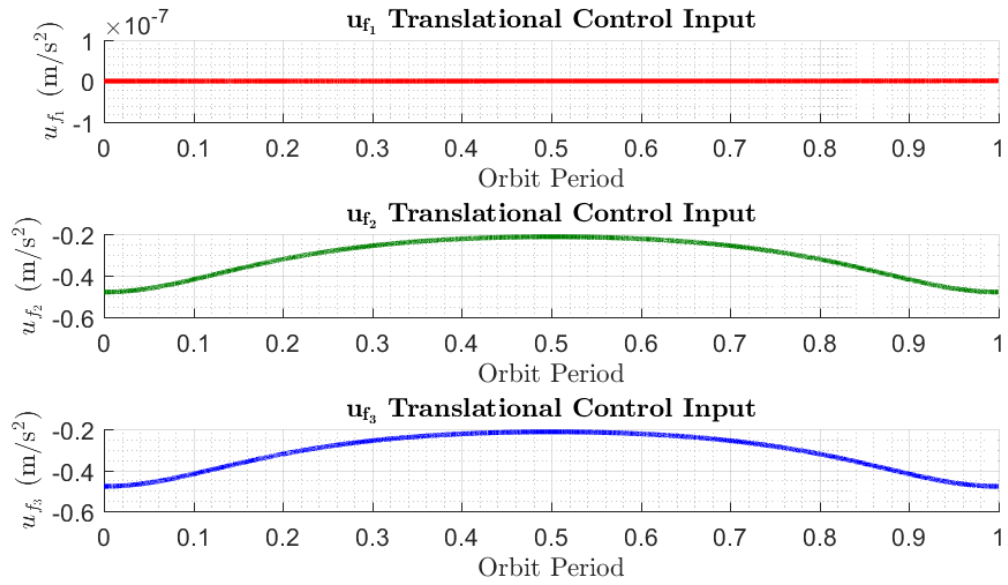

Figure 4.12 FCEI Translational Control Inputs

Finally, Figure 4.13 illustrates the rotational control inputs. As mentioned before, these are required to cancel out the gravity gradient torques. However, there is also an additional effect that is relevant to note; for the rotational control about the $\mathcal{B}_3$ axis, it is important to

show that the control input works to slow down the angular rotation in the first quarter of the orbit, and then varies almost linearly for the next half orbit, and then works to increase the rotation rate of the spacecraft. This is a result of Kepler's second law; that is, as the spacecraft leaves periselene, it moves slower and therefore must change its rotation rate to compensate for the change in velocity, thereby remaining pointed opposite its position vector. Furthermore, as the spacecraft leaves aposelene and approaches periselene, it must increase its angular rotation rate to compensate for the increase in its translational orbital velocity.

4.3.2. Fully Constrained Results on Double Tangent Bundles

Now, for the same scenario as that presented for treatment on $\mathbb{R}^6$, the same simulation can be prepared on the double tangent bundle to compare the equivalence of constraint acceleration determination on $\mathbb{R}^6$ and $T^2SE(3)$. It is expected that the fully constrained results on $\mathbb{R}^6$ should be identical to the fully constrained, elliptical, inclined formulation on the double tangent bundle manifold (FCEIM).

Figure 4.14 illustrates the difference between the treatment on $\mathbb{R}^6$ and $T^2SE(3)$. The difference in position is on the scale of millimeters between these approaches. This is a

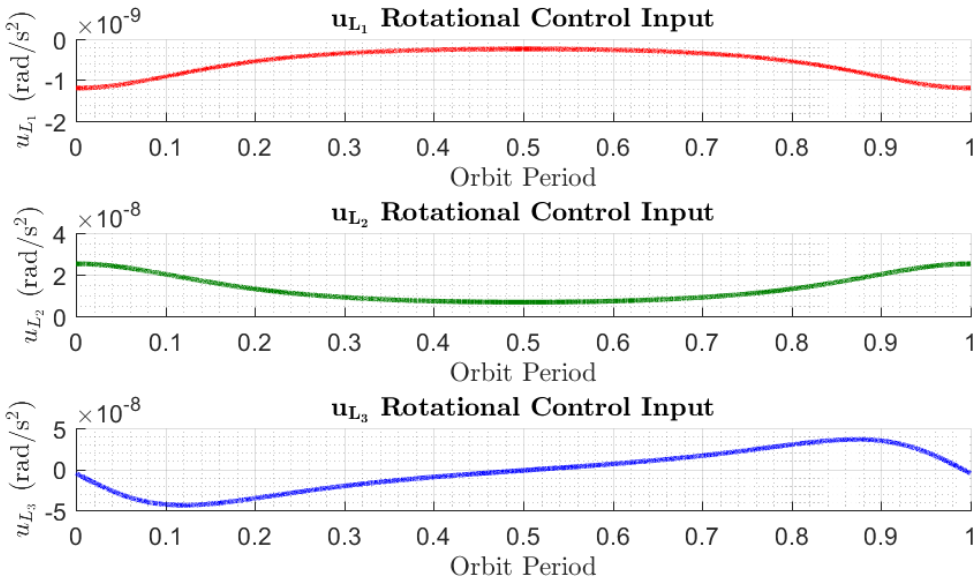

Figure 4.13 FCEI Rotational Control Inputs

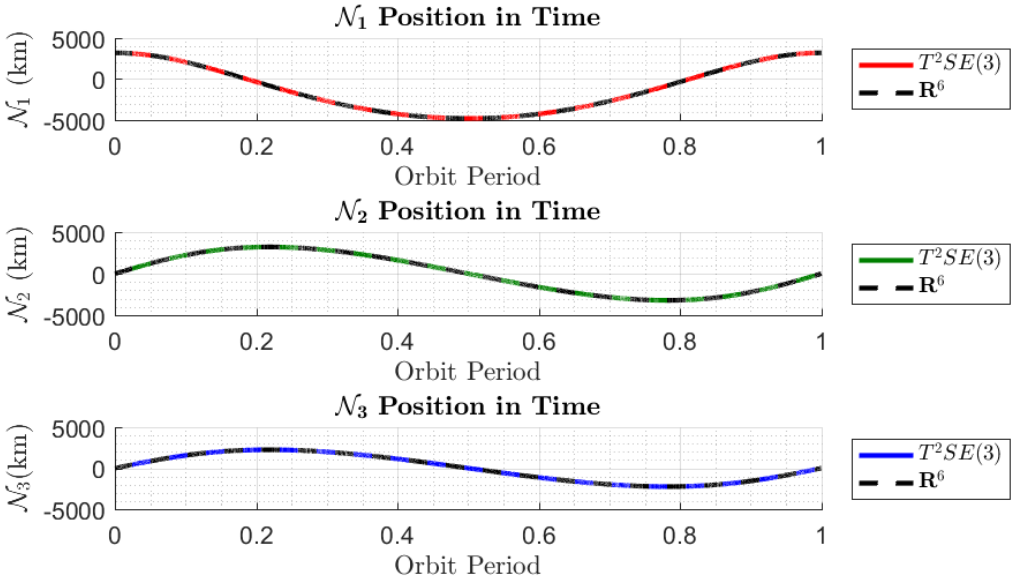

Figure 4.14 FCEIM Position

desirable result because it illustrates the equivalency between formulation on $\mathrm{T}^2\mathrm{SE}(3)$ and $\mathbb{R}^6$. A difference of only a few millimeters on the scale of thousands of kilometers for an orbit is negligible. The results on the Euclidean space are denoted by a black dashed line.

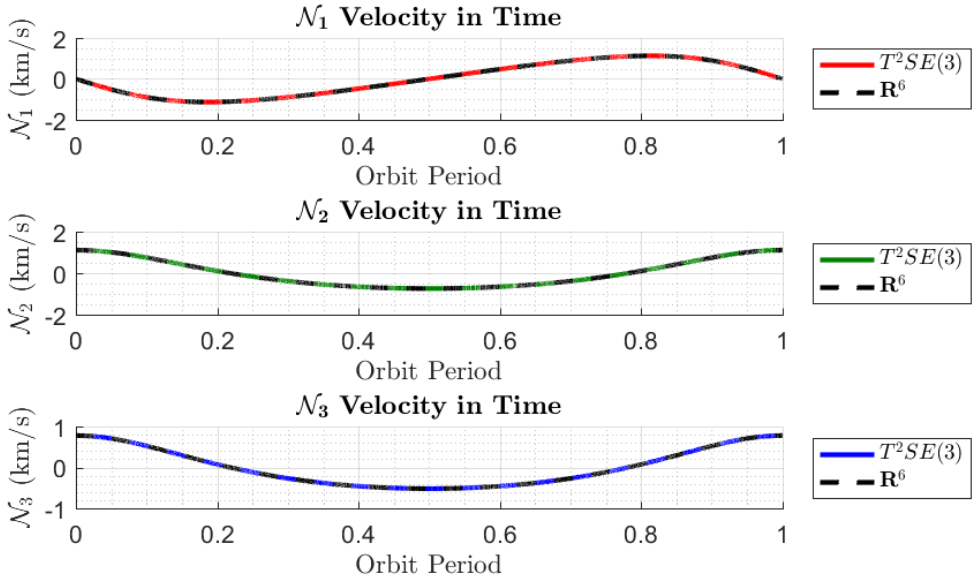

Figure 4.15 FCEIM Velocity

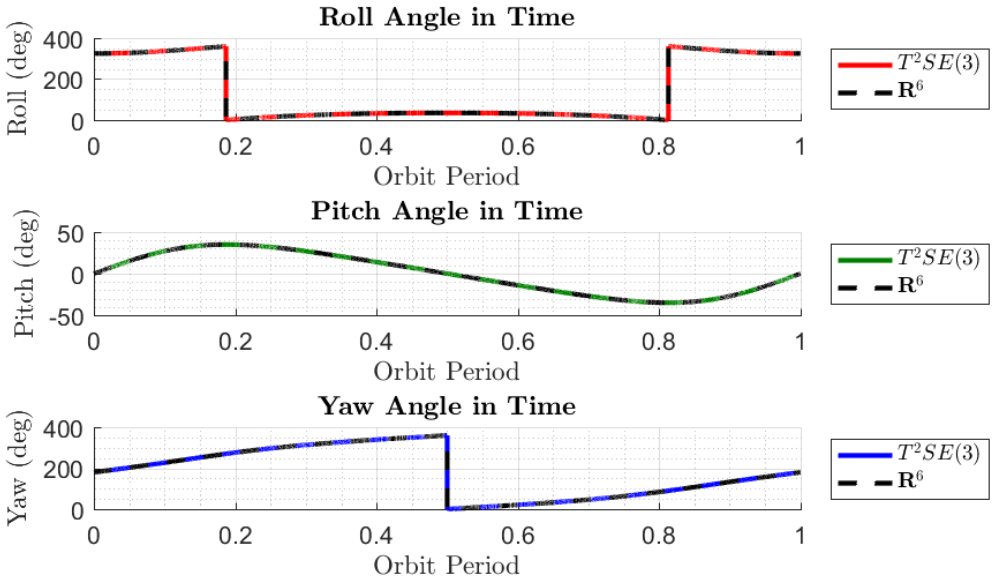

Figure 4.16 FCEIM Attitude

The difference between the velocities as seen in Figure 4.15 is small enough to be negligible. The difference in Euler angles is also irrelevant, which is illustrated in Figure 4.16.

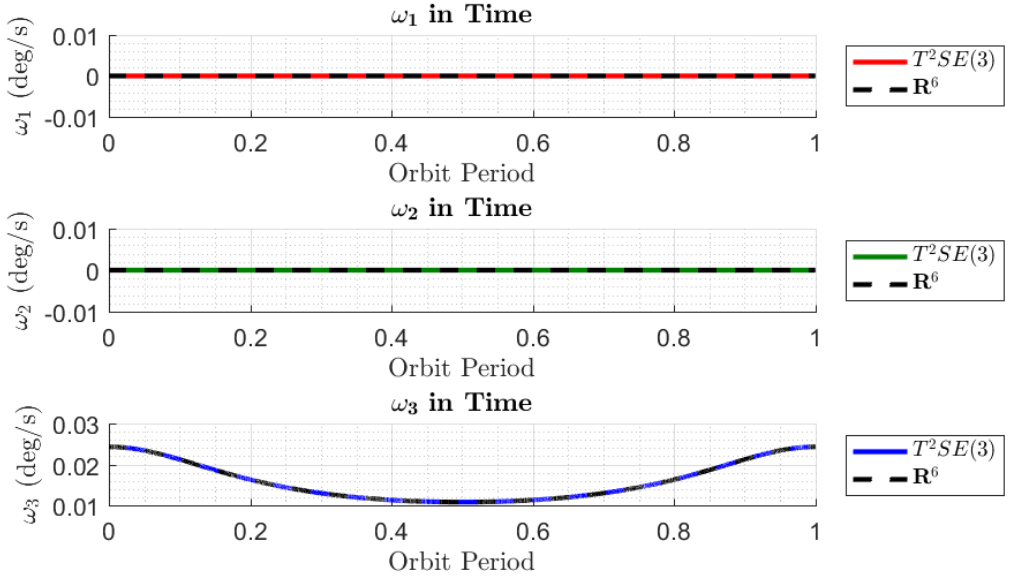

Figure 4.17 FCEIM Body Rotation Rate

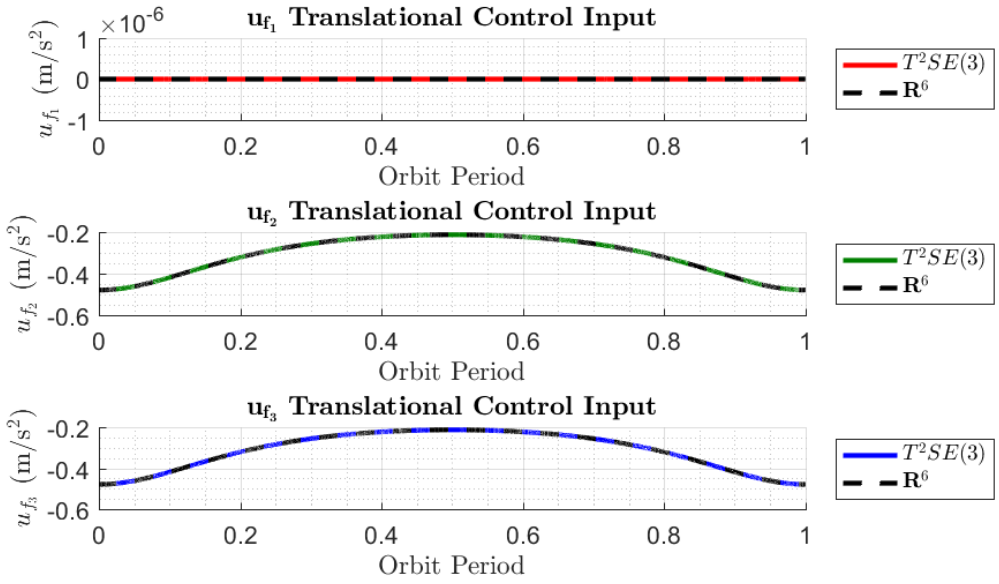

Figure 4.18 FCEIM Translational Control

The differences in angular velocities are seen in Figure 4.17. These responses are identical to within 10^{-16}deg/s. The differences in translational control inputs are once again negligibly small in Figure 4.18.

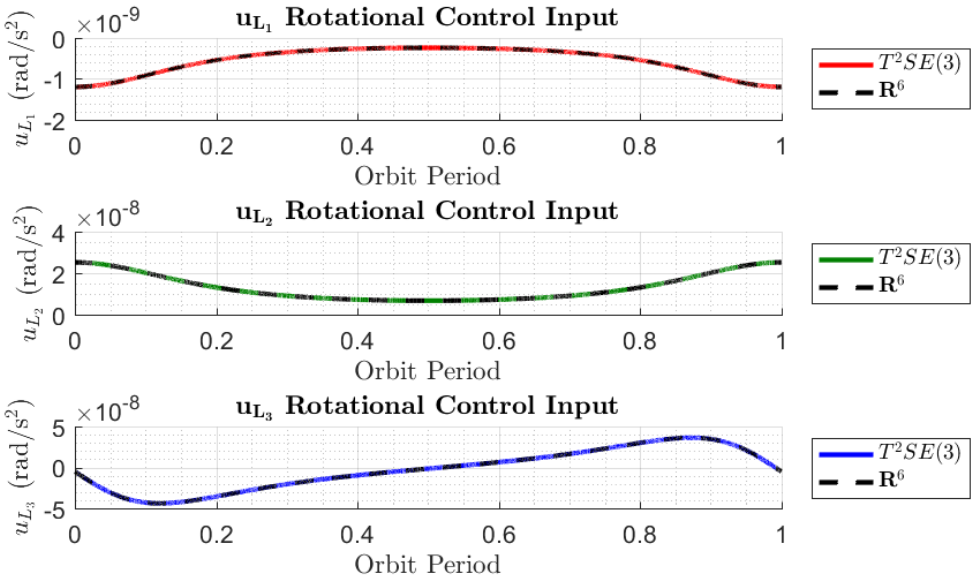

Figure 4.19 FCEIM Rotational Control

Finally, the rotational control inputs are functionally identical, per Figure 4.19.

In short, the treatment of fully constrained rigid bodies can be equivalently computed on $\mathbb{R}^6$ and $T^2SE(3)$. Treatment of underconstrained systems on $T^2SE(3)$ was not conducted, but the fundamental equation Equation(80) remains unchanged. Future work can examine the analysis of underconstrained systems on $T^2SE(3)$. In addition, the higher order terms presented in Section 3 can be incorporated into the dynamic model to increase the accuracy of the control acceleration determination.

4.3.3. Underconstrained Results on Six Dimensional Euclidean Space

The results for the underconstrained case are discussed below for a spacecraft that is assumed to rotate freely about its $\mathcal{B}_1$ axis. The motion is first propagated by assuming there are no torques acting on the spacecraft except for those from the gravity gradient. Since these deviations are small, the underconstrained case and the fully constrained case are plotted on the same figure to illustrate the comparison. The fully constrained case is denoted by a black solid line. The position and velocity of the spacecraft for the underconstrained case are given by Figures 4.20 and 4.21 respectively. This motion is not expected to change from the

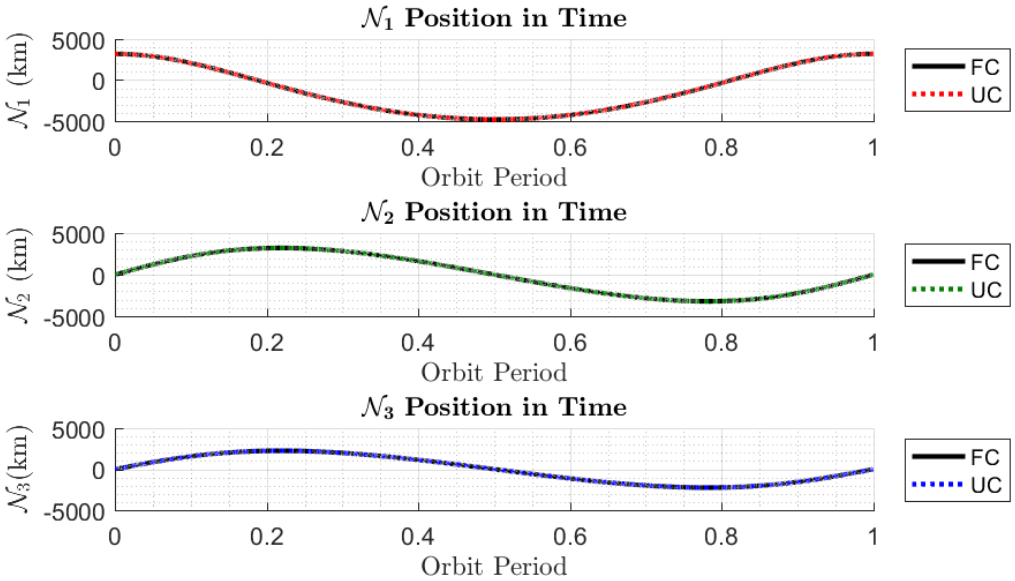

Figure 4.20 UCEI Position

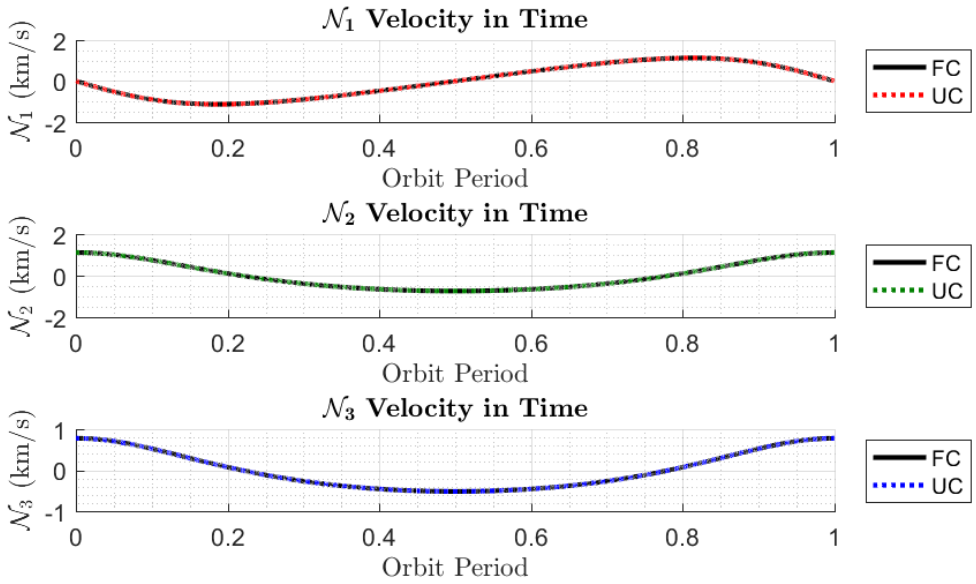

Figure 4.21 UCEI Velocity

fully constrained case as the translational components of the constraints are identical.

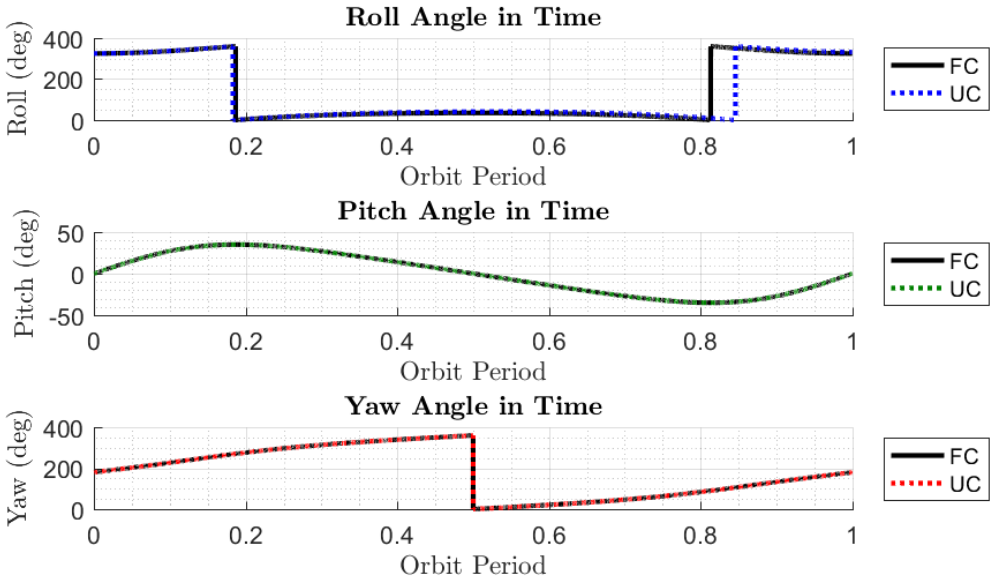

Figure 4.22 UCEI Euler Angles

Figure 4.22 illustrates the Euler angle attitude representation of the spacecraft with respect to time. Examining the roll angle, it can be seen that the deviation from this angle is very

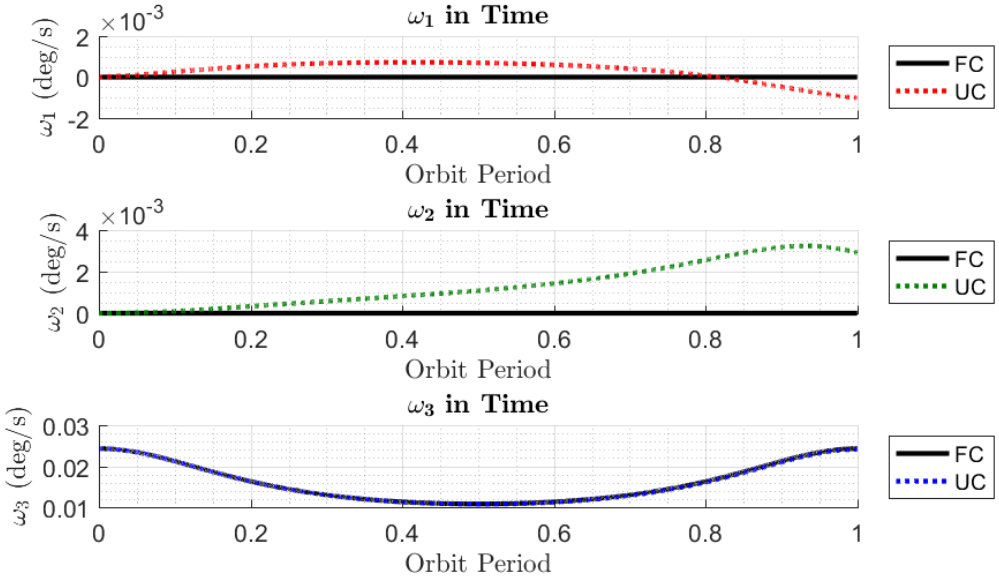

Figure 4.23 UCEI Angular Velocity

small. The discontinuity exaggerates the nature of these angles, but the gravity gradient perturbs the angle only slightly, while the other angles do not show any deviation. Small changes in angular velocity about the $\mathcal{B}_1$ axis are expected and observed in Figure 4.23.

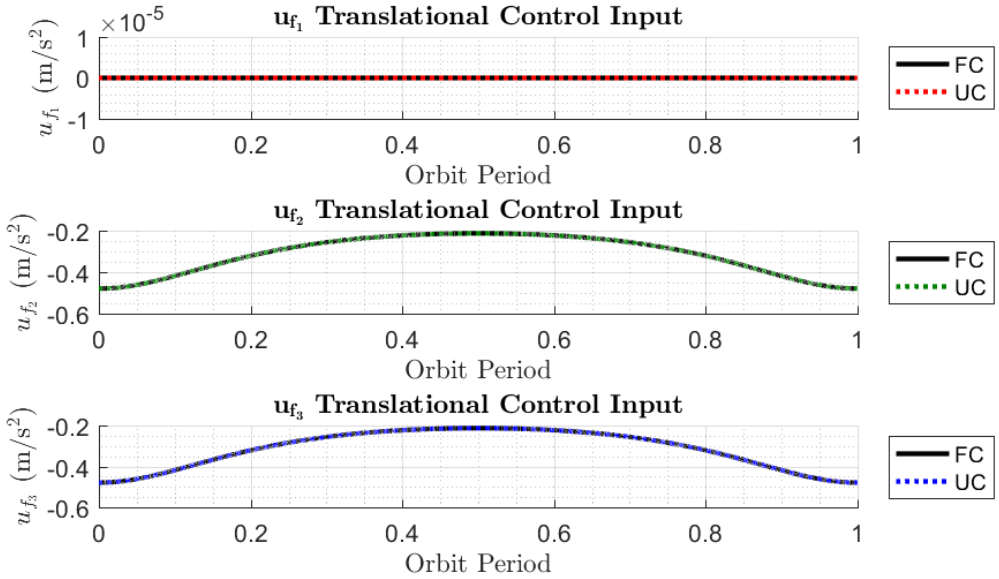

Figure 4.24 UCEI Translational Control

The translational control inputs are given by Figure 4.24. Note these controls are identical to fully constrained case's inputs, as expected since only the rotational motion was freed. Figure 4.25 illustrates the rotational control inputs. Note that the rotational control input about the $\mathcal{B}_1$ axis is non-zero. While the spacecraft is free to rotate around that axis, it must still satisfy the appropriate constraints between it and the virtual, fully constrained spacecraft. In fact, it requires more control input to free this axis when compared with the fully constrained case. As the spacecraft rotates, the gravitational gradient forces acting on it will change. As such, small angular changes and displacements may cause more exaggerated effects in the control inputs. And for control on the scale of 10^{-9}, such small changes are very pronounced. To get a better intuition for the effects of underconstraining the system, a larger, more noticeable torque is applied to the system.

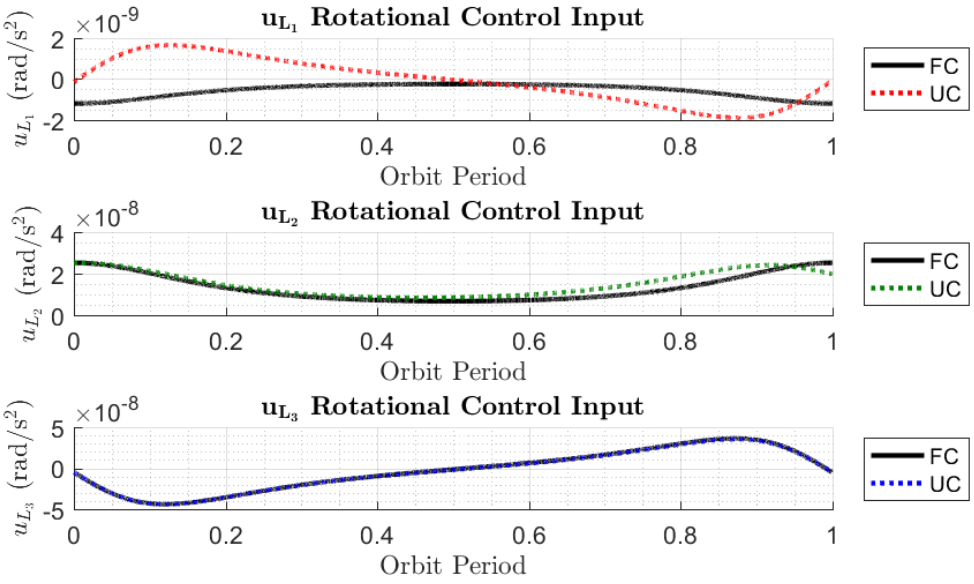

Figure 4.25 UCEI Rotational Control

4.3.3.1. Additional Sinusoidal Input

Now, a sinusoidal input torque of the form $\mathbf{L}_s = [0.005 \sin f, 0, 0]^T$ is included to exaggerate the effects of the UK underconstrained, elliptical, inclined orbit with the

sinusoidal input (UCEIS). These results are plotted as a comparison between the fully and underconstrained cases including the sinusoidal torque about the first axis $\mathcal{B}_1$.

The position and velocity in this underconstrained case are expected to be identical to those of the fully constrained case. Examination of Figure 4.26 shows the positions are the same in the under and fully constrained cases. Furthermore, Figure 4.27 shows that the inertial velocities are also the same.

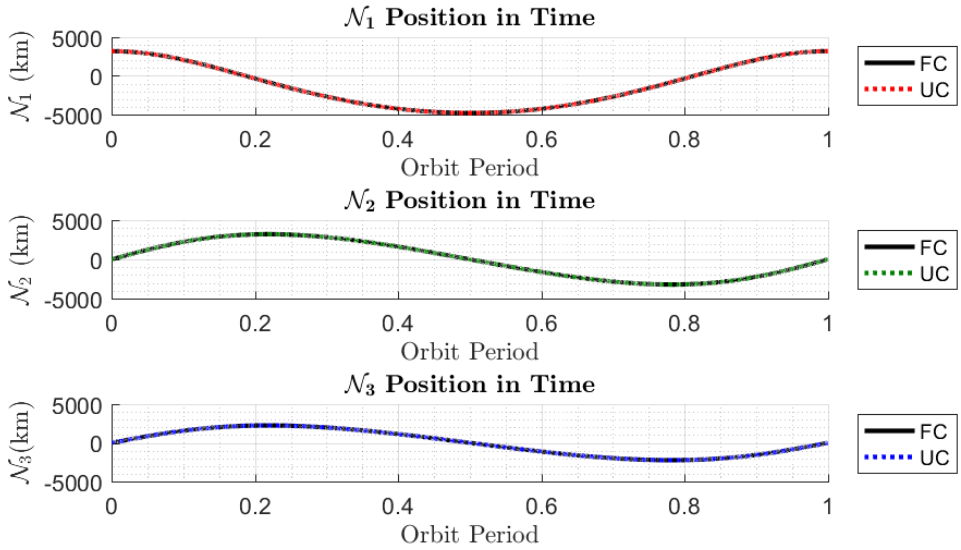

Figure 4.26 UCEIS Position

Figure 4.28 illustrates the Euler angles in the underconstrained case with the sinusoidal torque. Examining the roll angle, it is seen to vary over time, with the largest angular motion occurring between $f = 90°$ and $270°$. This appears due to the fact that the sinusoidal input is largest in this range, causing the motion to increase. It does not vary linearly, per the sinusoidal nature of the torque, especially between one-fourth and three-fourths of the orbital period. Similarly, the pitch and yaw angles change in time, but are identical to their counterparts in the fully constrained case.

The angular velocities in Figure 4.29 exhibit a periodic behavior, with the angular velocity about the $\mathcal{B}$ axis behaving as a sine function, which follows from the nature of the torque. Furthermore, examining the angular velocities about the $\mathcal{B}_2$ and $\mathcal{B}_3$ axes, note the

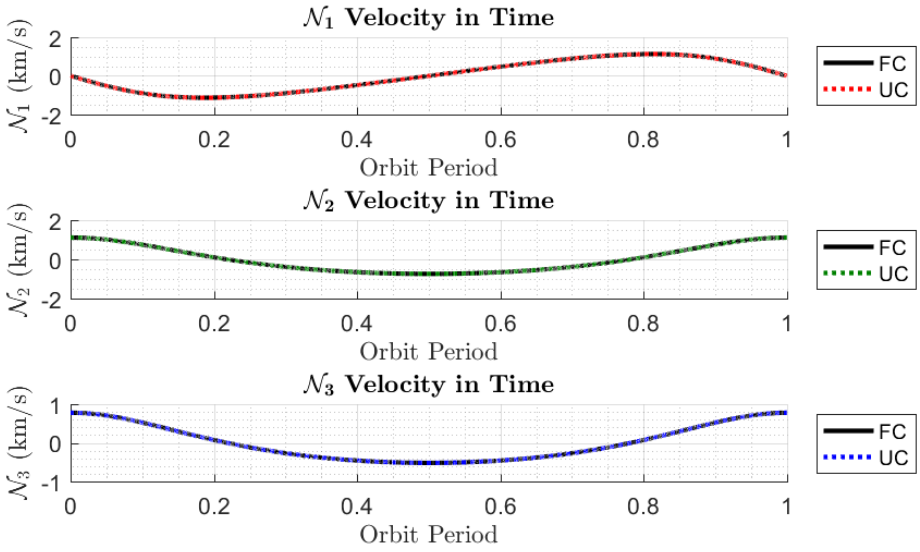

Figure 4.27 UCEIS Velocity

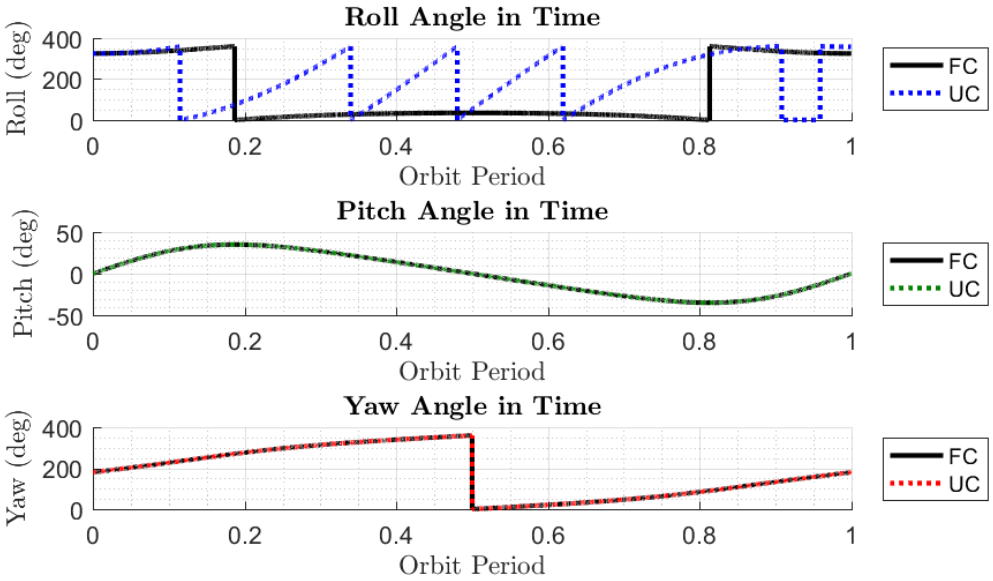

Figure 4.28 UCEIS Euler Angles

increase in frequency for the range of true anomalies $f \in [90°, 270°]$. This region occurs during the period where the torque changes from increasing to decreasing. As such, the torque is actively countering the motion of the spacecraft. As the $\mathcal{L}$ frame must rotate with the rate of change of true anomaly of the orbit, when the spacecraft is between $-90°$ and $90°$,

the torque is working with the motion of the spacecraft around the orbit. However, as the torque works opposite the motion of the orbit, more adjustments are needed to keep the $\mathcal{B}_1$ axis appropriately positioned when the angular velocities are higher. Also note that in this region of increased frequency the angular velocity ω_2 is phase shifted by one fourth the period of the increased range from ω_3. This intuitively makes sense as there are control torques about the $\mathcal{B}_2$ and $\mathcal{B}_3$ axes that are designed to keep the $\mathcal{B}_1$ axis pointed opposite its position vector. This is the constraint that is treated by the virtual spacecraft. The impressed torque is a sine function and the first axis rotation ensures that the other angular velocities must combine to satisfy the $\mathcal{B}_1$ pointing constraint.

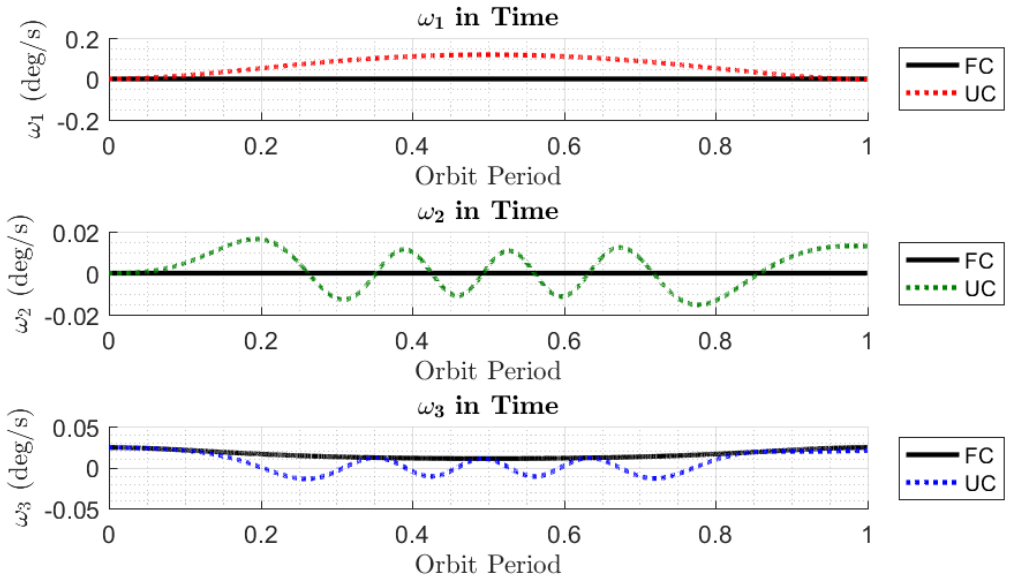

Figure 4.29 UCEIS Angular Velocity

The translational control inputs are nearly identical between the fully and underconstrained cases. As seen in Figure 4.30, the only acceleration that deviates from the fully constrained case are the translational control inputs from the spacecraft first body axis. However, the differences between these quantities are on the order of $10^{-7} m/s^2$.

The rotational control inputs are prime examples of the effects of freeing a degree of freedom. Note in Figure 4.31, the underconstrained control accelerations about the $\mathcal{B}_1$ axis

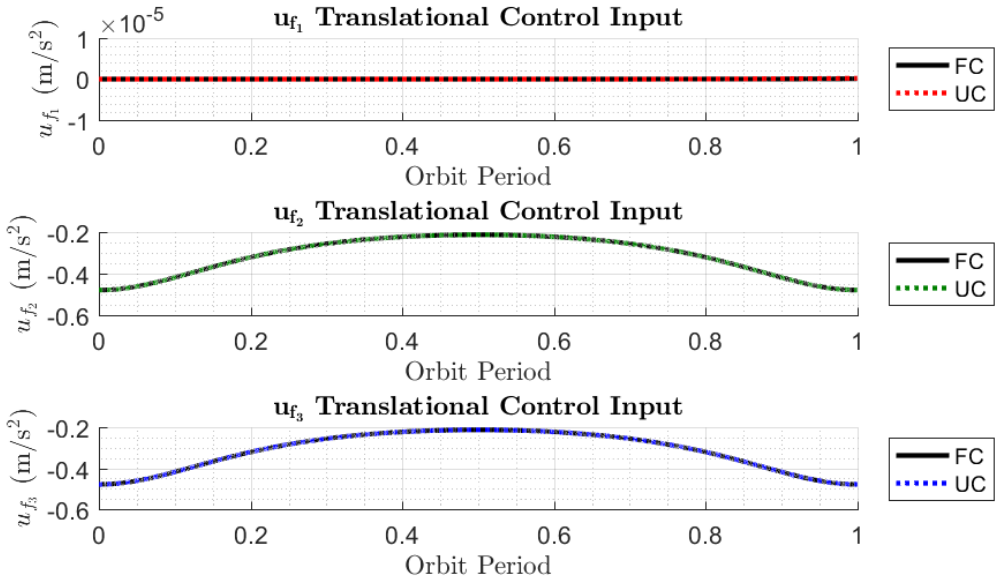

Figure 4.30 UCEIS Translational Control

is noticeably smaller than the fully constrained case. In fact, its deviations are small enough to be accounting for the gravity gradient torques acting on the system, similar to what was seen in Figure 4.25. However, it can be seen that the $\mathcal{B}_2$ and $\mathcal{B}_3$ underconstrained control

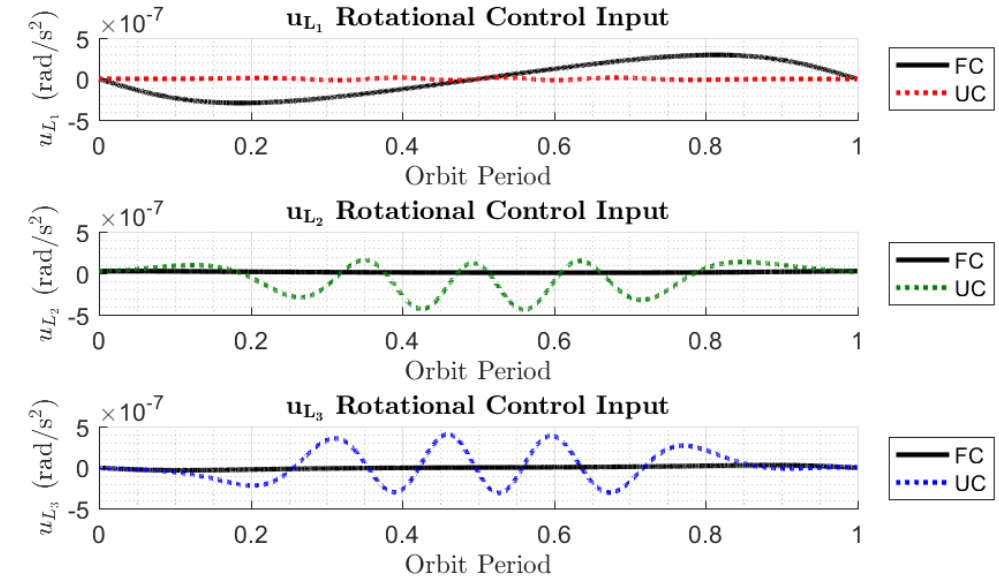

Figure 4.31 UCEIS Rotational Control

accelerations are larger than those from the fully constrained case. This is due to the fact that the spacecraft must keep its first axis pointed opposite the position vector. This means that relative to the perifocal frame, the spacecraft must still spin about the $\hat{P}_3$ axis. However, if the spacecraft has an angular displacement about the $\mathcal{B}_1$ axis, then the corresponding angular velocities about $\mathcal{B}_2$ and $\mathcal{B}_3$ must compensate to form the net rotation about the $\hat{P}_3$ axis and keep the first axis accurately pointed. This phenomenon is an example of constraint coupling and appears in the rotational control inputs.

5. Unmodeled Dynamics and Disturbances Within UK Formulation

Recall UK formulation requires that the initial conditions satisfy the constraints. Furthermore, the approach also specifies a set of modeled dynamics; it is from these modeled dynamics that the UK control accelerations are derived. If the initial conditions do not satisfy the constraints or there are unmodeled dynamics in the system, we require adjustments to the UK formulation. Two different cases that may disturb the system under the UK formulation are presented. Usage of a Morse-Lyapunov based controller using backstepping will display how these uncertainties can be handled in the system and UK formalism.

5.1. Disturbed Initial Conditions in UK Formulation

Here, the controller developed by Nazari et al. (2018) is utilized, but modified to capture error dynamics and provide tracking control. An integral term is also added to mitigate steady-state error in the response. The proposed controller is written here.

$$u = -\mathbb{I}K_1\dot{l} - \left(\mathrm{ad}^*_{\mathbf{V}}\mathbb{I}\mathbf{V} - \mathrm{ad}^*_{\mathbf{V}_n}\mathbb{I}\mathbf{V}_n\right) - \mathbb{I}K_2\psi - \mathbb{I}\kappa[0_{1\times 3}, E_{\mathbf{r}}^T E_R^T]^T - k_3\mathbb{I}\int_0^t \psi d\tau \tag{81}$$

The following definitions are necessary:

$$\psi = E_{\mathbf{V}} + K_1 l(E_g) \tag{82}$$

$$l(E_g) = [s^T(E_R), E_{\mathbf{r}}^T]^T \tag{83}$$

$$s(E_R) = \sum_{i=1}^{3} a_i \left(E_R^T \mathbf{e}_i\right)^{\times} \mathbf{e}_i \tag{84}$$

$$E_R = R_n^T R \quad E_{\mathbf{r}} = \mathbf{r} - \mathbf{r}_n \quad E_{\mathbf{V}} = \mathbf{V} - \mathbf{V}_n,$$

Here, the subscript "n" denotes nominal motion. In Equation (82),
$K_1 = \mathrm{blkdiag}(k_{11}I_3, k_{12}I_3) > 0$ with $k_{12} \neq 1$, $\mathbf{e}_i$ for $i = 1, 2, 3$ are the vectors that span the natural basis in $\mathbb{R}^3$, $A = \mathrm{diag}(a_1, a_2, a_3)$ with $a_1 > a_2 > a_3 \geq 1$, $K_2 = \mathrm{blkdiag}(k_{21}, k_{22})$ is

a positive definite matrix, and κ is a scalar value. Define a candidate Lyapunov function as,

$$V = V_1 + V_2(E_R) > 0, \quad \forall\ (E_g, E_{\mathbf{V}}) \neq (I, 0), \tag{85}$$

where V_1 is,

$$V_1 = \psi^T P \psi + \kappa\,(1 - k_{12})\,E_{\mathbf{r}}^T P_{22} E_{\mathbf{r}}, \tag{86a}$$

for $P = \text{blkdiag}(P_{11}, P_{22}) > 0$ and,

$$V_2(E_R) = k_3 \text{tr}(A - AE_R), \tag{86b}$$

with $k_3 > 0$. Note that if ψ goes to zero, it may not necessarily guarantee that the errors will go to zero. As such, some quadratic Lyapunov function of only the errors in $l(E_g)$ and $E_{\mathbf{V}}$ will only be positive semidefinite. To counteract this, the positive semidefinite Morse function V_2 is added to the positive definite quadratic function V_1 to form a total positive definite Lyapunov function V. The Morse function V_2 will vanish only when $E_R = I_3$. To prove stability, differentiate V.

Starting with V_1, note,

$$\dot{V}_1 = 2\left(\psi^T P \dot{\psi} + \kappa(1 - k_{12}) E_{\mathbf{r}}^T P_{22} \dot{E}_{\mathbf{r}}\right),$$

where,

$$\dot{\psi} = -K_2 \psi - \kappa [0_{1\times 3}, E_{\mathbf{r}}^T E_R^T]^T \tag{87}$$

Substituting Equation (87) into the equation for $\dot{V}_1$ yields the final form of this derivative.

$$\dot{V}_1 = 2\left(-\psi^T P K_2 \psi - \psi^T P \kappa [0_{1\times 3}, E_{\mathbf{r}}^T E_R^T]^T + \kappa(1 - k_{12}) E_{\mathbf{r}}^T P_{22} \dot{E}_{\mathbf{r}}\right)$$

By examining the second term T_2 in the expression for $\dot{V}_1$, the definitions for ψ and P can be expanded.

$$T_2 = \begin{bmatrix} E_\omega + k_{11} s(E_R) \\ E_{\mathbf{v}} + k_{12} E_{\mathbf{r}} \end{bmatrix}^T \begin{bmatrix} P_{11} & 0 \\ 0 & P_{22} \end{bmatrix} \kappa \begin{bmatrix} 0 \\ E_R E_{\mathbf{r}} \end{bmatrix}$$

The second term can be simplified.

$$T_2 = -\kappa E_{\mathbf{r}}^T \left(1 - k_{12}\right) P_{22} E_R E_{\mathbf{r}}$$

The third term T_3 can be simplified by finding the derivative for $\dot{E}_{\mathbf{r}} = E_R E_{\mathbf{v}}$. Furthermore using the backstepping technique employed by Nazari et al. (2018) and Khalil (2002), assume the system can be stabilized from a state feedback control law of the following form:

$$E_{\mathbf{V}} = -l(E_g) \tag{88}$$

Expanding Equation (88) it can be shown that that $E_{\mathbf{v}} = -E_{\mathbf{r}}$; hence, the third term can be rewritten.

$$T_3 = -\kappa(1 - k_{12}) E_{\mathbf{r}}^T P_{22} E_R E_{\mathbf{r}}$$

Substituting T_2 and T_3 into the expression for $\dot{V}_1$, these terms cancel and the total derivative $\dot{V}_1$ is obtained.

$$\dot{V}_1 = -2\psi^T P K_2 \psi < 0 \qquad \forall (E_g, E_{\mathbf{V}}) \neq (I, 0)$$

To find dV_2, differentiate Equation (86b).

$$dV_2 = -k_3 \mathrm{tr}(A E_r E_\omega^\times) dt$$

From the backstepping technique, $E_\omega = -s(E_R)$; as such, dV_2 can be simplified.

$$dV_2 = k_3 \mathrm{tr}(A E_r s(E_R)^\times) dt$$

It was shown by Nazari et al. (2018) that:

$$\mathrm{tr}(A E_r s(E_R)^\times) = -s^T(E_R) s(E_R)$$

The final expression for $\dot{V}_2$ can be obtained with this simplification.

$$\dot{V}_2 = -k_3 s^T(E_R) s(E_R) \leq 0 \qquad \forall (E_g, E_{\mathbf{V}}) \neq (I, 0),$$

is negative semidefinite, vanishing at $E_R = I_3$ as well as the cases $E_R = \text{diag}(1, -1, -1)$, $\text{diag}(-1, 1, -1)$, and $\text{diag}(-1, -1, 1)$. As noted by Nazari et al. (2018), these are saddle equilibria, and these critical points are isolated where the stable manifolds of these equilibria have zero measure in TSE(3). For the total derivative of the Lyapunov function,

$$\dot{V} = -k_3 s^T(E_R) s(E_R) - 2\psi^T P K_2 \psi, \tag{89}$$

the equilibrium state $(E_g^*, E_{\mathbf{V}}^*) = (I, 0)$ is almost globally asymptotically stable. This means that, when this controller is applied in addition to the UK formulation, it will drive the fully constrained closed loop (FCCL) system with disturbed states to the constrained desired state. Presented here are some transient response results using the controller within the context of UK formulation with disturbed initial conditions. The gains are chosen as follows:

$$k_{11} = 0.099999 \quad k_{12} = 0.99999$$

$$k_{21} = 1.1 \quad k_{22} = \text{diag}(0.05, 0.05, 1) \times 10^{-5}$$

$$\kappa = 0.0002 \quad A = \text{diag}(3, 2, 1) \quad k_3 = 1000$$

The disturbed initial conditions are given as follows:

$$\mathbf{V} = \begin{bmatrix} 0.05000 \\ 0.07000 \\ 0.01044 \\ -5.69501 \times 10^2 \\ -1.17817 \times 10^3 \\ 328.89840 \end{bmatrix} \qquad g = \begin{bmatrix} -0.88728 & 0.35421 & -0.29541 & 3.201 \times 10^6 \\ -0.25042 & -0.90782 & -0.33637 & 163.150 \\ -0.38733 & -0.22448 & 0.89420 & 4997.447 \\ 0 & 0 & 0 & 1 \end{bmatrix}$$

Figure 5.1 shows the transient response of the position. The dashed black line illustrates the trajectory and time history of the states with initial conditions that satisfy the constraints. Note that the color lines converge to the dashed line, indicating that the Morse-Lyapunov

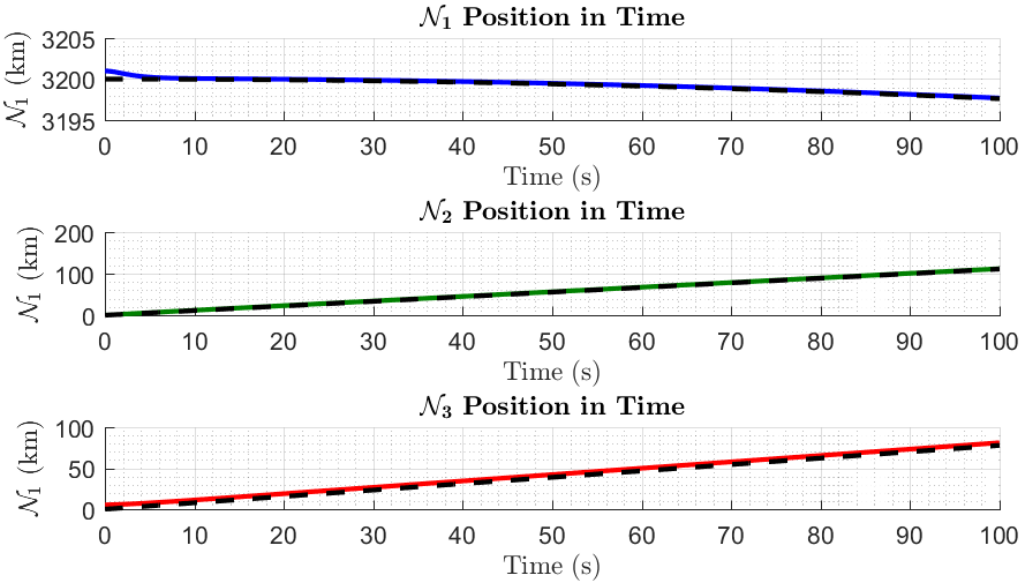

Figure 5.1 FCCL Position

based controller drives the system to the desired trajectory. Note that the period of the spacecraft's orbit is on the scale of 22,000 seconds, so these results illustrate a small fraction of the total orbit. Figure 5.2. The velocity is seen to overshoot the correct trajectory slightly

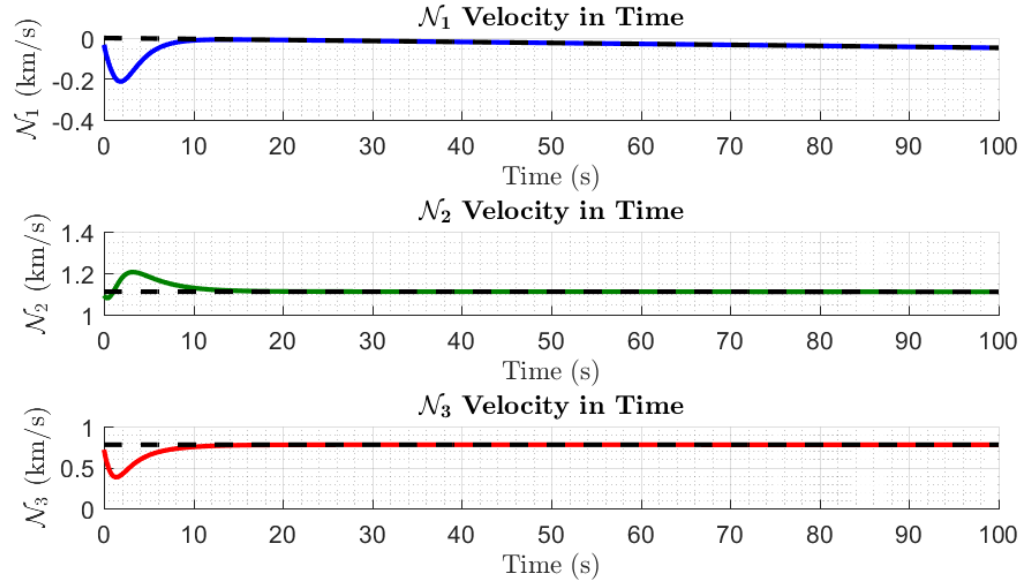

Figure 5.2 FCCL Velocity

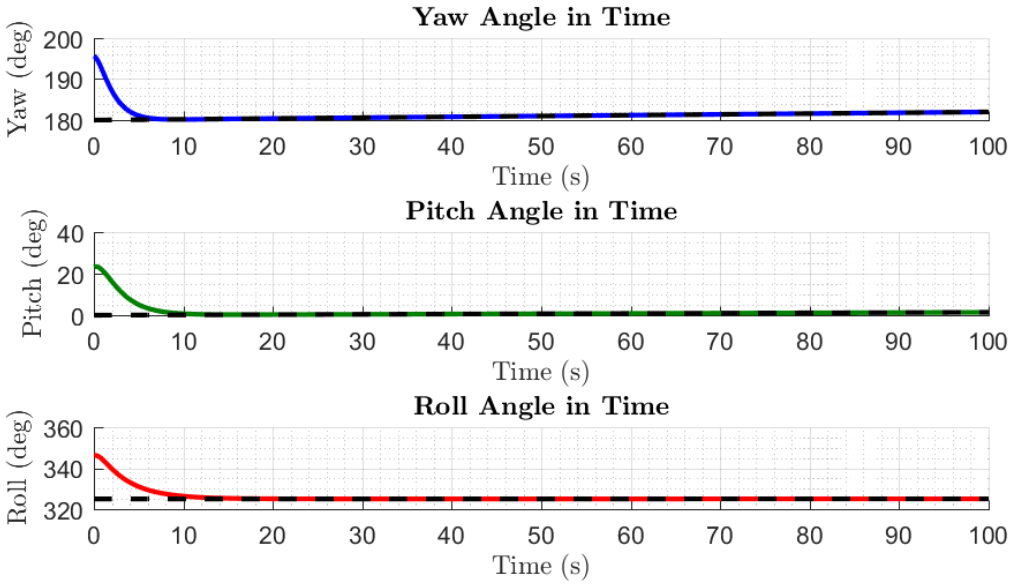

Figure 5.3 FCCL Attitude

at the beginning of the timespan, but also eventually converges to the nominal case. All the angular quantities converge in a robust manner with respect to the gains. The values of these gains can be altered somewhat drastically and will still converge. The angular velocities

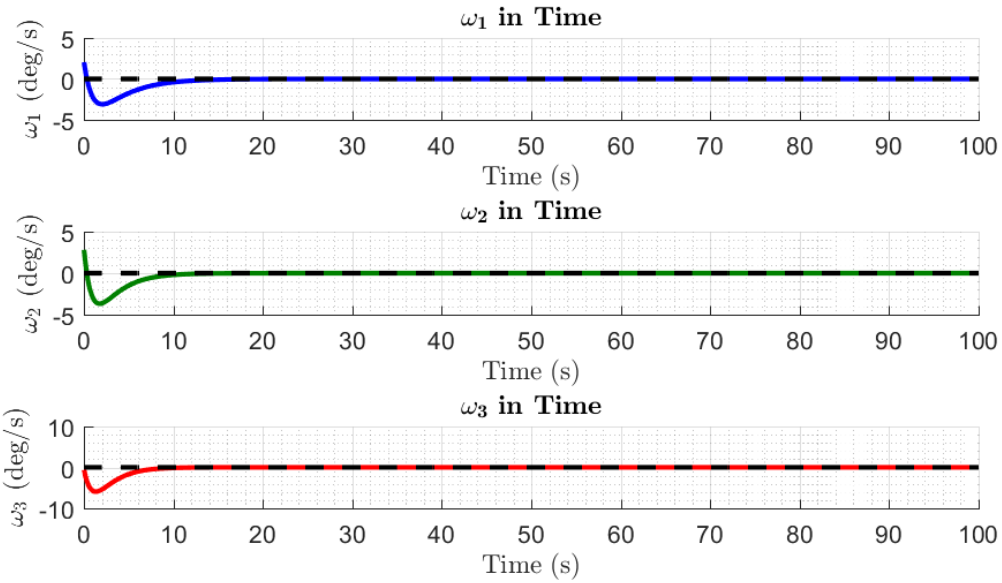

Figure 5.4 FCCL Angular Velocity

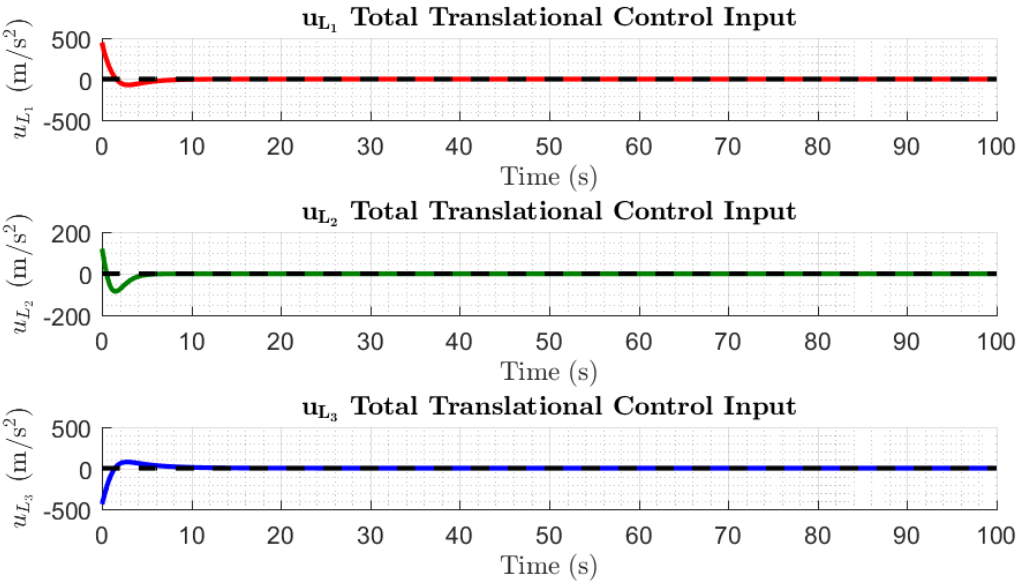

Figure 5.5 FCCL Translational Control

converge to the original fully constrained response in Figure 5.4. Figure 5.5 illustrates the control inputs using the controller. They eventually converge to the nominal case control as the Morse-Lyapunov controller approaches zero. The rotational control inputs in Figure 5.6

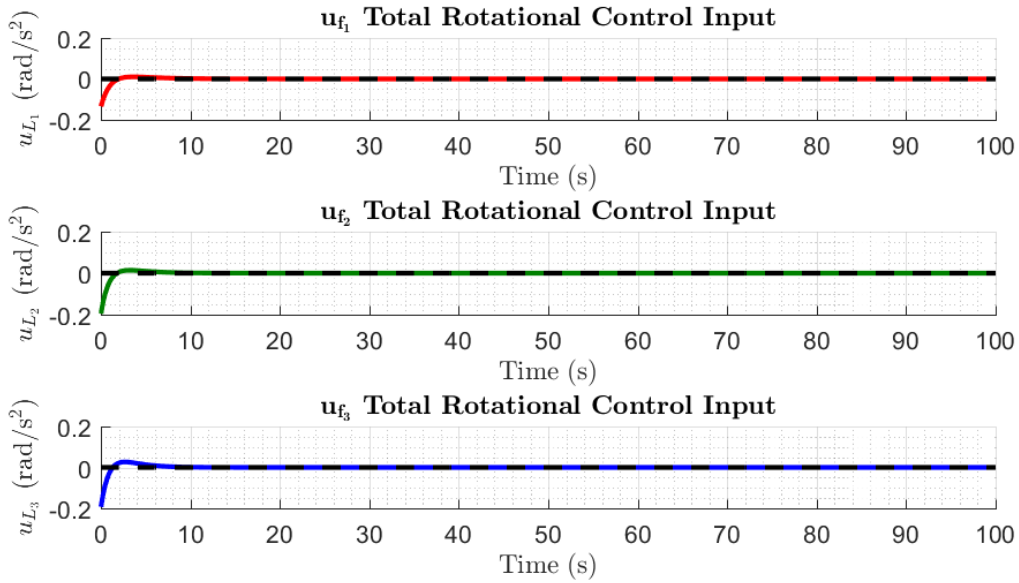

Figure 5.6 FCCL Rotational Control

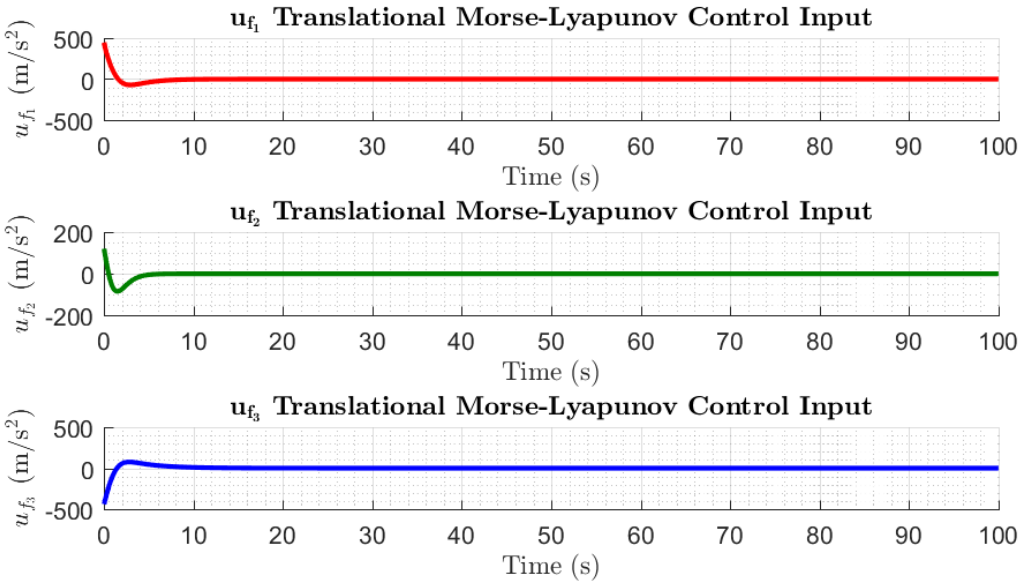

Figure 5.7 FCCL Translational Morse-Lyapunov Control

are seen to converge to the original case denoted by the dashed line. Given that the Morse-Lyapunov based controller using backstepping was applied to the system in addition to the UK control acceleration, this control input can be analyzed on its own to see how it contributes to the overall dynamics and control. From Figures 5.7 and 5.8, it can be seen that the Morse-Lyapunov based control inputs approach zero. This follows from the fact that the M-L controller is a tracking controller that will go to zero as the constraint is satisfied.

Analysis of the steady state can illustrate how close to the desired configuration the Morse-Lyapunov based controller can drive the rigid body, per Figures 5.9 and 5.10. It can be seen that the total rotational control inputs are extremely close to the nominal UK inputs, indicating the M-L controller has worked properly. For the translational control inputs, there are some larger errors. Preliminary investigation of these errors prompted the inclusion of the integral term which improved the response to the included results. Further tuning of the gains could lead to better response characteristics and less steady state error.

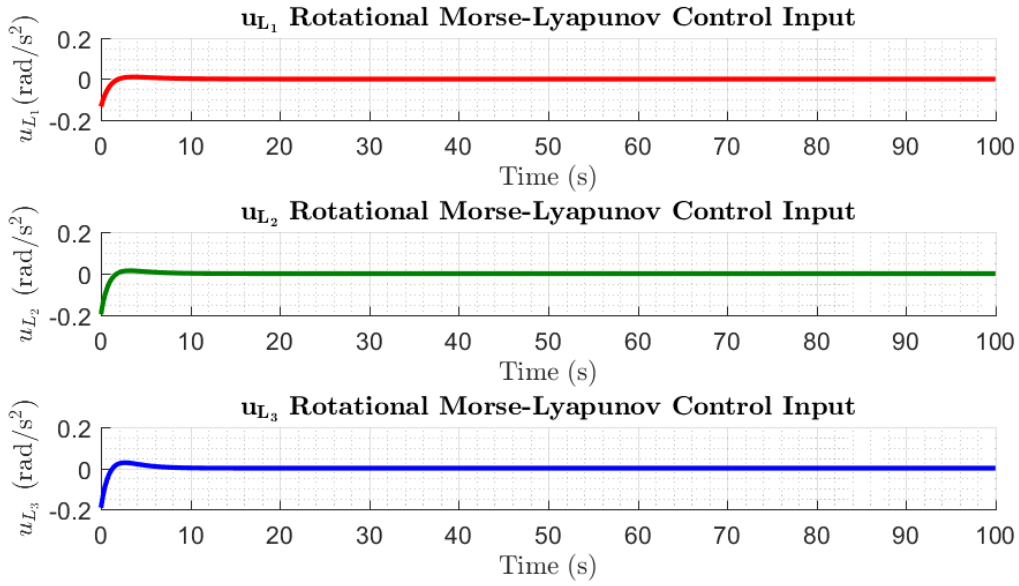

Figure 5.8 FCCL Rotational Morse-Lyapunov Control

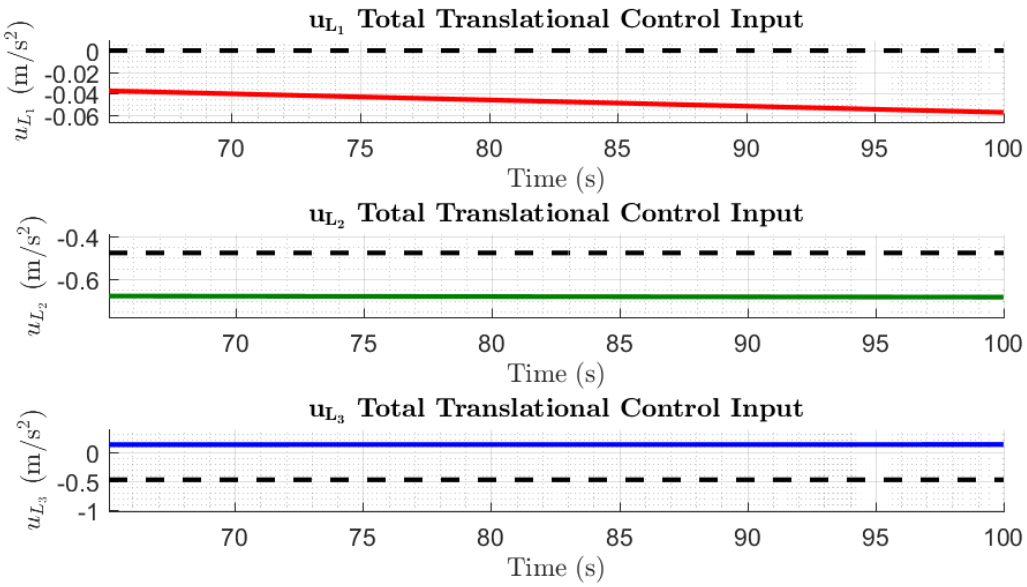

Figure 5.9 FCCL Translational Control Error

5.2. Robust Control with Unmodeled Dynamics

Now, consider the case where there are unmodeled dynamics acting on the system. The UK formulation finds the constraint acceleration under the modeled dynamics; however, if

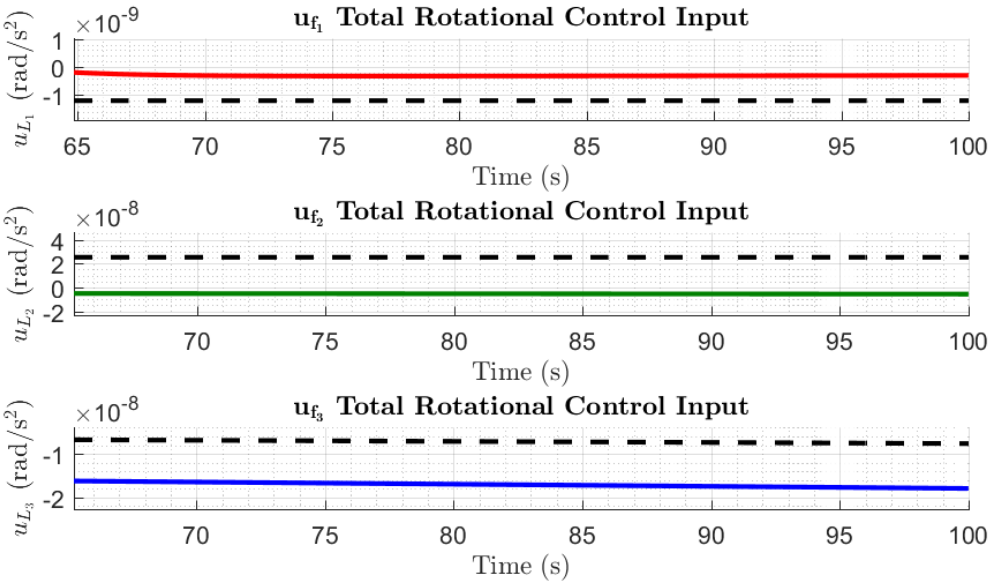

Figure 5.10 FCCL Rotational Control Error

there are other unmodeled dynamics, they will still affect the states of the system. As such, the UK formulation may violate the constraints if these unmodeled disturbances are substantial enough. To counter this problem, an extension of the Morse-Lyapunov based controller in Equation (81) is proposed that will manage these constraints. Assume the dynamics of the system are modeled as in Equations (23b) and (23a), but the spacecraft is affected by higher order gravitational terms. Examination of Equation (42) shows that the maximum quantity of the higher order gravitational terms is some constant times $||\mathbf{r}||^{-4}$ for spacecraft of degree and order two. A known upper bound that varies with $\mathbf{r}$ can be specified such that this controller will capture external perturbations from the higher order terms.

$$u = -\mathbb{I}K_1\dot{l} - \left(\mathrm{ad}^*_{\mathbf{V}}\mathbb{I}\mathbf{V} - \mathrm{ad}^*_{\mathbf{V}_n}\mathbb{I}\mathbf{V}_n\right) - \mathbb{I}K_2\psi - \mathbb{I}\kappa[0_{1\times 3}, E^T_{\mathbf{r}}E^T_R]^T - k_3\mathbb{I}\int_0^t \psi d\tau - \frac{\kappa_2\mathbb{I}}{||\mathbf{r}||^4}O \quad (90)$$

Here O is a six by one vector of ones. To analyze the performance of this controller, all the gains are chosen as in Section 5.1, and $\kappa_2 = -39/2$. This is a very conservative estimate based on the values of the second order gravitational constants (Misra et al., 2016).

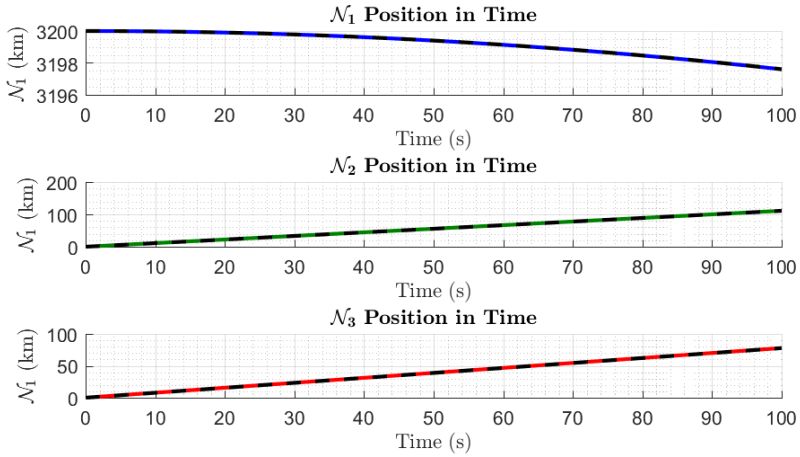

Figure 5.11 Position Under Unmodeled Dynamics

Figure 5.11 shows that the position difference between the unperturbed and the perturbed orbits is approximately one meter in the largest axis. In all results, the black, dashed line represents the results with no unmodeled dynamics and the colored lines indicate the response under the unmodeled dynamics. The difference in the velocities is almost negligibly small, on the scale of millimeters per second.

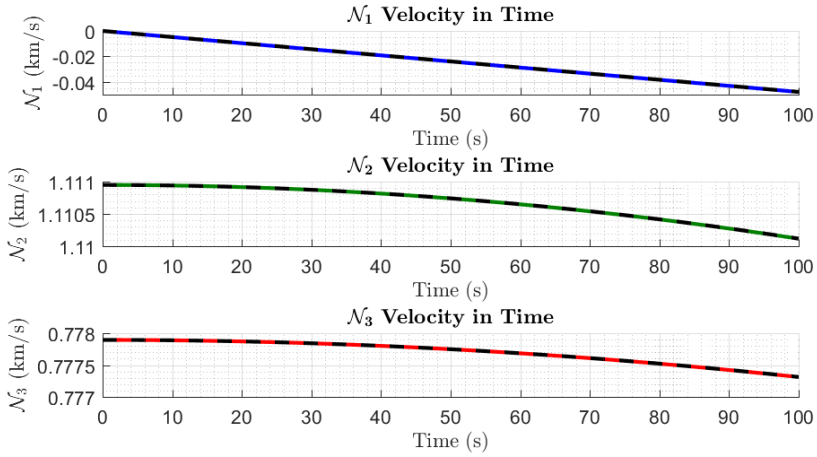

Figure 5.12 Velocity Under Unmodeled Dynamics

Figure 5.13 illustrates how the difference in Euler angles is also negligible.

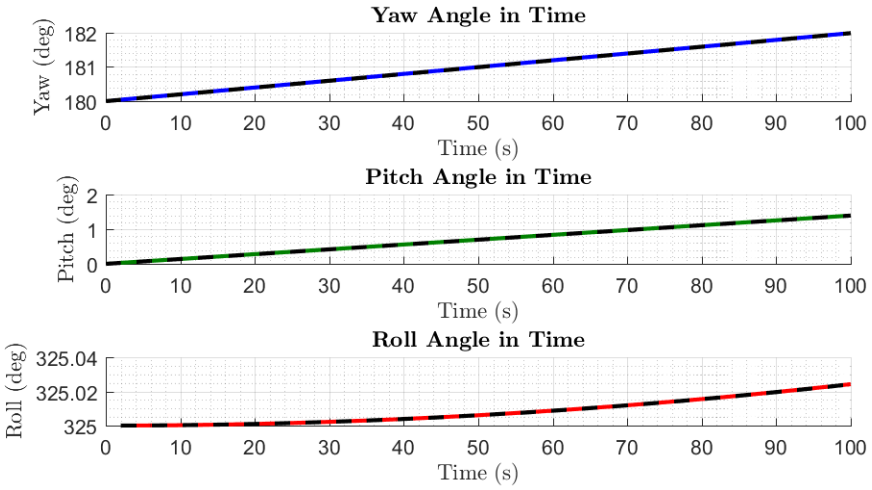

Figure 5.13 Attitude Under Unmodeled Dynamics

As with the other states, the angular velocity differences in Figure 5.14 are very small and and converge to zero, illustrating the controller is working.

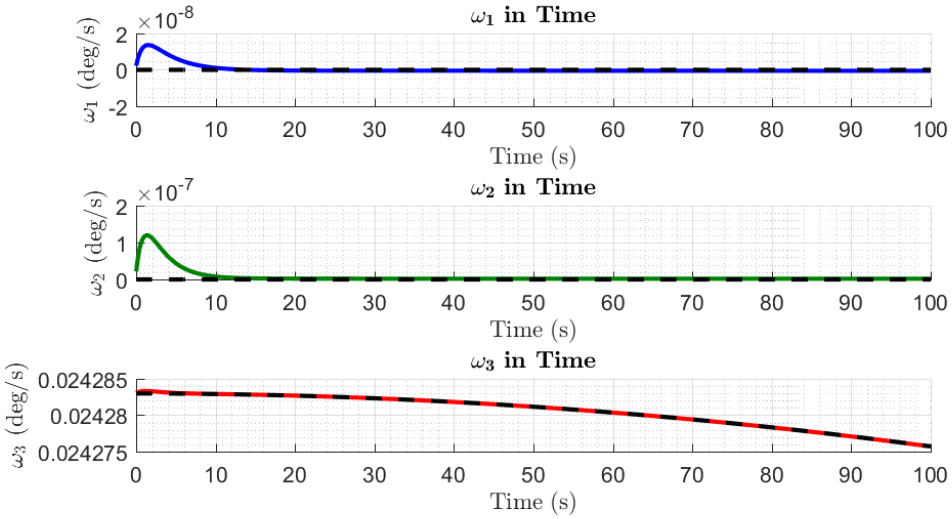

Figure 5.14 Angular Velocity Under Unmodeled Dynamics

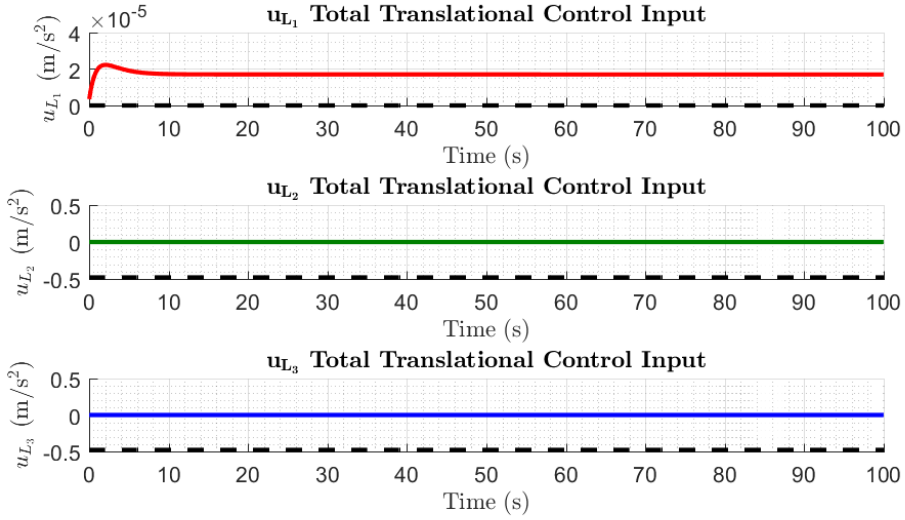

Figure 5.15 UK Translational Control Under Unmodeled Dynamics

Figure 5.15 illustrates the control from the UK formulation in the perturbed and unperturbed case, whereas Figure 5.16 illustrates the Morse-Lyapunov based controller input. The differences in Figure 5.15 are due to the upperbound of the perturbations seen in Equation (90).

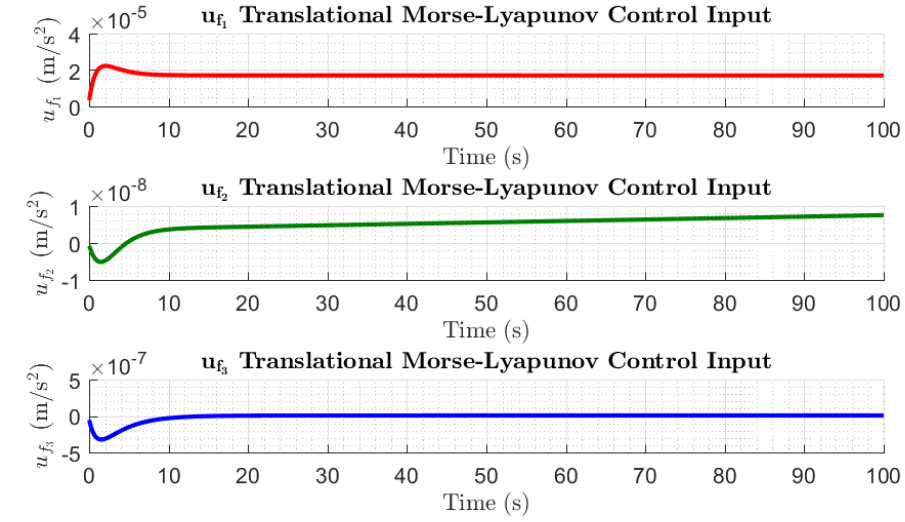

Figure 5.16 M-L Translational Control Under Unmodeled Dynamics

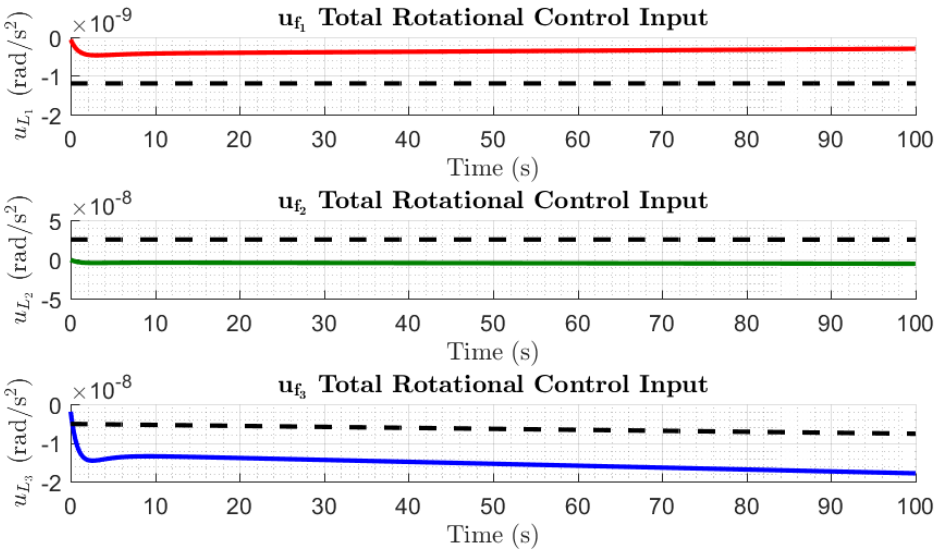

Figure 5.17 UK Rotational Control Under Unmodeled Dynamics

In a similar sense, Figure 5.18 illustrates the control input from the Morse-Lyapunov based controller, whereas Figure 5.17 illustrates the control from the UK formulation both in the perturbed and unperturbed case. The differences seen in Figure 5.17 are due to the influence of the upperbound of the perturbations seen in Equation (90).

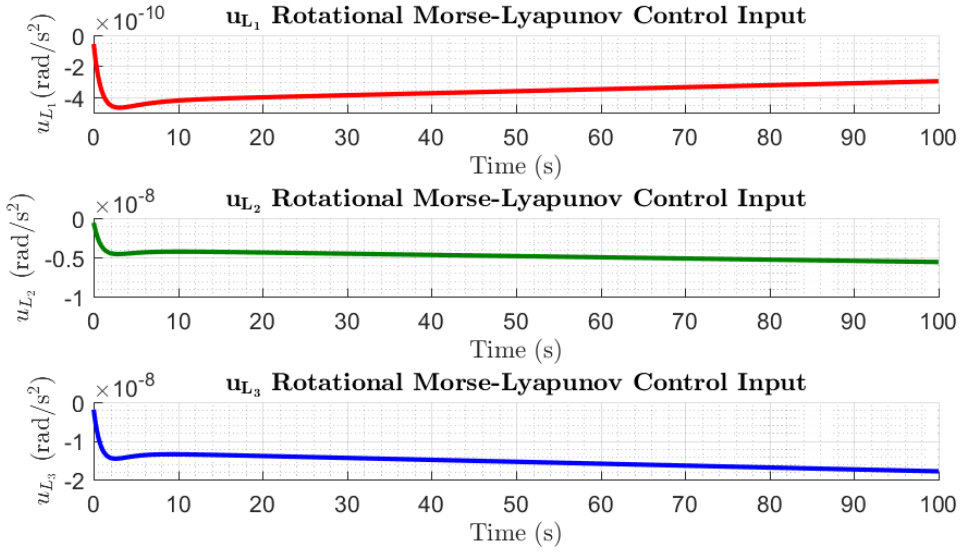

Figure 5.18 M-L Rotational Control Under Unmodeled Dynamics

6. Inequality Constraints Within UK Formulation

Udwadia-Kalaba formulation has been used and defined extensively for equality constraints. However, treatment of inequality constraints has not yet been extended to UK formulation. As such, optimality conditions of inequality constraints are discussed and a new approach to treating these inequalities within UK formulation is proposed.

6.1. Karush-Kuhn-Tucker Conditions

When inequality constraints are added to an optimization problem, several optimality conditions called the Karush-Kuhn-Tucker (KKT) conditions must be satisfied (Kuhn & Tucker, 1951). Assume a general optimization problem.

$$\begin{aligned} \text{minimize} \quad & \mathcal{J}(\mathbf{x}) \\ \text{subject to:} \quad & \mathbf{d}(\mathbf{x}) = \mathbf{0} \\ & \mathbf{g}(\mathbf{x}) \leq \mathbf{0} \end{aligned}$$

where $\mathbf{x}$ is the set of decision variables and $\mathcal{J}$ is a scalar cost function. The Hamiltonian function for a general problem of this form can be define.

$$\mathcal{H}(\mathbf{x}, \boldsymbol{\mu}, \boldsymbol{\lambda}) = \mathcal{J}(\mathbf{x}) + \boldsymbol{\mu}^T \mathbf{g}(\mathbf{x}) + \boldsymbol{\lambda}^T \mathbf{d}(\mathbf{x}) \tag{91}$$

For dynamic systems, the dynamics are imposed in equality constraints $\mathbf{d}(\mathbf{x}) = \mathbf{f}(\mathbf{x}, \mathbf{u}, t) - \dot{\mathbf{x}}$. As a result, the Lagrangian can be defined.

$$\mathcal{L}(\mathbf{x}, \boldsymbol{\mu}, \boldsymbol{\lambda}) = \mathcal{J}(\mathbf{x}) + \boldsymbol{\mu}^T \mathbf{g}(\mathbf{x}) + \boldsymbol{\lambda}^T \left(\mathbf{f}(\mathbf{x}, \mathbf{u}, t) - \dot{\mathbf{x}}\right) \tag{92}$$

The four KKT conditions are given below. Note $\mathbf{x}^*$ denotes an optimal set of decision variables or parameters.

Table 6.1
KKT Conditions for Parameter Optimization Problems

Stationarity Condition:	$\mathcal{J}_{\mathbf{x}}(\mathbf{x}^*) + \mu^T \mathbf{g}_{\mathbf{x}}(\mathbf{x}^*) + \boldsymbol{\lambda}^T \mathbf{d}_{\mathbf{x}}(\mathbf{x}^*) = 0$
Primal Feasibility:	$\mathbf{d}(\mathbf{x}^*) = \mathbf{0}$ $\mathbf{g}(\mathbf{x}^*) \leq \mathbf{0}$
Dual Feasibility:	$\boldsymbol{\mu} \geq \mathbf{0}$
Complementary Slackness:	$\boldsymbol{\mu}^T \mathbf{g}(\mathbf{x}^*) = 0$

These conditions can be enforced in indirect optimization problems. If more direct methods are used, these conditions can be checked to see if an optimal solution has been determined. As has been alluded to, two different types of optimization problems exist: direct and indirect methods. In general terms, indirect optimization problems determine optimality conditions and then discretize the timespan. By comparison, direct optimization problems discretize the timespan and then apply the dynamics and optimality conditions at each discretized time point, or collocation point. Two of the most salient conditions in assessing optimality are the dual feasibility and complementary slackness conditions. The dual feasibility condition can be checked with relative ease. The complementary slackness condition, however, provides excellent insight into the nature of the system. Assuming an optimal solution $\mathbf{x}^*$ has been found, if the j^{th} inequality given by $g_j(\mathbf{x}^*)$ is binding (or active), then $g_j(\mathbf{x}^*) = 0$. This means $\mathbf{x}^*$ is on an outermost boundary of the feasible region. Hence, the Lagrange multiplier μ_j associated with that inequality constraint will be larger than zero. If, however, the inequality is not binding (or inactive), then $g_j(\mathbf{x}^*) \neq 0$, necessitating that $\mu_j = 0$ in order to satisfy the complementary slackness condition.

6.2. Pontryagin's Minimum Principle

Pontryagin's Minimum Principle states that the Hamiltonian at the optimal control input must be less than or equal to the Hamiltonian for all other admissible controls (Pontryagin & Neustadt, 1986). In other words,

$$\mathcal{H}(\mathbf{x}^*, \mathbf{u}^*, \boldsymbol{\lambda}^*, \boldsymbol{\mu}^*, t) \leq \mathcal{H}(\mathbf{x}^*, \mathbf{u}, \boldsymbol{\lambda}^*, \boldsymbol{\mu}^*, t), \tag{93}$$

for all admissible $\mathbf{u}$. It can be shown that under minimum-time control (meaning the cost function is some function of time), the optimal control adopts the form of a bang-bang controller (Lewis et al., 2012).

6.3. Slack and Excess Variables

In many canonical forms of static optimization for linear and nonlinear programs, inequality constraints are transformed into equality constraints via introduction of a slack or

excess variable (Griva & Nash, 2017). For example, the inequality $x \geq 5$ would become $x - e = 5$ and the inequality $x \leq 6$ would become $x + s = 6$, where s and e are the slack and excess variables respectively.

6.3.1. Less Than Inequality Constraint

Consider an inequality where it is desired for the function $h(\mathbf{q}, \dot{\mathbf{q}}, t)$ to be less than or equal to zero $h(\mathbf{q}, \dot{\mathbf{q}}, t) \leq 0$. Recall q, $\dot{q}$, and $\ddot{q}$ are the generalized positions, velocities, and accelerations of the system of particles in Equation (1) for usage within UK formulation. This inequality can be rewritten as an equality constraint with a slack variable, a method used often in static optimization programs per Griva and Nash (2017).

$$h(\mathbf{q}, \dot{\mathbf{q}}, t) + s = 0 \tag{94}$$

Note s is a function of time. However, s must be greater than or equal to zero. Therefore, s is selected in the form of $s = q^2$ to yield the equality constraint and its derivatives

$$h(\mathbf{q}, \dot{\mathbf{q}}, t) + q^2 = 0 \tag{95a}$$

$$\dot{h}(\mathbf{q}, \dot{\mathbf{q}}, t) + 2q\dot{q} = 0 \tag{95b}$$

$$\ddot{h}(\mathbf{q}, \dot{\mathbf{q}}, t) + 2(q\ddot{q} + \dot{q}^2) = 0 \tag{95c}$$

For this purpose, a new variable q has been introduced to the system and must be appended to the $\mathbf{q}$ vector.

6.3.2. Greater Than Inequality Constraints

Consider an inequality where it is desired for the function $h(\mathbf{q}, \dot{\mathbf{q}}, t)$ to be greater than or equal to zero $h(\mathbf{q}, \dot{\mathbf{q}}, t) \geq 0$. This inequality can be rewritten as an equality constraint with an excess variable (Griva & Nash, 2017).

$$h(\mathbf{q}, \dot{\mathbf{q}}, t) - e = 0 \tag{96}$$

Note e is a function of time. Similarly, e must be greater than or equal to zero. Therefore, e

is selected to be in the form of $e = p^2$ to yield the equality constraint and its derivatives.

$$h(\mathbf{q}, \dot{\mathbf{q}}, t) - p^2 = 0 \tag{97a}$$

$$\dot{h}(\mathbf{q}, \dot{\mathbf{q}}, t) - 2p\dot{p} = 0 \tag{97b}$$

$$\ddot{h}(\mathbf{q}, \dot{\mathbf{q}}, t) - 2(p\ddot{p} + \dot{p}^2) = 0 \tag{97c}$$

For this purpose, a new variable p has been introduced to the system and must be appended to the $\mathbf{q}$ vector.

6.3.3. Slack Dynamics Specification

Note that the values of $\dot{q}$ and $\dot{p}$ are required to propagate the motion of the system and form the constraints. One approach to determining these quantities is by rearranging Equations (95b) and (97b). However, if the chosen initial conditions are such that the constraint is active $h(\mathbf{q}_0, \dot{\mathbf{q}}_0, t_0) = 0$, Equations (95b) and (97b) have a singularity. In fact, choosing the slack and excess dynamics in this fashion will prohibit the system from having truly active inequality constraints, but the response will converge to a minimum control if one exists. However, tying the slack and excess dynamics to the physical dynamics ensures that the system will not converge to a false minimum, which may occur if the slack and excess dynamics are constrained to obey some function of time. As such, just as there exists an optimal $\mathbf{x}^*$, there are optimal slack and excess variables.

6.4. Direct Optimization of Dynamical System Trajectories

Using a direct optimization scheme, the minimum control needed to satisfy a constraint can be determined. The finer details of the method are outlined by Hedengren et al. (2014), but the key points are presented here. Direct optimization methods discretize the timespan into collocation points such that a parameter optimization problem can be solved. To get the time history curve to match the motion of the system, interpolation between the collocation points is conducted. The optimization methodology presented here uses Lobatto Quadrature and orthogonal collocation to discretize the timespan. Within Lobatto Quadrature, the

interval along which the Lobatto function is defined is $[-1, 1]$. The collocation points are the first $(n-1)$ roots of the function P'_{n-1}, where P_n is the Legendre polynomial of degree n. Here, n is the chosen number of collocation points, including the first and last values on the interval. The timespan can then be scaled to fit along $[0, 1]$, from which the collocation points can be tied together. Scaling this up to some maximum time is a simple multiplication of the elements of the timespan.

This collocation method functionally converts the infinite parameter continuous time problem into a finite parameter problem. However, the dynamics still have yet to be imposed as constraints on the system. In Hedengren et al. (2014), the process of translating a system of differential equations into a differential algebraic equation is detailed. This converts a continuous-time trajectory optimization problem into a parameter optimization problem, which nonlinear-program (NLP) solvers can accommodate fairly well (Kelly, 2016; Liu et al., 2017; Kelly, 2017). This is done by relating the derivatives of the states $\dot{x}$ at each collocation point to the difference between the state x and the initial condition. Using the same definition of n as in the Lobatto Quadrature (n is number of discrete times, or collocation points, including the outer bounds), the differential algebraic equation (DAE) can be expressed as follows:

$$t_n R_{(n-1)\times(n-1)} \begin{bmatrix} \dot{x}_1 \\ \dot{x}_2 \\ \vdots \\ \dot{x}_{n-1} \end{bmatrix} = \begin{bmatrix} x_1 \\ x_2 \\ \vdots \\ x_{n-1} \end{bmatrix} - \begin{bmatrix} x_0 \\ x_0 \\ \vdots \\ x_0 \end{bmatrix} \tag{98}$$

Assume an interpolation of the state x between collocation points by an $(n-1)^{th}$ degree polynomial.

$$x(t) = a_0 + a_1 t + a_2 t^2 + \cdots + a_n t^{n-2} = \sum_{i=1}^{n} a_i t^{n-i} \tag{99}$$

The relationship between the derivative and its corresponding state at each collocation point can be determined.

$$t_n R_{(n-1)\times(n-1)} = P^{-1}, \tag{100}$$

Here, the matrix P is required.

$$P = \begin{bmatrix} 1 & 2t_1 & 3t_1^2 & \dots & (n-1)t_1^{n-2} \\ 1 & 2t_2 & 3t_2^2 & \dots & (n-1)t_2^{n-2} \\ \vdots & \vdots & \vdots & \vdots & \vdots \\ 1 & 2t_{n-1} & 3t_{n-1}^2 & \dots & (n-1)t_{n-1}^{n-2} \end{bmatrix} \begin{bmatrix} t_1 & t_1^2 & \dots & t_1^{n-1} \\ t_2 & t_2^2 & \dots & t_2^{n-1} \\ \vdots & \vdots & \vdots & \vdots \\ t_n & t_n^2 & \dots & t_{n-1}^{n-1} \end{bmatrix}^{-1}$$

With these definitions, the optimization problem can be expressed in a form that a NLP solver can understand. The following notation is consistent with that used in Matlab's NLP solver, *fmincon*. This is a general formulation of a parameter optimization problem, as opposed to a continuous time trajectory optimization problem.

$$\begin{aligned} \text{minimize} \quad & \mathcal{J} = \int_{t_0}^{t_f} \mathbf{u}^T M^{-1} \mathbf{u} dt \\ \\ \text{subject to:} \quad & \bar{A}_{eq}\mathbf{x} = \bar{\mathbf{b}}_{eq} \\ & \bar{A}\mathbf{x} \leq \bar{\mathbf{b}} \\ & \bar{c}_{eq}(\mathbf{x}) = 0 \\ & \bar{c}(\mathbf{x}) \leq 0 \\ & \bar{lb} \leq \mathbf{x} \leq \bar{ub} \end{aligned}$$

In the continuous case as derived in the UK formulation, the constraints were represented by a matrix A multiplied by the vector of second derivatives, whose product was equal to a vector $\mathbf{b}$. This expression is somewhat different from that expressed above. The quantity $\mathcal{J}$ is a scalar cost function the solver will try to minimize. The vector $\mathbf{x}$ is a vector of parameters or decision variables that the NLP solver will vary. In the case of dynamic systems, the vector will be comprised of the positions, velocities, accelerations, and control inputs at each time step. So, if the system is described in $\mathbb{R}^3$ and there are n collocation points, $\mathbf{x}$ will at least have $(3)(4)(n-1)$ decision variables, depending on the nature of the

control inputs; all other matrices and vectors will be sized accordingly. $\bar{A}_{eq}$ is the matrix of values representing the left hand side of linear equality constraints on the vector $\mathbf{x}$, whereas $\bar{\mathbf{b}}_{eq}$ is the vector representing the right hand side of that equality. The same applies for $\bar{A}$ and $\bar{b}$, except for linear inequalities. The vectors $\bar{c}_{eq}$ and $\bar{c}$ are nonlinear equality and inequality constraints respectively.

6.5. Numerical Simulation Results and Discussion

Two different examples that the inequality constraint formulation can be applied to are presented here. One methodology looks at a simple spring-mass damper. This case is relevant and lends itself to an intuitive dynamic behavior. This makes analyzing the optimality and system behavior easier. The second case is focused on trajectory maintenance for a spacecraft that is allowed to drift a certain difference from a reference trajectory.

6.5.1. Spring-Mass-Damper Example

Consider the simple dynamic system of a spring-mass-damper.

$$m\ddot{x} + b\dot{x} + kx = 0$$

Here, the constants are chosen to be $m = 2$kg, $b = 5$Ns/m, $k = 10$N/m. As such, there are several different cases of inequalities that can exist. These are explored here.

6.5.1.1. Greater Than Inequality

Consider the case of a greater than (GT) inequality constraint that requires the mass displacement $x \geq 5$. Figures 6.1 through 6.6 illustrate the results of the UK formulation with the modified excess variable constraints. The physical displacement of the mass over time is given by the blue line in Figure 6.1 and the red line represents the value of the constraint. As the constraint was formatted as $x - e = x - p^2 = 5$, it would be expected that this should hold for all time, a fact confirmed by the red line in Figure 6.1. As is expected, the system's physical displacement converges to the equilibrium state within the admissible region that corresponds to the minimum required constraint force. The physical velocity of the mass is given by Figure 6.2. Note the velocity converges to a final steady state of zero.

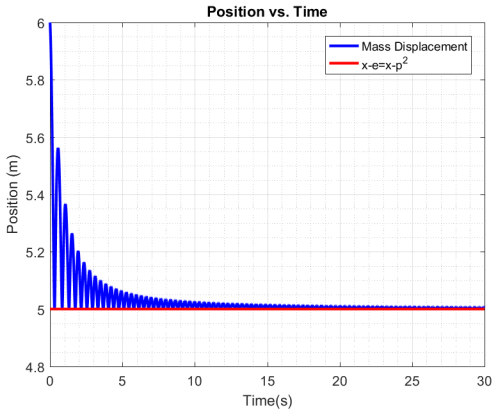

Figure 6.1 GT SMD Position

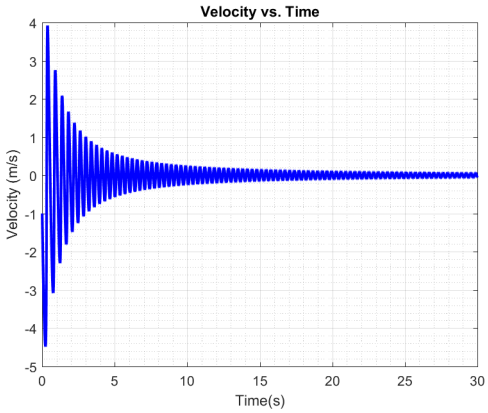

Figure 6.2 GT SMD Velocity

The blue line in Figure 6.3 represents the control acceleration acting on the mass to satisfy the constraint. This converges to the expected acceleration needed to keep the mass at $x = 5$. Furthermore, within the context of Pontryagin's Minimum Principle, it can be seen that the control acceleration impulsively increases whenever the constraint is about to become active. This acts in a fashion similar to a bang-bang controller, suggesting that for that one instance of constraint activation, the formulation is solving a minimum-time optimization problem that results in a bang-bang-like control. The restoring forces of the spring and damper return the mass to a point where the constraint may become active again, leading to another impulsive, minimum time control. Figure 6.4 illustrates the control effort of this approach. It confirms what was seen in Figure 6.3; since the control effort has a constant slope, the control acceleration is a constant.

Figure 6.5 illustrates the Lagrange multipliers associated with the equality constraint that was formed from the inequality constraint. Assessing the complementary slackness KKT condition, it can be seen that the product of the Lagrange multipliers and the constraint value (given in Figure 6.6 by the green line) is initially larger than zero, but approaches zero as time goes to infinity, suggesting the transient behavior is not optimal, but the steady state is. This is further verified by examination of the primal feasibility condition, which states that for inequality constraints, $\mathbf{g}(\mathbf{x}^*) \leq 0$. In the steady state case, the inequality converges to zero, indicating that the steady state is optimal.

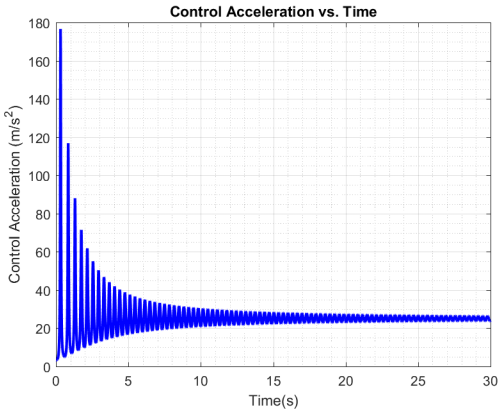

Figure 6.3 GT SMD Control Acceleration

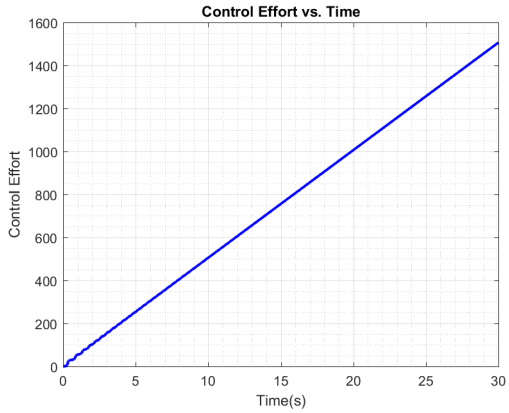

Figure 6.4 GT SMD Control Effort

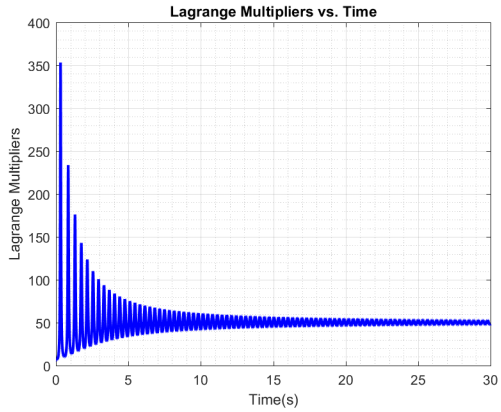

Figure 6.5 GT SMD Lagrange Multipliers

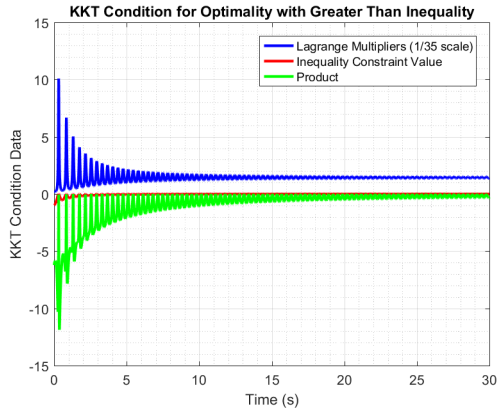

Figure 6.6 GT SMD KKT Conditions

6.5.1.2. Less Than Inequality

Consider a less than (LT) inequality problem where it is desired to keep $x \leq 1$. The results of the simulation using the slack variable transformation can be found in Figures 6.7 through 6.12. Note the mass's physical displacement in Figure 6.7 reaches the upper limit ($x = 1$) but does not exceed it. The system then proceeds to the equilibrium condition where the minimum control acceleration is needed, which in the case of a spring mass damper, is at zero displacement and velocity, permitting the control acceleration to be zero. The result from the position response is validated in Figures 6.8 through 6.10 which show the mass's velocity, control acceleration, and control effort. The mass's velocity goes to zero, as does the control acceleration. Furthermore, the control effort becomes horizontal, indicating no

additional control has been applied to the system. These observations show that the slack and excess variable formulation can cause a system to converge to a natural minimum control if selection of the slack and excess dynamics is done carefully.

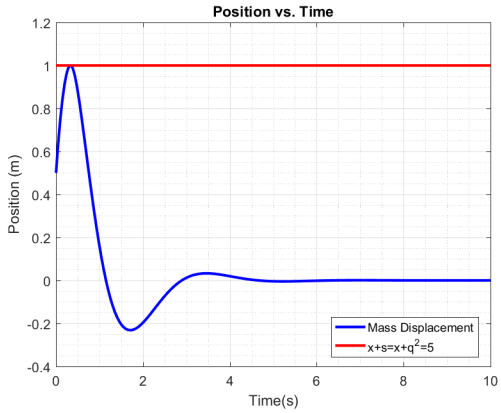

Figure 6.7 LT SMD Position

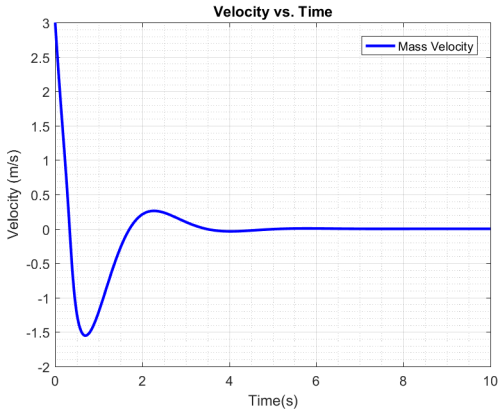

Figure 6.8 LT SMD Velocity

It is also relevant to note that the control acceleration also behaves similar to the greater-than inequality case, where a bang-bang-like control satisfies the constraint.

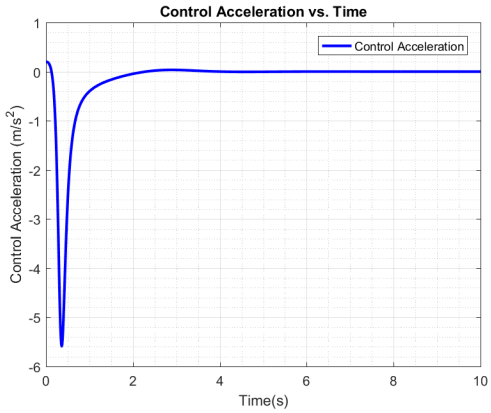

Figure 6.9 LT SMD Control Acceleration

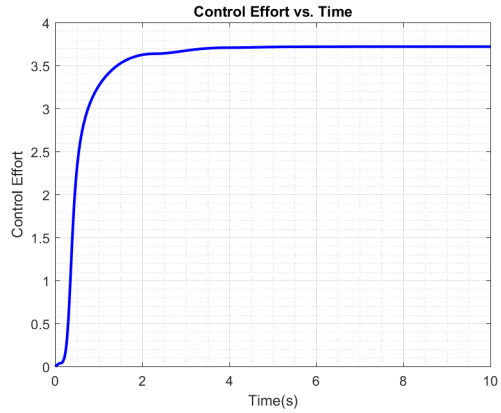

Figure 6.10 LT SMD Control Effort

Figures 6.11 and 6.12 illustrate the Lagrange multipliers associated with the constraint and the KKT complementary slackness condition. Once again, examining the primal feasibility condition in Figure 6.12, it would appear that the time history is optimal because the inequality is negative semidefinite for the whole time history. However, note that the product of the constraint value and the Lagrange multipliers goes to zero only at the steady

state. Similar to the greater-than inequality case, the transient behavior appears to be sub-optimal from a minimal control perspective, but the steady state solution is optimal.

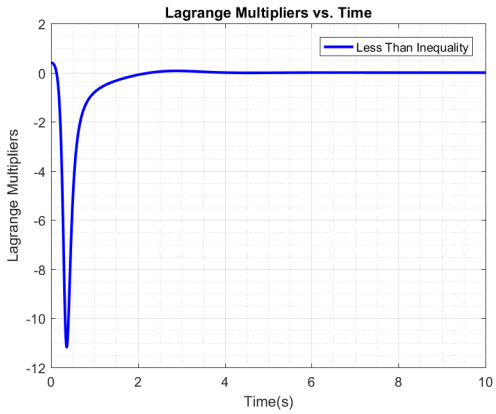

Figure 6.11 LT SMD Lagrange Multipliers

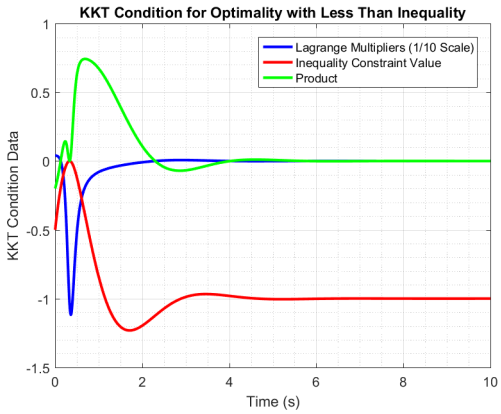

Figure 6.12 LT SMD KKT Conditions

6.5.1.3. Bounding Constraints

For the case of bounding inequalities (BI), the data can be analyzed in the same manner as for the individual greater than and less than inequalities. For this problem, the constraints are formatted such that $1 \leq x \leq 2$. Initial conditions are specifically chosen for this simulation such that both constraints would be active at some point in the timespan.

Examination of Figure 6.13 shows that the mass displacements reaches the upper bound, but does not exceed it. Furthermore, the mass displacement then falls and converges to an admissible point with minimal necessary control. Figure 6.14 illustrates the velocity of the mass. As the timespan goes to infinity, the mass velocity converges to zero.

It can be seen that the control acceleration counters the motion of the mass when it appears a constraint would be active. It is also important to note that the control acceleration converges to a constant value. Applying Newton's second law, it can be confirmed that for the spring and damping coefficients, such an acceleration will ensure the system is static. The control effort confirms the information about the mass's displacement as its steady state slope is a constant, just as the control acceleration in the steady state is constant.

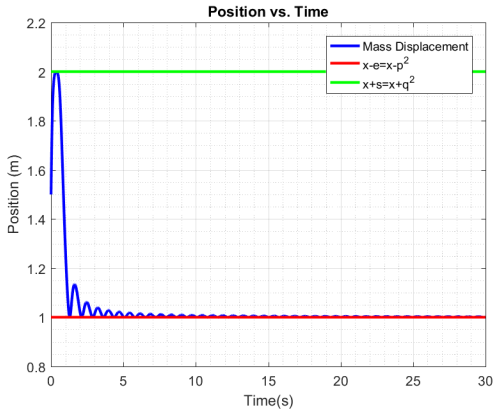

Figure 6.13 BI SMD Position

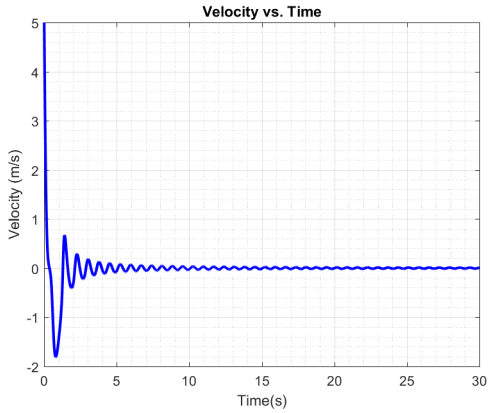

Figure 6.14 BI SMD Velocity

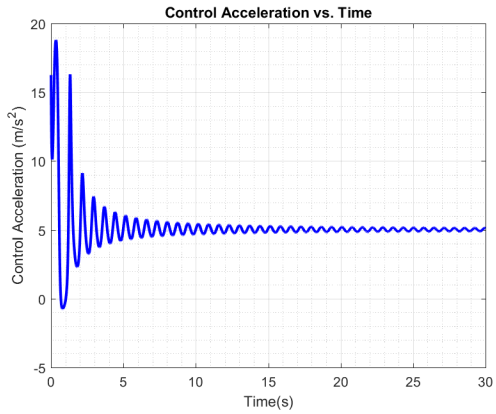

Figure 6.15 BI SMD Control Acceleration

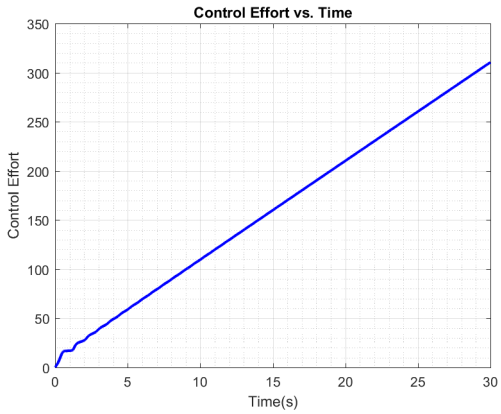

Figure 6.16 BI SMD Control Effort

Figure 6.17 shows the Lagrange multipliers for each inequality.

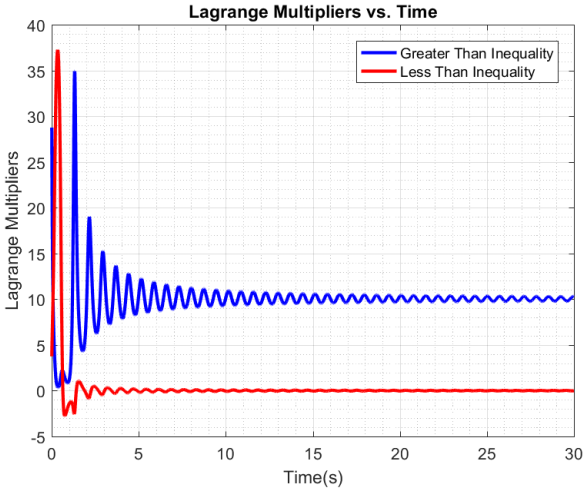

Figure 6.17 BI SMD Lagrange Multipliers

The complementary slackness condition for the less than and greater than inequalities can be assessed for optimality by examining Figures 6.18 and 6.19 respectively.

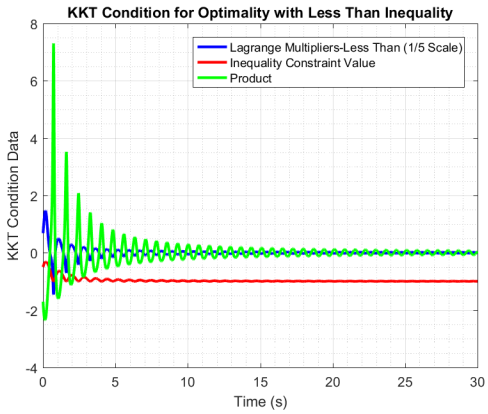

Figure 6.18 BI SMD-LT KKT Conditions

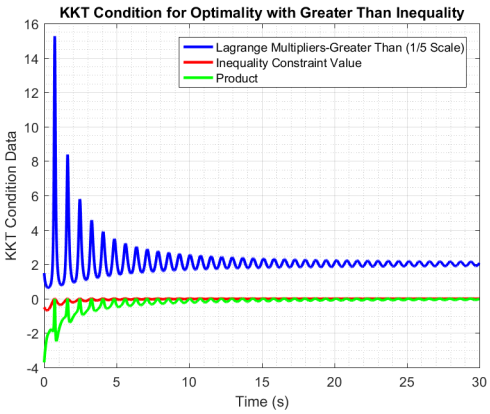

Figure 6.19 BI SMD-GT KKT Conditions

It is important to note that in Figures 6.18 and 6.19, the complementary slackness condition is not obeyed, but the primal feasibility condition is satisfied. The product between the Lagrange multiplier μ and the value of the inequality constraint should be zero if an optimal solution is achieved. Once again, this suggests that the solution is suboptimal in the transient case.

6.5.1.4. Direct Optimization Results

Once again consider the spring-mass-damper system. This is a one-dimensional system with one possible control input that is being optimized by minimizing the Gaussian. As such, if there are n total collocation points, then $\mathbf{x}$ adopts a specific form.

$$\mathbf{x} = \begin{bmatrix} x_1 & \dots & x_n & \dot{x}_1 & \dots & \dot{x}_n & \ddot{x}_1 & \dots & \ddot{x}_n & u_1 & \dots & u_n \end{bmatrix}^T$$

Here, x_n, $\dot{x}_n$, $\ddot{x}_n$, and u_n are the position, velocity, acceleration, and control input at the collocation point corresponding to t_n. This lends itself to formulation for the equality and inequality constraints described above.

$$\bar{A}_{eq} = \begin{bmatrix} -I_{n-1} & t_n R & 0_{n-1} & 0_{n-1} \\ 0_{n-1} & -I_{n-1} & t_n R & 0_{n-1} \\ \frac{k}{m} I_{n-1} & \frac{b}{m} I_{n-1} & I_{n-1} & -\frac{1}{m} I_{n-1} \end{bmatrix} \quad \bar{\mathbf{b}}_{eq} = \begin{bmatrix} -x_0 Q_{n-1\times 1} \\ -\dot{x}_0 Q_{n-1\times 1} \\ 0_{n-1\times 1} \end{bmatrix}$$

These quantities require definition of a quantity $Q_{\alpha\times\beta}$ which denotes an $\alpha \times \beta$ matrix of ones. The first row relates the velocity to position, and the second row relates the velocity to acceleration with the differential algebraic equations. The third row is the kinetic equation of motion. Here, the results from the direct optimization of the spring-mass-damper system under inequality constraints are presented and compared with the slack and excess variable formulation.

Inequality constraints bounding the position at each collocation point between $x = 1$ and $x = 2$ are described by the $\bar{A}$ and $\bar{b}$ matrices which are defined for the spring-mass-damper problem as follows:

$$\bar{A} = \begin{bmatrix} -I_{r1} & 0_{3\times(r-1)} \\ I_{r-1} & 0_{3\times(r-1)} \end{bmatrix} \quad \bar{b} = \begin{bmatrix} -1 \\ 2 \end{bmatrix}$$

Functionally, setting an upper and lower bound on the position would accomplish the same goal as these two inequality constraints. In addition, there are no nonlinear constraints in this example, so those values are neglected. The continuous time optimal control problem can be now solved by as a parameter optimization problem by a NLP solver.

The following numerical simulations adopt a maximum time of thirty seconds and the timespan is discretized into five collocation points. The results from this optimization and their comparison with the proposed method utilizing slack variables can be seen in Figures 6.20 through 6.27. The optimal position time history determined from the direct optimization can be seen in Figure 6.20. Of specific importance is the the initial displacement. Both started from the same initial conditions. However, when using the direct optimization scheme and interpolating, the system displacement was forced to a minimum

faster. They both converge to the same steady state. Similar to the position response, the direct optimization scheme illustrates that both treatments of inequality constraints converge to the same steady state that matches intuition about the system dynamics.

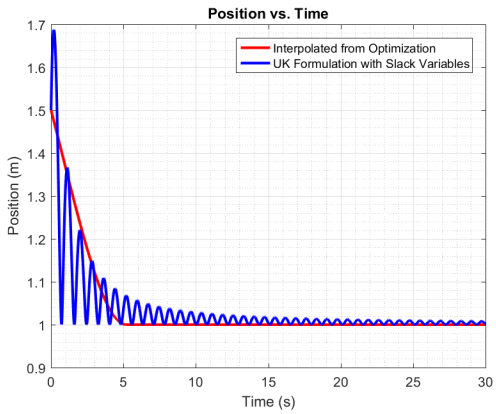

Figure 6.20 Optimal Position Comparison

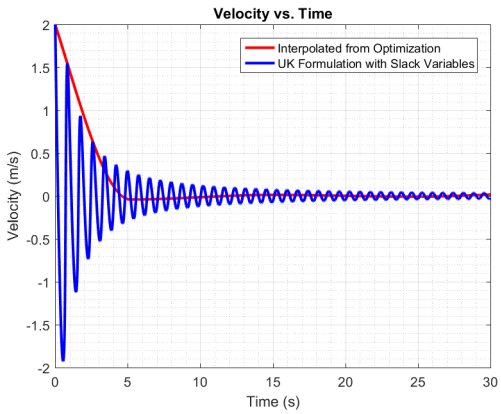

Figure 6.21 Optimal Velocity Comparison

The control accelerations capture the steady state dynamics. The initial acceleration is assumed to be zero, which can bee seen in the interpolation in Figure 6.22. Examination of Figure 6.23 proves the slack variable approach is greater than the optimal solution derived from the direct optimization method. This is attributable to the singularity issue noted in the formulation of the slack variable approach. As p and q can never be zero exactly, the formulation will keep the displacement of the mass away from the active constraint limits. This explains the damped, oscillatory behavior for this system.

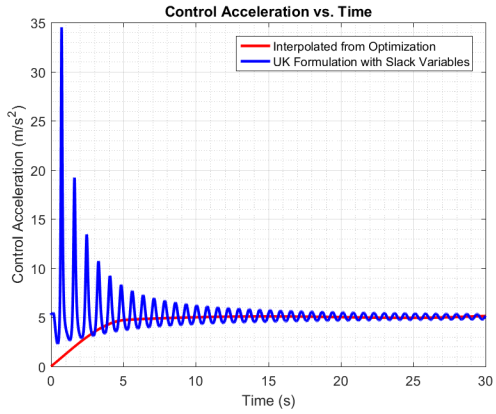

Figure 6.22 Optimal Control Comparison

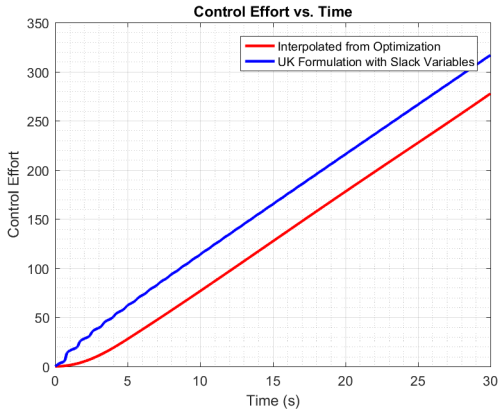

Figure 6.23 Optimal Ctrl. Eff. Comparison

The Lagrange multipliers for each constraint can be seen in Figures 6.24 and 6.25. The less than inequality Lagrange multipliers converge to zero, which makes sense because the less than inequality is not active. However, the determination of the Lagrange multipliers in the greater than case is not very consistent with those from the UK formulation. Such a difference prompts brief investigation into how the Lagrange multipliers are determined by NLP solvers. Some will choose fixed estimates of the Lagrange multipliers, whereas others will apply more adaptive methods (Liu et al., 2017; Betts, 1998). However, it has been noted with Matlab and *fmincon* specifically that determination of the Lagrange multipliers may not be accurate (Nocedal & Wright, 2006). Furthermore, increasing the number of collocation points too much leads to near singular collocation matrices. Such collocation matrices cause problems in determination of the Jacobians and Hessian matrices that in turn lead to fatal errors in Lagrange multiplier determination (Nocedal & Wright, 2006). In summary, the use of some Lagrangian-based optimization solvers can result in inaccurate Lagrange multipliers (Fahroo & Ross, 2000). The development shown here does not rely on the determination of the Lagrange multipliers and carries the advantages of the UK technique.

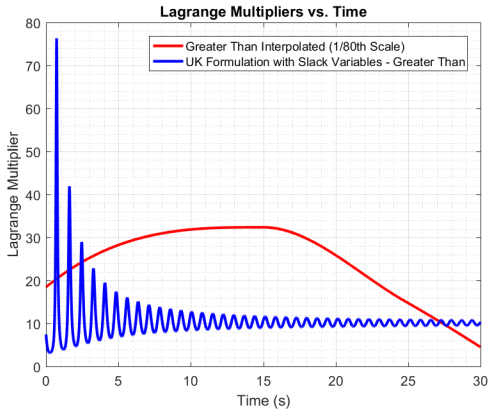

Figure 6.24 GT Lagrange Mult. Comp.

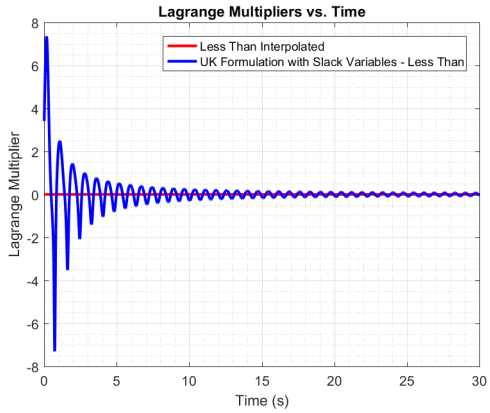

Figure 6.25 LT Lagrange Mult. Comp.

Figures 6.26 and 6.27 show the complimentary slackness condition for these inequalities. It shows that the direct method obeys the primal feasibility, dual feasibility, and complimentary slackness conditions. As previously discussed, the UK formulation with

slack and excess appears not to satisfy the dual feasibility and complementary slackness conditions.

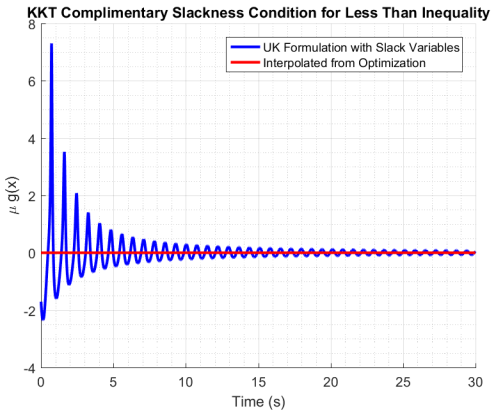

Figure 6.26 LT KKT Cond. Comp.

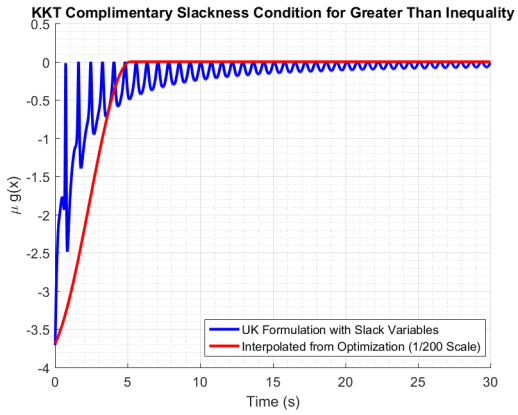

Figure 6.27 GT KKT Cond. Comp.

6.5.2. Trajectory Maintenance Example

Assume a reference trajectory exists that is defined by a time history of the position, velocity, and acceleration of a spacecraft given by $\mathbf{r}_r$, $\dot{\mathbf{r}}_r$, and $\ddot{\mathbf{r}}_r$ respectively. The actual position and velocity of the spacecraft are given by $\mathbf{r}$ and $\dot{\mathbf{r}}$. As such, the error in both of these quantities can be defined.

$$\mathbf{r}_e = \mathbf{r} - \mathbf{r}_r \qquad \dot{\mathbf{r}}_e = \dot{\mathbf{r}} - \dot{\mathbf{r}}_r$$

Let the magnitude of the error in the position and velocity vectors be confined to be less than some time-varying values $\delta(t)$ and $\gamma(t)$, respectively. Therefore, two constraints are possible.

$$g_1(\mathbf{q}, \dot{\mathbf{q}}, t) = ||\mathbf{r}_e|| - \delta(t) \leq 0 \tag{101}$$

$$g_1(\mathbf{q}, \dot{\mathbf{q}}, t) = ||\mathbf{r}_e|| - \delta(t) + q_1^2 = 0$$

$$g_2(\mathbf{q}, \dot{\mathbf{q}}, t) = ||\dot{\mathbf{r}}_e|| - \gamma(t) \leq 0 \tag{102}$$

$$g_2(\mathbf{q}, \dot{\mathbf{q}}, t) = ||\dot{\mathbf{r}}_e|| - \gamma(t) + \dot{q}_2^2 = 0$$

Note the values for the magnitude of $\mathbf{r}_e$ and $\dot{\mathbf{r}}_e$ are required.

$$||\mathbf{r}_e|| = \sqrt{(x - x_r)^2 + (y - y_r)^2 + (z - z_r)^2} \tag{103}$$

$$||\dot{\mathbf{r}}_e|| = \sqrt{(\dot{x} - \dot{x}_r)^2 + (\dot{y} - \dot{y}_r)^2 + (\dot{z} - \dot{z}_r)^2} \tag{104}$$

Differentiating Equations (101) and (102) twice and once respectively yields the following:

$$\begin{aligned}\ddot{g}_1 =& \frac{(x - x_r)(\ddot{x} - \ddot{x}_r) + (\dot{x} - \dot{x}_r)^2 + (y - y_r)(\ddot{y} - \ddot{y}_r) + (\dot{y} - \dot{y}_r)^2}{\sqrt{(x - x_r)^2 + (y - y_r)^2 + (z - z_r)^2}} + \dots \\ &\cdots + \frac{(\dot{z} - \dot{z}_r)(\ddot{z} - \ddot{z}_r) + (\dot{z} - \dot{z}_r)^2}{\sqrt{(x - x_r)^2 + (y - y_r)^2 + (z - z_r)^2}} - \dots \\ &\cdots - \frac{[(x - x_r)(\dot{x} - \dot{x}_r) + (y - y_r)(\dot{y} - \dot{y}_r) + (z - z_r)(\dot{z} - \dot{z}_r)]^2}{[(x - x_r)^2 + (y - y_r)^2 + (z - z_r)^2]^{\frac{3}{2}}} - \dots \\ &\cdots - \ddot{\delta}(t) + 2(q_1\ddot{q}_1 + \dot{q}_1^2)\end{aligned} \tag{105}$$

$$\dot{g}_2 = \frac{(\dot{x} - \dot{x}_r)(\ddot{x} - \ddot{x}_r) + (\dot{y} - \dot{y}_r)(\ddot{y} - \ddot{y}_r) + (\dot{z} - \dot{z}_r)(\ddot{z} - \ddot{z}_r)}{\sqrt{(\dot{x} - \dot{x}_r)^2 + (\dot{y} - \dot{y}_r)^2 + (\dot{z} - \dot{z}_r)^2}} - \dot{\gamma}(t) + 2\dot{q}_2\ddot{q}_2 \tag{106}$$

Expressing these constraints in the format given by Equation (1) yields the following:

$$A_1 = \begin{bmatrix} \frac{x - x_r}{||\mathbf{r}_e||} & \frac{y - y_r}{||\mathbf{r}_e||} & \frac{z - z_r}{||\mathbf{r}_e||} & 2q_1 \end{bmatrix} \tag{107}$$

$$\begin{aligned}b_1 =& \frac{\ddot{x}_r(x - x_r) - (\dot{x} - \dot{x}_r)^2 + \ddot{y}_r(y - y_r) - (\dot{y} - \dot{y}_r)^2 + \ddot{z}_r(z - z_r) - (\dot{z} - \dot{z}_r)^2}{||\mathbf{r}_e||} + \dots \\ &\cdots + \frac{[(x - x_r)(\dot{x} - \dot{x}_r) + (y - y_r)(\dot{y} - \dot{y}_r) + (z - z_r)(\dot{z} - \dot{z}_r)]^2}{||\mathbf{r}_e||^3} + \ddot{\delta}(t) - 2\dot{q}_1^2\end{aligned} \tag{108a}$$

or,

$$b_1 = \frac{\ddot{\mathbf{r}}_r^T\mathbf{r}_e - \dot{\mathbf{r}}_e^T\dot{\mathbf{r}}_e}{||\mathbf{r}_e||} + \frac{(\dot{\mathbf{r}}_e^T\mathbf{r}_e)^2}{||\mathbf{r}_e||^3} + \ddot{\delta}(t) - 2\dot{q}_1^2 \tag{108b}$$

Similarly, for Equation (106),

$$A_2 = \begin{bmatrix} \frac{\dot{x}-\dot{x}_r}{||\mathbf{r}_e||} & \frac{\dot{y}-\dot{y}_r}{||\mathbf{r}_e||} & \frac{\dot{z}-\dot{z}_r}{||\mathbf{r}_e||} & 2\dot{q}_2 \end{bmatrix} \tag{109}$$

$$b_2 = \frac{\ddot{x}_r(\dot{x}-\dot{x}_r) + \ddot{y}_r(\dot{y}-\dot{y}_r) + \ddot{z}_r(\dot{z}-\dot{z}_r)}{||\dot{\mathbf{r}}_e||} + \dot{\gamma}(t) \tag{110a}$$

or

$$b_2 = \frac{\ddot{\mathbf{r}}_r^T \dot{\mathbf{r}}_e}{||\dot{\mathbf{r}}_e||} + \dot{\gamma}(t) \tag{110b}$$

The reference trajectory for the lunar mass concentration problem is developed by integrating the simple two-body problem around the Moon. Both orbits have approximately an 11° inclination as this is not a frozen orbit and has historically displayed appreciable perturbations from nonuniform lunar gravity. The simulation then employed a more advanced gravity model for use with the UK Formulation. The GRAIL mission studied lunar gravity and developed very accurate gravity models that included as many as 1200 degrees (Lemoine et al., 2013, 2014). The synthesized data for this model can be obtained and utilized. For the sake of this analysis, a model up to degree 660 was selected (Konopliv et al., 2013). The point mass spacecraft was chosen to have a mass of 300kg.

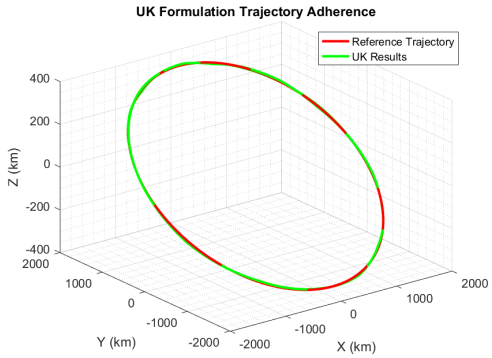

Figure 6.28 Trajectory Maintenance - Orbit Comparison

Figure 6.28 illustrates the comparison between the reference and UK trajectory. Figure 6.29 illustrates the position error for the lunar orbit simulation with the detailed gravity model.

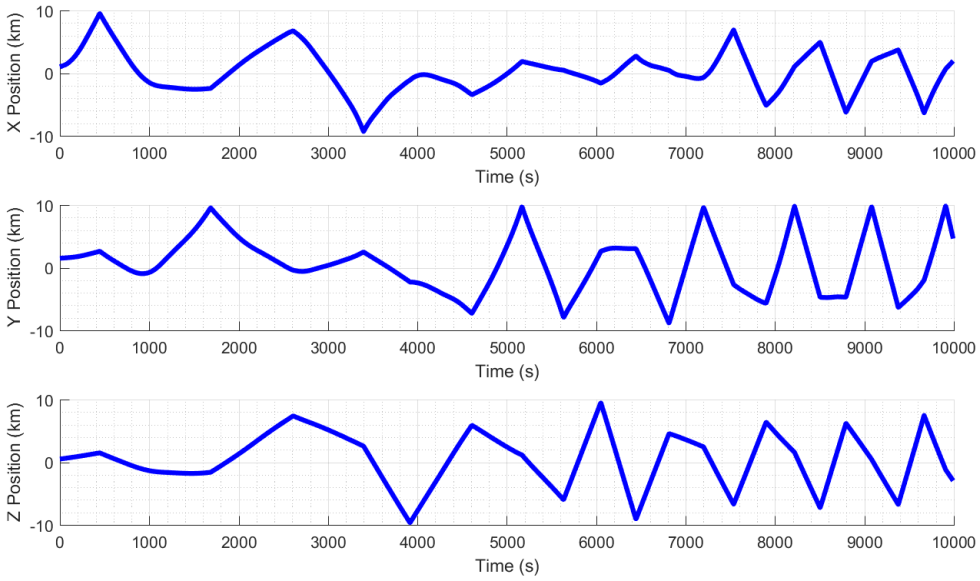

Figure 6.29 Trajectory Maintenance - Position Error from Reference Orbit

Figures 6.30 and 6.31 show the relative motion of the spacecraft around the reference trajectory and adherence to the constraint, respectively. Once again, it can be seen that the dynamic behavior obeys the constraint.

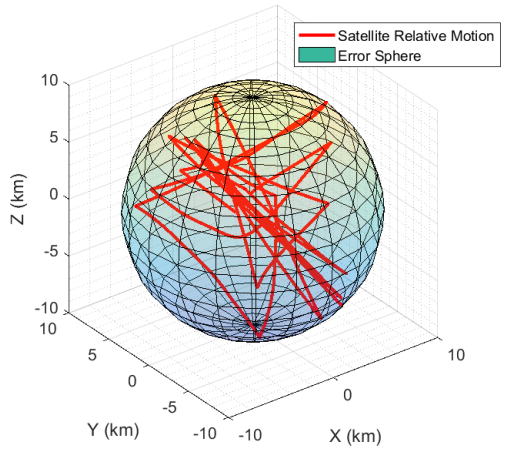

Figure 6.30 Trajectory Maintenance - Relative Motion About Reference Trajectory

Figures 6.32, 6.33, and 6.34 illustrate the velocity error, control acceleration, and control effort per unit mass of the spacecraft respectively.

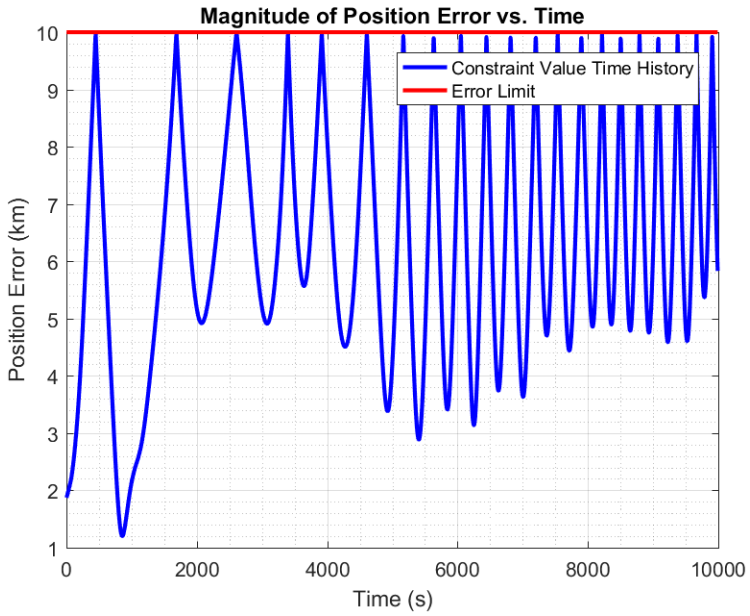

Figure 6.31 Trajectory Maintenance - Position Error Magnitude

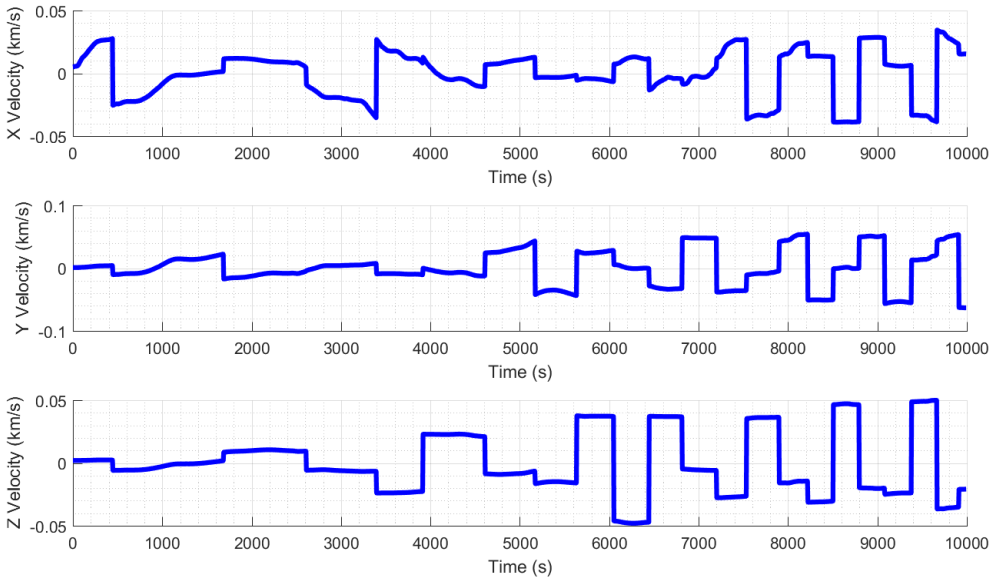

Figure 6.32 Trajectory Maintenance - Velocity Error

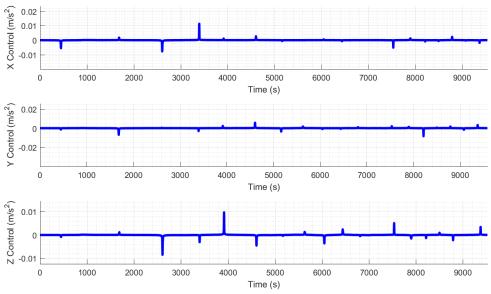

Figure 6.33 Maintenance - Control

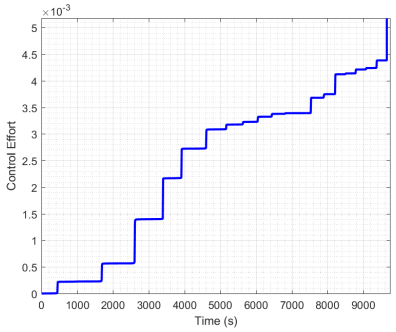

Figure 6.34 Maintenance - Control Effort

Relevant to this discussion is the nature of the control that acts to keep the spacecraft within a certain radius of the reference trajectory. The spacecraft appears to impulsively apply control to keep it within the acceptable error sphere, which exhibits the same bang-bang-like control seen in the spring-mass-damper example. In general, this gives credence to the fact that the formulation obeys the dynamical nature of these optimal control problems at short intervals, even if they are not optimal from a control sense in the global case.

There is one caveat to using this methodology. The velocity is allowed to increase in an unbounded fashion because there are no constraints on the velocity. For longer simulations, the constraints begin to be violated. It is believed that these errors originate from this free velocity motion. Figure 6.32 illustrates the erratic behavior in changes in velocity as time progresses. As these changes increase, it may be more difficult to successfully counter the position when the velocity is not monitored. Future work could include an analysis which would consider both a constraint on position and velocity error.

7. Conclusion and Future Work

Within this thesis, multiple tools for usage in constrained motion analysis have been presented. In Chapter 3, a dynamical formalism for the effects of nonuniform gravitational fields on rigid body spacecraft was generalized and presented for future use. The treatment of constrained motion within the geometric mechanics framework was defined using Udwadia-Kalaba formulation. This geometric mechanics Udwadia-Kalaba formalism (GMUK) was provided on six-dimensional Euclidean space $\mathbb{R}^6$ for fully and underconstrained systems of rigid bodies as well as on the double tangent bundle $T^2SE(3)$ for the fully constrained case in Chapter 4.

Chapter 5 explored treatment of perturbations and disturbances within the UK formulation. A Morse-Lyapunov based controller utilizing a backstepping technique was extended to ensure the almost global asymptotic stability of the system under disturbed initial conditions. This same controller was further manipulated to accommodate a set of disturbances. It was shown that the Morse-Lyapunov based backstepping tracking control technique introduced here was capable of treating external disturbances and perturbations in the system while the constraint acceleration for the nominal system was obtained using the UK formulation. In Chapter 6, a novel approach for incorporating inequality constraints within UK formulation based on implementation of slack and excess variables was presented and applied to two different systems. The optimality of this approach was assessed using analytical and numerical analyses.

7.1. Future Work

As future work, there are several areas of the included development that can be further explored. First, modeling of underconstrained systems on $T^2SE(3)$ requires simulation based on the formulation presented herein. Furthermore, more complex constraints should be explored and analyzed to better understand how robust the GMUK development is. In addition, the application presented here was focused on elliptical and circular orbits. Using this analysis for parabolic and hyperbolic orbits is expected to require little to no changes to

the formulation; however, no simulations have been run with these conditions. Within the usage of the Morse-Lyapunov based controller, more work can be done to tune the gains to get a more desirable response; however, proof of the almost global asymptotic stability remains despite the values of the gains detailed here. In addition, the implementation of more higher order terms as detailed in Chapter 3 can be applied to add additional accuracy to the dynamical model or perturbations acting on the system. The development of the inequality constraint conversion to equality constraints would benefit from more rigorous testing and analysis. The specification of the slack and excess dynamics should be of paramount importance, as accurately determining an approach for modeling these dynamics may further confirm the validity of this methodology.

Finally, a key area for development, both within constrained motion and geometric mechanics, is trajectory optimization within said framework. There are two primary areas that should be explored. First, at some point, both in direct and indirect trajectory optimization, it will be required to compute the Hessian of a matrix with respect to another matrix. The literature is somewhat unclear on how to approach this. Secondarily, analysis of constrained optimization on matrix manifolds has yet to be fully developed. Optimization algorithms do exist for matrix manifolds; however, traditional constrained optimization methods, such as reduced gradient based algorithms, have not yet been formed on matrix manifolds. Successful solutions to these issues will enable the development of optimization schemes for rigid body motion on $SE(3)$. Potential applications include trajectory optimization of rigid-body spacecraft during lunar or Martian landing.

REFERENCES

Abramowitz, M., & Stegun, I. A. (2014). *Handbook of mathematical functions with formulas, graphs, and mathematical tables*. Martino Publishing.

Absil, P. A., Mahony, R., & Sepulchre, R. (2008). *Optimization algorithms on matrix manifolds*. New Jersey: Princeton University Press.

Antunes, J., Debut, V., Borsoi, L., Delaune, X., & Piteau, P. (2017). A modal udwadia-kalaba formulation for vibro-impact modelling of continuous flexible systems with intermittent contacts. *Procedia Engineering*, *199*, 322–329.

Barker, M., Mazarico, E., Neumann, G., Zuber, M., Haruyama, J., & Smith, D. (2016). A new lunar digital elevation model from the lunar orbiter laser altimeter and selene terrain camera. *Icarus*, *273*, 346–355.

Baumgarte, J. (1972). Stabilization of constraints and integrals of motion in dynamical systems. *Computer Methods in Applied Mechanics and Engineering*, *1*, 1-16.

Bell, E. (2020, May). *Apollo 16 subsatellite.* NASA. Retrieved from `https://nssdc.gsfc.nasa.gov/nmc/spacecraft/display.action?id=1972-031D`

Betts, J. T. (1998). Survey of numerical methods for trajectory optimization. *Journal of Guidance, Control, and Dynamics*, *21*(2), 193–207.

Biggs, J., & Holderbaum, W. (2005). The geometry of optimal control solutions on some six dimensional lie groups. *Proceedings of the 44th IEEE Conference on Decision and Control*. doi: 10.1109/cdc.2005.1582359

Casado, M. L., & Martínez-Rubio, D. (2019). Cheap orthogonal constraints in neural networks: A simple parametrization of the orthogonal and unitary group. *CoRR*, *abs/1901.08428*. Retrieved from `http://arxiv.org/abs/1901.08428`

Cho, H., & Udwadia, F. E. (2010). Explicit solution to the full nonlinear problem for satellite formation-keeping. *Acta Astronautica*, *67*, 369-387.

Dodson, C. T. J., & Galanis, G. (2005). Bundles of acceleration on banach manifolds. *Nonlinear Analysis: Theory, Methods and; Applications*, *63*(5-7). doi: 10.1016/j.na.2004.12.022

Dodson, C. T. J., & Galanis, G. N. (2004). Second order tangent bundles of infinite dimensional manifolds. *Journal of Geometry and Physics*, *52*(2), 127–136. doi: 10.1016/j.geomphys.2004.02.005

Dong, H., Hu, Q., & Akella, M. R. (2018, May). Dual-quaternion-based spacecraft autonomous rendezvous and docking under six-degree-of-freedom motion constraints.

Journal of Guidance, Control, and Dynamics, *41*(5). doi: https://doi.org/10.2514/1.G003094

Elipe, A., & Lara, M. (2003). Frozen orbits about the Moon. *Journal of Guidance, Control, and Dynamics*, *26*(2), 238–243.

Fahroo, F., & Ross, I. (2000). Trajectory optimization by indirect spectral collocation methods. In *Astrodynamics specialist conference*. (p. 123-129).

Griva, S. G., & Nash, I. (2017). *Linear and nonlinear optimization*. Orient Blackswan Pvt Ltd.

Hedengren, J., Shishivan, R. A., Powell, K., & Edgar, R. (2014). Nonlinear modeling, estimation and predictive control in ap monitor. *Computers and Chemical Engineering*, *70*, 133-148.

Kelly, M. (2016). Transcription methods for trajectory optimization. *Cornell University*, *arXiv:1707.00284*.

Kelly, M. (2017). An introduction to trajectory optimization: How to do your own direct collocation. *SIAM Review*, *69*(4), 849-904.

Khalil, H. (2002). *Nonlinear systems* (3rd ed.). New Jersey: Upper Saddle River.

Knežević, Z., & Milani, A. (1998). Orbit maintenance of a lunar polar orbiter. *Planetary and Space Science*, *46*(11-12), 1605–1611, doi: 10.1016/S0032-0633(98)00021-X.

Konopliv, A. S., Park, R. S., Yuan, D.-N., Asmar, S. W., Watkins, M. M., Williams, J. G., ... et al. (2013). The JPL lunar gravity field to spherical harmonic degree 660 from the GRAIL Primary Mission. *Journal of Geophysical Research: Planets*, *118*(7), 1415–1434.

Kuhn, H., & Tucker, A. (1951). Nonlinear programming. In *Proceedings of 2nd berkeley symposium* (pp. 481–492). Berkeley: University of California Press.

Lam, T. (2006). A new approach to mission design based on the fundamental equations of motion. *Journal of Aerospace Engineering*, *19*(2), 59-67.

Lemoine, F. G., Goossens, S., Sabaka, T. J., Nicholas, J. B., Mazarico, E., Rowlands, D. D., ... et al. (2013). High-degree gravity models from GRAIL primary mission data. *Journal of Geophysical Research: Planets*, *118*(8), 1676–1698.

Lemoine, F. G., Goossens, S., Sabaka, T. J., Nicholas, J. B., Mazarico, E., Rowlands, D. D., ... et al. (2014). GRGM900C: A degree 900 lunar gravity model from GRAIL primary and extended mission data. *Geophysical Research Letters*, *41*(10), 3382-–3389.

Lewis, F. L., Syrmos, V. L., & Vrabie, D. L. (2012). *Optimal control*. Hoboken, NJ: Wiley.

Liu, X., Lu, P., & Pan, B. (2017). Survey of convex optimization for aerospace applications. *Astrodyn 1*, 23-40.

Low, G. M. (1969, Nov). *Apollo 11 mission report.* Retrieved from `https://www.nasa.gov/specials/apollo50th/pdf/A11_MissionReport.pdf`

Luenberger, D. (1969). *Optimization by vector space*. New York, NY: Wiley.

Memon, M. W., Nazari, M., Seo, D., & Prazenica, R. (2019, August 11-15). Constrained motion analysis and nonlinear optimal tracking control of two-craft Coulomb formation in elliptic chief orbits. *AAS/AIAA Astrodynamics Specialist Conference*. (AAS 19-706)

Michor, P. W. (2008). *Topics in differential geometry*. Providence, RI: American Mathematical Society.

Misra, G., Izadi, M., Sanyal, A., & Scheeres, D. (2016). Coupled orbit–attitude dynamics and relative state estimation of spacecraft near small Solar System bodies. *Advances in Space Research*, *57*(8), 1747–1761. doi: 10.1016/j.asr.2015.05.023

Müller, A., & Terze, Z. (2014a). On the choice of configuration space for numerical Lie group integration of constrained rigid body systems. *Journal of Computational and Applied Mathematics*, *262*, 3–13.

Müller, A., & Terze, Z. (2014b). The significance of the configuration space Lie group for the constraint satisfaction in numerical time integration of multibody systems. *Mechanism and Machine Theory*, *82*, 173-–202.

Nazari, M., Maadani, M., Butcher, E., & Yucelen, T. (2018, 01). Morse-lyapunov-based control of rigid body motion on tse(3) via backstepping. In *Scitech.* doi: 10.2514/6.2018-0602

Nielsen, M. C., Eidsvik, O. A., Blanke, M., & Schjølberg, I. (2020). Constrained multi-body dynamics for modular underwater robots: Theory and experiments. *Ocean Engineering*, *149*, 358-372.

Nocedal, J., & Wright, S. (2006). *Numerical optimization*. New York,NY: Springer.

Patel, H., Henderson, T. A., & Nazari, M. (2019, August 11-15). Application of Udwadia-Kalaba formulation to three-body problem. *AAS/AIAA Astrodynamics Specialist Conference*. (AAS 19-706)

Pontryagin, L., & Neustadt, L. W. (1986). *The mathematical theory of optimal processes*. Gordon and Breach Science Publishers.

Pothen, A. A., & Ulrich, S. (2019). Close-range rendezvous with a moving target spacecraft using udwadia- kalaba equation. In *2019 american control conference (acc)* (p. 3267-3272).

Sastry, S. (1999). *Nonlinear systems: Analysis, stability, and control*. New York, NY: Springer.

Schaub, H., & Junkins, J. L. (2018). *Analytical mechanics of space systems* (4th ed.). American Institute of Aeronautics and Astronautics. doi: 10.2514/4.105210

Scheeres, D. J. (2012). *Orbital motion in strongly perturbed environments: Applications to asteroid, comet and planetary satellite orbiters*. Berlin, Heidelberg: Springer.

Scheeres, D. J., Ostro, S. J., Hudson, R. S., Dejong, E. M., & Suzuki, S. (1998). Dynamics of orbits close to asteroid 4179 Toutatis. *Icarus*, *132*(1), 53–79.

Shah, N., Calhoun, P., Garrick, J., Hsu, O., & Simpson, J. (2010). Launch and commissioning of the lunar reconnaissance orbiter (lro. *American Astronautical Society Guidance and Control Conference*.

Stackhouse, W., Nazari, M., Henderson, T., & Prazenica, R. (2020). Adaptive control design using the Udwadia-Kalaba formulation for hovering over an asteroid with unknown gravitational parameters. *AIAA Scitech 2020 Forum*.

Stackhouse, W., Nazari, M., Henderson, T., & Yucelen, T. (2019, August 11-15). Spacecraft asteroid hovering using Udwadia-Kalaba formualation with time-varying coefficients. *AAS/AIAA Astrodynamics Specialist Conference*. (AAS 19-706)

Sun, H., Zhao, H., Zhen, S., Huang, K., Zhao, F., Chen, X., & Chen, Y.-H. (2015, Aug). Application of the udwadia–kalaba approach to tracking control of mobile robots. *Nonlinear Dynamics*, *83*. doi: https://doi.org/10.1007/s11071-015-2335-3

Sun, H., Zhao, H., Zhen, S., Huang, K., Zhao, F., Chen, X., & Ye-Hwa, C. (2016, 01). Application of the Udwadia–Kalaba approach to tracking control of mobile robots. *Nonlinear Dynamics*, *83*(1-2), 389-400.

Suri, A. (2013). Geometry of the double tangent bundles of Banach manifolds. *Journal of Geometry and Physics*, *74*, 91–100. doi: 10.1016/j.geomphys.2013.07.009

Suri, A. (2016). Higher order tangent bundles. *Mediterranean Journal of Mathematics*, *14*(1). doi: 10.1007/s00009-016-0812-7

Udwadia, F. E., & Kalaba, R. E. (1992). A new perspective on constrained motion. *Proceedings of the Royal Society of London. Series A: Mathematical and Physical Sciences*, *439*, 407-410.

Udwadia, F. E., & Kalaba, R. E. (2008). *Analytical dynamics: A new approach*. New York: Cambridge University Press.

Udwadia, F. E., & Schutte, A. D. (2011). A unified approach to rigid body rotational dynamics and control. *Proceedings of the Royal Society A: Mathematical, Physical and Engineering Sciences*, *468*(2138), 395–414.

Vallado, D. A. (2013). *Fundamentals of astrodynamics and applications* (4th ed.). Microcosm Press.

Valverde, A., & Tsiotras, P. (2018, 11). Dual quaternion framework for modeling of spacecraft-mounted multibody robotic systems. *Frontiers in Robotics and AI*, *5*.

Xu, Y., & Liu, R. (2017). Dynamic modeling of scara robot based on udwadia–kalaba theory. *Advances in Mechanical Engineering*, *9*(10), 168781401772845. doi: 10.1177/1687814017728450

Yang, X., Zhang, X., Chen, Z., Xu, S., & Liu, P. X. (2019, Apr). Udwadia-kalaba approach for three link manipulator dynamics with motion constraints. *IEEEAccess*.

Yin, H., Chen, Y., & Yu, D. (2019). Vehicle motion control under equality and inequality constraints: a diffeomorphism approach. *Nonlinear Dynamics*, *95*, 175-194.

Zupp, G. A. (January 2013). An analysis and a historical review of the apollo program lunar module touchdown dynamics. *https://www.lpi.usra.edu/lunar/documents/SP-2013-605.pdf*.